

Precision measurement of the top quark pair production cross section at $\sqrt{s} = 13$ TeV with the CMS detector

Dissertation

zur Erlangung des Doktorgrades
an der Fakultät für Mathematik, Informatik und Naturwissenschaften
Fachbereich Physik
der Universität Hamburg

vorgelegt von

TILL ARNDT
aus Frankfurt am Main

Hamburg
2018

Gutachter der Dissertation:	PD. Dr. Andreas Meyer Prof. Dr. Johannes Haller
Zusammensetzung der Prüfungskommission:	Prof. Dr. Caren Hagner Prof. Dr. Gudrid Moortgat-Pick Prof. Dr. Johannes Haller PD. Dr. Andreas Meyer Dr. Roberval Walsh
Vorsitzender der Prüfungskommission:	Prof. Dr. Caren Hagner
Datum der Disputation:	5.07.2018
Vorsitzender Fach-Promotionsausschusses PHYSIK:	Prof. Dr. Wolfgang Hansen
Leiter des Fachbereichs PHYSIK:	Prof. Dr. Michael Potthoff
Dekan der Fakultät MIN:	Prof. Dr. Heinrich Graener

Eidesstattliche Versicherung

Hiermit versichere ich an Eides statt, die vorliegende Dissertationsschrift selbst verfasst und keine anderen als die angegebenen Hilfsmittel und Quellen benutzt zu haben.

Die eingereichte schriftliche Fassung entspricht der auf dem elektronischen Speichermedium.

Die Dissertation wurde in der vorgelegten oder einer ähnlichen Form nicht schon einmal in einem früheren Promotionsverfahren angenommen oder als ungenügend beurteilt.

Hamburg, den 15.05.2018

Till Arndt

Abstract

This work presents several measurements of the inclusive top pair production cross section at a center of mass energy of $\sqrt{s} = 13$ TeV with the CMS detector. The cross section is measured using several data sets collected by the CMS detector in 2015 and 2016. The main and most precise result is obtained using full 2016 data set with an integrated luminosity of $\mathcal{L}_{\text{int}} = 35.9 \text{ fb}^{-1}$.

The top quark pair production cross section is measured with a likelihood fit. The events are required to contain two charged leptons. The top quark pair production cross section is first measured in the visible phase space, as defined by the detector acceptance. It is then extrapolated to the full phase space.

The efficiency of the lepton triggers is measured independently. The uncertainty on the trigger efficiency is determined comparing multiple measurement techniques and then propagated to the measurement of the top quark pair production cross section.

The top quark pole mass is extracted from the cross section measurement, using the next-to-next-to-leading order (NNLO) prediction for the top quark pair production cross section and its measured value.

Zusammenfassung

Diese Arbeit beschreibt mehrere Messungen des Wirkungsquerschnittes für Top Quark Paarproduktion mit dem CMS Detektor bei einer Schwerpunktsenergie von $\sqrt{s} = 13$ TeV. Der Wirkungsquerschnitt wird für verschiedene Datensätze gemessen, die in den Jahren 2015 und 2016 von dem CMS Detektor gesammelt wurden. Das Hauptergebnis wird mit dem vollständigen Datensatz aus 2016 mit einer integrierten Luminosität von $\mathcal{L}_{\text{int}} = 35.9 \text{ fb}^{-1}$ gemessen.

Der Wirkungsquerschnitt für Top Quark Paarproduktion wird mit einer Maximum-Likelihood-Anpassung für Ereignisse mit zwei geladenen Leptonen gemessen. Er wird zuerst im sichtbaren Phasenraum gemessen, der durch die Akzeptanz des Detektors definiert wird. Danach wird der Wirkungsquerschnitt für Top Quark Paarproduktion in den kompletten Phasenraum extrapoliert.

Die Effizienz der Leptontrigger wird separat gemessen. Ihre Unsicherheit wird durch den Vergleich mehrerer Messmethoden bestimmt und dann in der Messung des Wirkungsquerschnitts für Top Quark Paarproduktion verwendet.

Die Polmasse des Top Quarks wird durch den Vergleich des gemessenen Wirkungsquerschnitts für Top Quark Paarproduktion mit einer Vorhersage in nächst-zu-nächst-zuführender-Ordnung (NNLO) bestimmt.

Table of contents

1	Introduction	1
2	Theory	3
2.1	The Standard Model	3
2.1.1	The electroweak interaction	5
2.1.2	The strong interaction	7
2.2	The top quark	8
2.2.1	Top quark pair production and decay	9
2.2.2	The top quark mass	12
2.3	Background processes	13
2.4	Simulation	15
3	The LHC and the CMS experiment	19
3.1	The Large Hadron Collider	19
3.2	The CMS detector	21
3.2.1	The tracking system	22
3.2.2	The electromagnetic calorimeter	23
3.2.3	The hadronic calorimeter	25
3.2.4	The muon system	26
3.2.5	Triggering	28
4	Reconstruction	31
4.1	Tracking and vertex reconstruction	32
4.2	Electron reconstruction	34
4.3	Muon reconstruction	36
4.4	Reconstruction of jets	37
4.5	Identification of b jets	39

5 Trigger efficiency measurement	41
5.1 Trigger selection	41
5.2 Methods using independent triggers	42
5.3 Method using tag-and-probe	49
5.4 Comparison of trigger efficiency measurements	50
5.5 Determination of the trigger scale factor	54
6 Cross section measurement	59
6.1 Analysis strategy	59
6.2 Event selection	61
6.3 Comparison of simulation and data	62
6.4 Choice of event categories and template distributions	68
6.5 Definition of the likelihood	70
6.6 Extrapolation from the visible to the full phase space	76
7 Systematic uncertainties	79
7.1 Experimental uncertainties	80
7.1.1 Uncertainties related to leptons	80
7.1.2 Uncertainties related to jets	81
7.1.3 Further experimental uncertainties	82
7.2 Theoretical uncertainties	85
8 Results	91
8.1 Results with the 2015 data sets	91
8.1.1 First measurement of the top pair production cross section at 13 TeV	92
8.1.2 Measurement of the top quark pair production cross section with the 2015 data set	94
8.2 Measurement of the top quark pair production cross section with the 2016 data set	96
8.2.1 Post-fit template distribution	96
8.2.2 Results for systematic uncertainties	100
8.3 Comparison to theory predictions and previous results	103
8.4 Addition of the semileptonic channel	104
8.5 Extraction of the top quark pole mass	105
9 Conclusion and outlook	107
References	111

Appendix A Detailed breakdown of systematic uncertainties	119
--	------------

Appendix B List of publications	123
--	------------

Chapter 1

Introduction

Particle physics aims to explore the fundamental structure of the world, the elementary particles and forces. The Standard Model (SM) is the theory describing particle physics and has successfully predicted experimental results at highest precision. It tries to explain the early universe as well as the smallest building blocks of matter. It is able to describe elementary interactions over energy scales of many orders of magnitude.

One of the important particles in the SM is the top quark. The top quark has a large coupling to the Higgs boson, making it the heaviest known particle. This high mass leads to a very short lifetime, allowing the study of bare quark properties. Properties of the top quark, such as the mass, are also important for the determination of Standard Model parameters. Top quarks also have a high production rate, which makes their production one of the important background processes for measurements of rare SM processes, Higgs boson processes and searches for physics beyond the SM. The top quark is also linked to various models predicting new phenomena beyond the SM.

The top quark pair production cross section is predicted at high precision by SM calculations. Measuring the top quark production cross section with high precision enables a stringent test of these calculations and their underlying assumptions. Confronting the measured top quark pair production cross section with the predicted value allows for the extraction of further Standard Model parameters like the strong coupling, α_S , or the mass of the top quark.

With the start of the Large Hadron Collider (LHC) at CERN a new energy frontier opened up in 2009. Until 2012 the LHC provided proton-proton collisions at a center of mass energy of up to $\sqrt{s} = 8 \text{ TeV}$. After a two-year break the LHC resumed operations with even higher collision energies, $\sqrt{s} = 13 \text{ TeV}$, in 2015 through 2018. The data collected at the new energy frontier offers new opportunities to observe new physics processes and confirm previous observations.

The Compact Muon Solenoid (CMS) detector is one of the experiments at the LHC. It is a multi-purpose detector. One of the greatest achievements of the CMS collaboration was the discovery of the Higgs boson, together with the ATLAS collaboration, in 2012 [1, 2].

In the context of this work, three measurements of the top quark pair production cross section were performed. The first measurement uses data taken in 2015 by the CMS detector with an integrated luminosity of $\mathcal{L}_{\text{int}} = 42 \text{ pb}^{-1}$. The first measurement of the top quark pair production cross section at $\sqrt{s} = 13 \text{ TeV}$ is designed to test for a possible strong deviation from the SM. The purpose of a second measurement, which uses data taken in 2015 with an integrated luminosity of $\mathcal{L}_{\text{int}} = 2.2 \text{ fb}^{-1}$ is to corroborate the result of the first measurement with more data. The third measurement is the main focus of this work. It uses data taken in 2016 with an integrated luminosity of $\mathcal{L}_{\text{int}} = 35.9 \text{ fb}^{-1}$ to measure the top quark pair production cross section with the highest possible precision.

Several steps are taken to ensure a high precision. In order to select a sample with a high number of top quark pair ($t\bar{t}$) events, events with two leptons in the final state are chosen for the measurement of the cross section. Moreover, systematic uncertainties are addressed in detail. Special emphasis is given to the uncertainty in the determination of the efficiency of the triggers. These triggers select the basic dataset for the cross section measurement and fundamentally determine the reach of this analysis. Therefore, the trigger efficiency and its uncertainty are precisely determined in a separate measurement. The top quark cross section is then measured with a likelihood fit to kinematic observables, taking into account systematic uncertainties and their correlations.

Relevant theoretical aspects are described in Chapter 2. This includes a brief summary of top quark physics as well as a description of the simulation. The experimental setup is described in Chapter 3, including the LHC and the CMS detector. The reconstruction of data and simulation is described in Chapter 4. The measurement of the trigger efficiency is described in Chapter 5. The uncertainty on the trigger efficiency is assessed by comparing multiple methods. The measurement of the top quark pair production cross section is described in Chapter 6. The different parts of the measurement such as the event selection and the fit are described in detail. The agreement of data and simulation is verified for a range of observables. Chapter 7 provides a detailed description of the systematic uncertainties used in the measurement. The results are given in Chapter 8. This chapter also includes the extraction of the top quark pole mass using the measured $t\bar{t}$ cross section. A study is presented addressing the impact of including events with one muon in the final state in the $t\bar{t}$ cross section measurement. Chapter 9 summarizes the results and shows possibilities for future improvement.

Chapter 2

Theory

The theoretical framework of particle physics, the Standard Model (SM), has been developed since the 1960s [3, 4]. Up to now it has been successful in explaining most of the observations made in particle physics experiments. Especially important for this analysis are predictions concerning top quark production in proton-proton collisions, which can be calculated at a high level of accuracy.

In this chapter an overview of the Standard Model is given in Section 2.1. The top quark and its properties are explained in Section 2.2. Background processes that are relevant for this measurement of the $t\bar{t}$ production cross section are described in Section 2.3. The simulation used for the $t\bar{t}$ production cross section measurement is described in Section 2.4.

2.1 The Standard Model

The Standard model is a quantum field theory describing subatomic particles and their interactions. In the SM there are two types of elementary particles: The fermions with a half integer spin as the fundamental building blocks of matter and the bosons with an integer spin as the mediators of the interactions. The SM describes the existence of multiple generations of fermions where particles have different masses in each generation, but the same properties otherwise. After the discovery of the first generation of SM particles (mostly in the first half of the twentieth century), a second and third generation of fermions was discovered by the Stanford Linear Accelerator Center [5, 6]. The SM also describes the existence of W and Z bosons, which were then discovered in the 1980s by the UA1 and UA2 experiments at CERN [7–10]. These discoveries confirmed the SM as the model of particle physics. The currently known particles of the standard model are shown in Figure 2.1 with their mass, electric charge and spin.

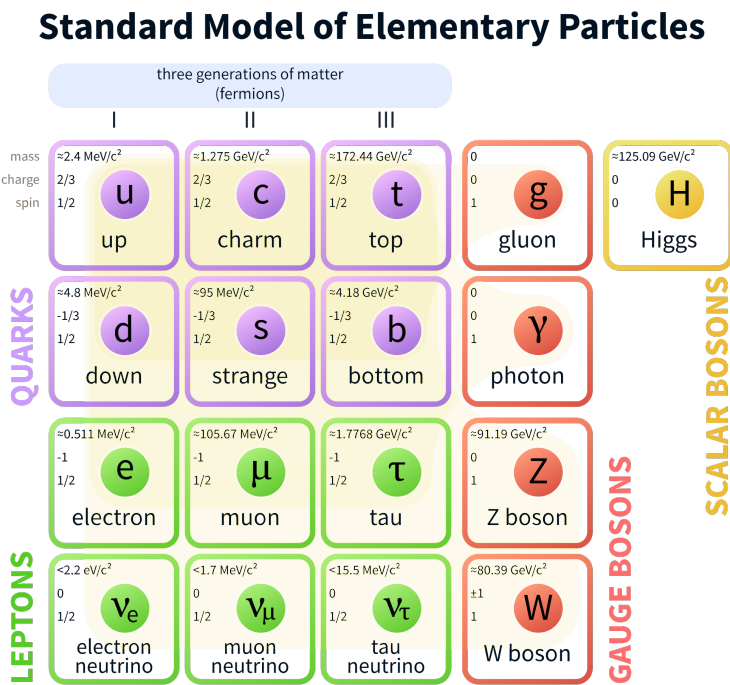


Figure 2.1: The particles of the Standard Model with their respective mass, electric charge and spin [11]. The first three columns show the three generations of fermions. The fourth column shows the vector bosons (spin of one). In the right-most column the scalar (spin of zero) Higgs boson is displayed.

The SM describes three interactions or forces: The strong interaction, the weak interaction and the electromagnetic interaction. The latter two can be unified as the electroweak interaction. The strong interaction is mediated by 8 gluons, which carry the charge of the hard interaction, color. The electroweak interaction is mediated by the photon, the Z boson and the two W bosons. The charge of the electroweak interaction is the weak hypercharge, a combination of the electromagnetic charge and the weak isospin. Gluons and photons are massless, while the W and Z bosons have a mass, which makes the electroweak interaction 'weak'. These masses are in principle not in line with the requirement of electroweak symmetry. The Higgs mechanism [12–14] introduces spontaneous breaking of the electroweak symmetry, which allows for massive bosons. This mechanism also predicted the existence of another boson with zero spin, the Higgs boson, which was discovered in 2012 at the LHC [1, 2].

The fermions are further divided into two categories: The leptons which are only affected by the electroweak interaction and the quarks which interact with both the electroweak and the strong force. There are three generations of fermions, in each generation there are particles with the same properties and a charge difference of one. Only the mass is different, increasing with each generation.

2.1.1 The electroweak interaction

The unification of the electromagnetic interaction and the weak interaction occurs at the scale of the mass of the bosons mediating the weak interaction (W and Z bosons). This can be seen in the measurement of deep inelastic electron-proton interactions, which were measured at the highest energies at the HERA collider by the H1 and ZEUS collaborations [15] (see Figure 2.2). Neutral currents are mediated by the photon and Z boson and charged currents are mediated by the W^+ and W^- bosons carrying an electrical charge. The scale where the cross sections of both currents start to agree is the unification scale of the electromagnetic and weak interaction. Below that scale the weak interaction is suppressed due to the mass of the corresponding bosons.

The transition or decay of heavier quarks into lighter quarks is explained by the mixing of flavor eigenstates and weak eigenstates. The transition is mediated by a W boson and the probability is determined by the Cabibbo-Kobayashi-Maskawa (CKM) matrix. The probability of one quark transitioning to another quark is proportional to the square of the CKM matrix element V_{ab} . The CKM matrix is required to be unitary in the standard model. With that requirement its values are measured to be [16]:

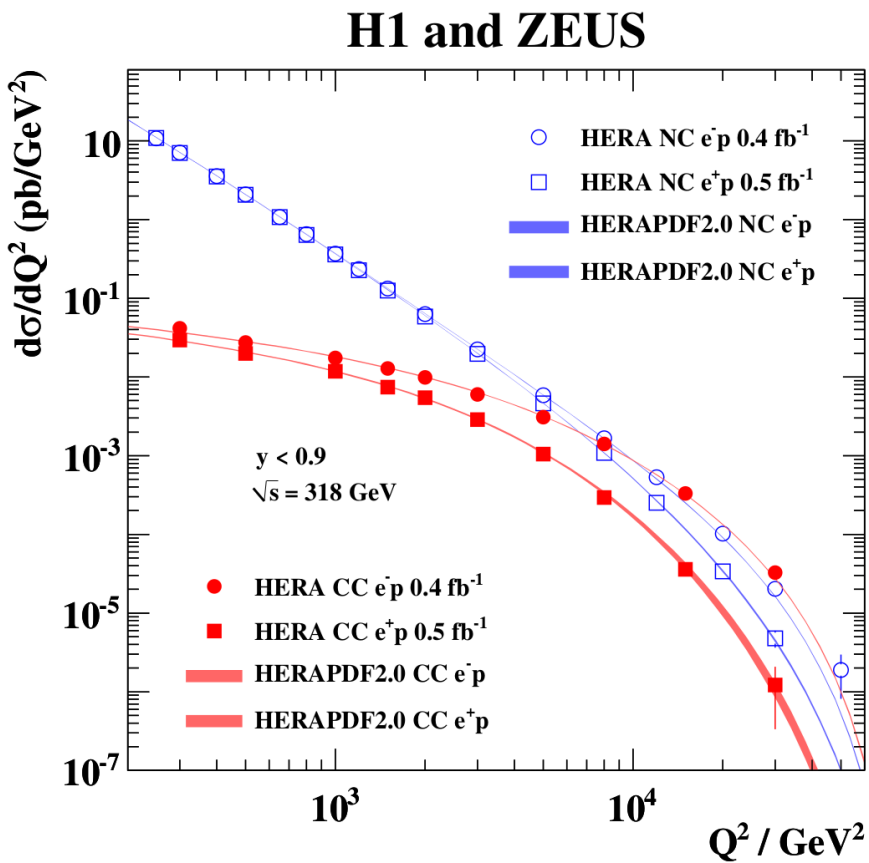


Figure 2.2: Measurement of the neutral and charged current interaction cross section in e^-p and e^+p collisions by the H1 and ZEUS collaboration [15]. The cross sections depend on the total momentum transfer and the measurement is compared to predictions from HERAPDF2.0.

$$V_{\text{CKM}} = \begin{pmatrix} V_{ud} & V_{us} & V_{ub} \\ V_{cd} & V_{cs} & V_{cb} \\ V_{td} & V_{ts} & V_{tb} \end{pmatrix} = \begin{pmatrix} 0.947 & 0.225 & 0.004 \\ 0.225 & 0.973 & 0.041 \\ 0.009 & 0.041 & 0.999 \end{pmatrix}. \quad (2.1)$$

The electroweak interaction is described by a $SU(2)_L \otimes U(1)_Y$ gauge symmetry. To preserve that symmetry, all bosons would need to be massless, which contradicts experimental measurements. Particle masses for bosons as well as fermions can be introduced by an additional field, the Higgs field, with a potential that can be written as:

$$V(\Phi) = \mu^2 \Phi^\dagger \Phi + \lambda (\Phi^\dagger \Phi)^2 \quad (2.2)$$

Here, λ is restricted to $\lambda > 0$ and μ to $\mu^2 < 0$ in order to have non-zero masses. The minima of the potential lead to a non-zero vacuum expectation value of $v = -\mu^2/\lambda = 246$ GeV [16]. The vacuum expectation value is connected to the masses of the bosons and fermions, but otherwise these masses are free parameters that have to be measured experimentally.

2.1.2 The strong interaction

The strong interaction is described by Quantum Chromo Dynamics (QCD), which comprises a $SU(3)_C$ gauge group. The charge of the QCD is called color and is mediated by 8 gluons, which are massless bosons. The interaction length of the strong force is short, due to a phenomenon called confinement. It requires all particles carrying a color charge to form color neutral hadrons, a process called hadronization.

Confinement is caused by the dependence of the coupling of the color charge (strong coupling) α_S on the energy scale of an interaction, shown in Figure 2.3.

The strong coupling increases with decreasing momentum transfer. Consequently, the coupling between two quarks increases with larger distances. This makes it energetically more beneficial to create a new quark anti-quark pair. This means that no bare color charge can exist for an extended period of time; the color is confined. The quarks, together with gluons, eventually form bound states, which are required to be colorless and are called hadrons. For the three colors (red, green and blue) a color neutral hadron can contain three valence quarks with a different color each and be called a baryon. Hadrons can also be formed from two quarks which have to form a pair of color and anti color (quark and anti quark). These hadrons are called mesons. Beside the proton all hadrons are unstable and decay eventually. A single high energetic quark will produce multiple hadrons which are collimated due to the momentum of the initial quark. In a detector, these collimated hadrons are measured as a so-called jet.

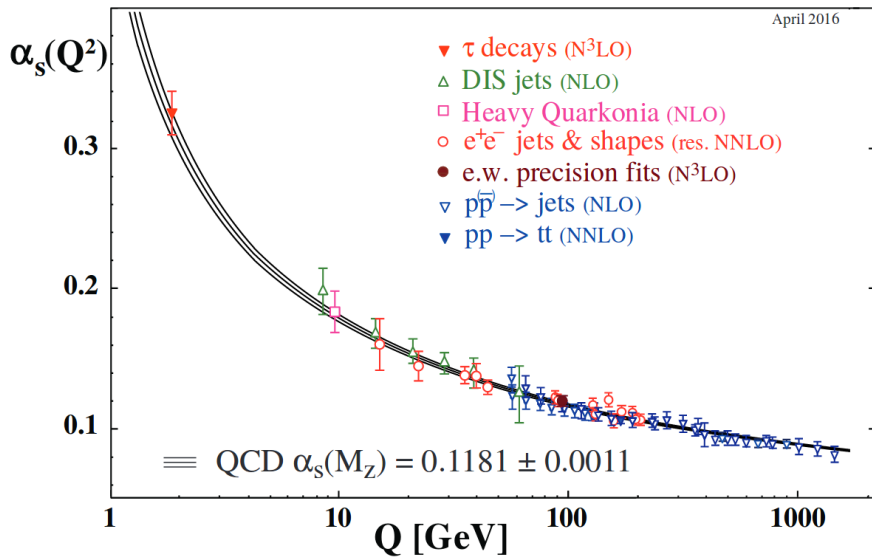


Figure 2.3: Dependence of α_s on the scale Q^2 of an interaction [16].

For high energies or short interaction scales the coupling strength decreases. This effect is called asymptotic freedom. It allows the quarks in a bound state, for example inside the proton, to be treated as free. At high scales the interaction can be calculated perturbatively, while processes at low scales such as hadronization are usually calculated based on phenomenological models.

2.2 The top quark

The top quark is the heaviest particle in the Standard Model and the heaviest elementary particle known to date. It was discovered in 1995 by the D0 and CDF collaborations at the Tevatron [17, 18]. Due to its high mass, it decays before it hadronizes, which allows measuring properties of the bare quark through the decay products. Multiple theories that extend the Standard Model predict particles that decay into top quarks. An example would be a massive Z' boson in extended gauge theories [19, 20] decaying into a $t\bar{t}$ pair. A supersymmetric top partner, a stop or a top squark, could also decay into a top quark and a neutralino, leading to a process very similar to $t\bar{t}$ production [21, 22]. Anomalous top quark couplings could also affect the production of top quarks as well as their decay [23–25].

2.2.1 Top quark pair production and decay

The calculation of top quark pair production cross section at the LHC can be factorized into a high energy ('hard') scattering process and the distribution of the momenta of the initial partons. At the LHC the probability to find a quark or gluon of a certain energy in the initial state is given by Parton Density Functions (PDFs), which can be measured independently from a specific physics process. The cross section can then be calculated perturbatively according to [26]:

$$\sigma = \sum_{jk}^{\text{partons}} \int_0^1 dx_k dx_j \cdot f_j(x_j, \mu_F) \cdot f_k(x_k, \mu_F) \cdot \hat{\sigma}(x_j, x_k, s, \mu_F, \alpha_S(\mu_R)) \quad (2.3)$$

The PDFs $f_i(x_i, \mu_F)$ give the probability to find a parton i with the momentum fraction x_i in the initial state when the initial state hadron is probed at the scale μ_F . The factorization scale μ_F separates the hard process from the PDF, which absorbs infrared or collinear divergences in the initial state. The scattering amplitude or hard cross section $\hat{\sigma}$ depends on the momentum fraction of the partons, the squared center of mass energy s and the strong coupling strength α_S calculated at defined scale μ_R . Introducing the renormalization scale μ_R as a cut-off avoids ultraviolet divergences in virtual corrections of the production cross section.

For proton-proton collisions at a center of mass energy of $\sqrt{s} = 13$ TeV, top quark pairs are mainly produced by gluon-gluon fusion. Only about 10% of $t\bar{t}$ pairs are produced through quark anti-quark annihilation [16]. The production of $t\bar{t}$ pairs via gluon-gluon fusion can occur in the s -, t - or u -channel. Feynman graphs for these production processes are shown in Figure 2.4.

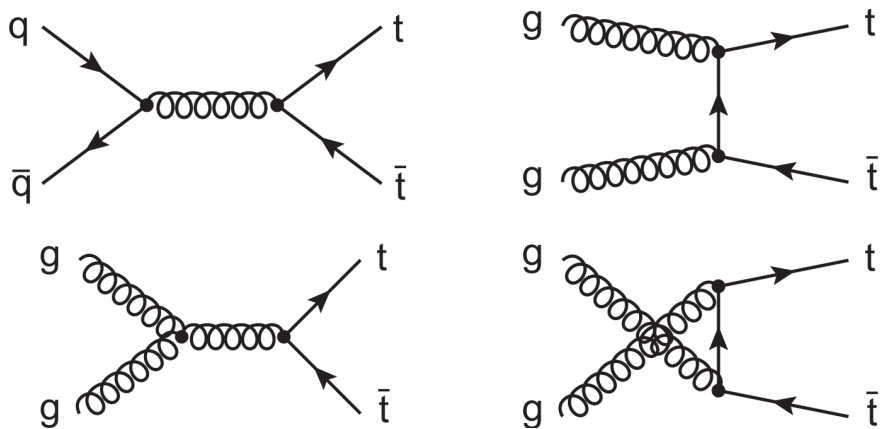


Figure 2.4: Feynman graphs for $t\bar{t}$ production from gluon-gluon fusion and quark anti quark annihilation (upper left) [26]. The production from gluon-gluon fusion is shown in the s - (lower left), t - (upper right) and u -channel (lower right).

Proton-proton collisions can also result in the production of single top quarks via the electroweak interaction. Single top quarks can be produced in the t- and s-channel or with an associated W boson. The respective Feynman diagrams are shown in Figure 2.5.

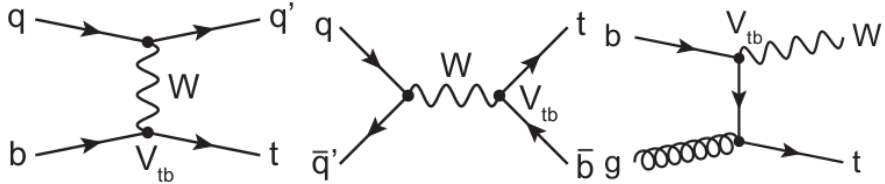


Figure 2.5: Feynman graphs for single top quark production in the t- (left), s-channel (middle) and with an associated W boson (right) [26].

Due to its high mass, the top quark has a very short lifetime. It decays before it would hadronize. Top quarks almost exclusively decay into a W boson and a b quark, due to the high value of the CKM matrix element $V_{tb} = 0.999$ (see Equation 2.1). A $t\bar{t}$ pair consequently decays into two W bosons and two b quarks. At next-to-leading order (NLO) of QCD the $gg \rightarrow WbWb$ process enters into calculations of single top production with an associated W boson, leading to interference with $t\bar{t}$ production [27]. However, the two processes can still be treated separately [28].

The total production cross section at a center of mass energy of $\sqrt{s} = 13$ TeV has been calculated at NNLO+NNLL as [29]:

$$\sigma_{t\bar{t}} = 832 \pm^{20}_{29} (\text{scale}) \pm 35(\text{PDF} + \alpha_s) \text{ pb.} \quad (2.4)$$

This very precise calculation can be tested by an equally precise measurement. Besides probing higher order QCD calculations, the comparison of the measured and predicted cross section can also be used to constrain anomalous phenomena. It can also be used to determine other SM parameters like the strong coupling strength α_s .

The cross sections for several processes in proton-proton collisions are shown in Figure 2.6. The $t\bar{t}$ production cross section increases significantly with the center of mass energy, especially compared to other processes. Nevertheless, the cross section for the production of b quarks and W or Z bosons is significantly higher at a center of mass energy of $\sqrt{s} = 13$ TeV. The ability to distinguish $t\bar{t}$ events from these other processes depends on the decay of the top quarks.

After the decay of the top quark into a W boson and a b quark, the W boson decays either into a lepton and the associated neutrino or into two quarks. Decays of $t\bar{t}$ events are separated into decay channels according to the decay of the W bosons.

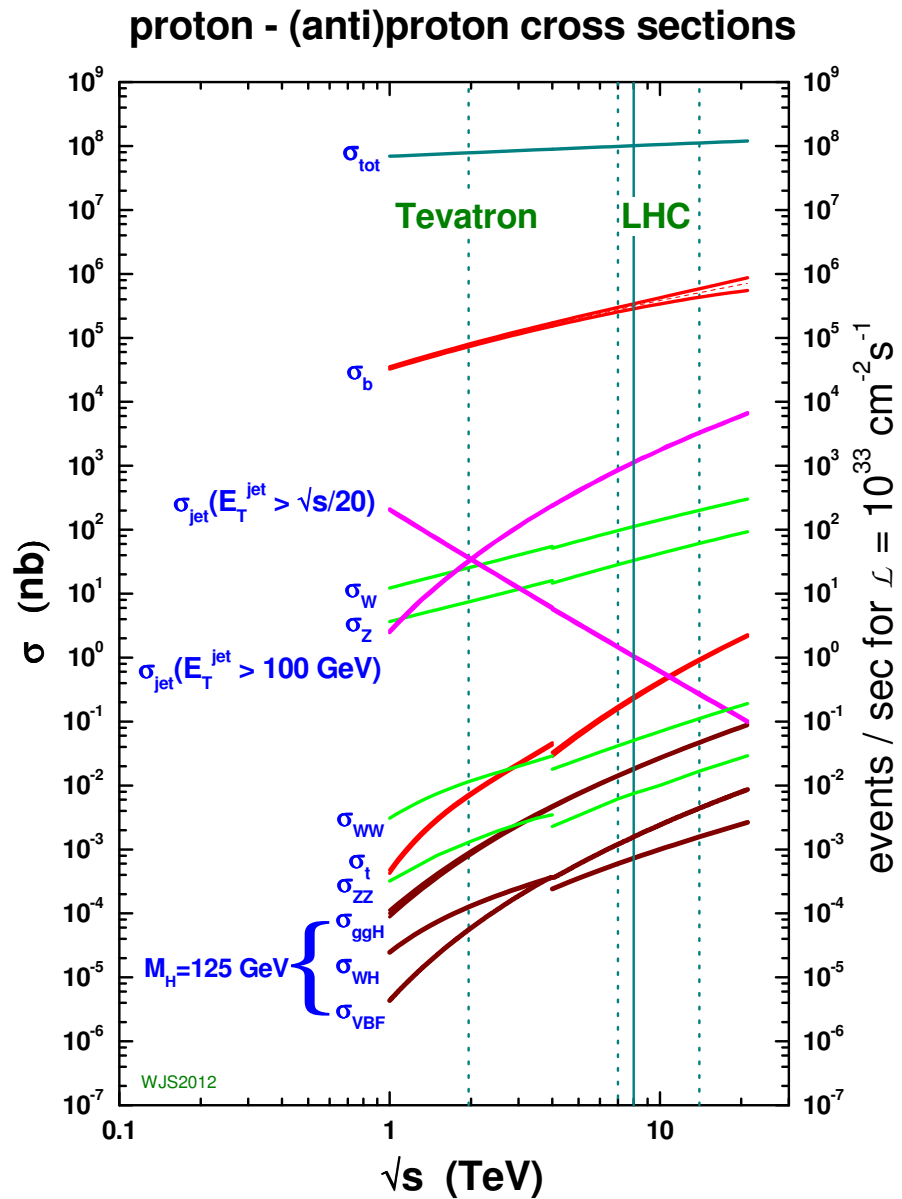


Figure 2.6: Cross sections for several processes at the Tevatron and the LHC depending on the center of mass energy \sqrt{s} [16].

In the all-hadronic decay channel, both W bosons decay into quarks: $t\bar{t} \rightarrow q\bar{q}b q\bar{q}\bar{b}$. This channel has the highest branching ratio of $\sim 45\%$, but it suffers from a lot of background contamination, since the cross section to produce multiple jets in proton-proton collisions is large compared to the $t\bar{t}$ cross section. This makes the all-hadronic channel unsuitable for a high precision measurement of the $t\bar{t}$ cross section.

In the semileptonic decay channel one W boson decays into quarks, the other into leptons: $t\bar{t} \rightarrow l^+ \nu_l b q\bar{q}\bar{b}$. This channel has a similar branching ratio to that of the all-hadronic channel at 45%, including events with τ leptons. The lepton in the final state makes the events easier to distinguish from background events. However, the cross section for W+jets production is still significantly higher, leading to a sizable background contamination.

In the dilepton decay channel both W bosons decay into leptons: $t\bar{t} \rightarrow l^+ \nu_l b l^- \bar{\nu}_l \bar{b}$. This channel has a comparatively low branching ratio of $\sim 10\%$, including τ leptons. The decays of τ leptons into quarks again effectively reduce the branching ratio. The dilepton decay channel has a clear signature thanks to the two leptons in the final state. The largest source of background events is Drell-Yan (Z+jets) process, which has a higher production cross section than the $t\bar{t}$ process, but can be distinguished by the Z mass peak in the dilepton mass spectrum. Especially the $e^\pm \mu^\mp$ decay channel combines a clear signature with a low background: Muons leave a clear signature in the detector and the main background from Drell-Yan events is reduced by requiring opposite flavored leptons in the final state.

The dilepton decay channel is suitable to achieve the highest possible precision for the measurement of the $t\bar{t}$ production cross section.

2.2.2 The top quark mass

The top quark mass is defined by its Yukawa coupling to the Higgs field. Conversely, since the mass is large, the Yukawa coupling is predicted to be large compared to the coupling of lighter particles. In both measurements and theory calculations, the top quark mass can be determined in multiple ways.

In a direct measurement of the top quark mass the decay products are identified and the invariant mass distribution of the decay products is measured. The relation of the observed to the actual top quark mass is usually provided by Monte Carlo (MC) generators. This method allows measuring the top quark mass with a high experimental precision [30, 31]. Since the simulation of $t\bar{t}$ decays includes phenomenological models the mass measured in such measurements does not exactly correspond to the mass definition used in theoretically well-defined calculations.

Perturbative calculations often use the pole mass definition, m_t^{pole} . It is well defined in every order of perturbation theory [32], but it suffers from non-perturbative ambiguities [33,

34]. It has been shown that this so-called renormalon ambiguity is of the size of 70 MeV [35]. It can be measured indirectly by measuring other top quark parameters and comparing them to theory predictions depending on m_t^{pole} . The predicted top quark pair production cross section depends on the assumed pole mass and can be used to extract the pole mass [36, 37]. The precision of these measurements is not only limited by the uncertainties on the measurement, but also by the theoretical uncertainties on m_t^{pole} . The top quark mass implemented in MC generators is assumed to be close to the pole mass [38], but a uncertainty of up to 1 GeV remains.

The scale-dependent top quark mass in the $\overline{\text{MS}}$ scheme does not contain non-perturbative ambiguities. It has also been shown to converge faster than the pole mass [33], leading to generally lower theoretical uncertainties. The relation to the pole mass is known to a high precision [39]. Similar to the pole mass it can be extracted from measurements of top quark parameters like the $t\bar{t}$ cross section [40].

The top quark mass is an important parameter in electroweak fits that are used to probe the SM prediction on the relation of several electroweak parameters [41]. The SM can be extrapolated to the Planck scale. In this extrapolation the vacuum state of the Higgs field has implications on the stability of the universe [42]. The stability of the vacuum state strongly depends on the Higgs mass, the top quark mass and α_S . In Figure 2.7 the stability is shown depending on the Higgs and the top quark mass. The current values for these masses hint at a metastable vacuum. Slightly different parameters could however lead to either a stable vacuum or contradictions to the observed lifetime of the universe.

2.3 Background processes

In an experiment, top quarks are not measured directly, but they are identified by their decay products. In the dilepton channel, which is used in this analysis, the $t\bar{t}$ decay produces the following final state: $t\bar{t} \rightarrow l^+ \nu_l b l^- \bar{\nu}_l \bar{b}$. The two neutrinos cannot be detected, so the signature in the detector consists of two leptons (electrons or muons) and two b quarks, which result in jets. For this analysis events are mainly selected according to the leptons. Multiple different SM processes can lead to a similar or even the same signature. The impact of these background events is an important part of $t\bar{t}$ cross section measurements and the underlying physics processes are shortly described below.

The largest source of background events in the dilepton channel is the Drell-Yan [43] process. A Z boson is produced through electroweak interaction and decays into two leptons. Two b quarks can originate from initial state radiation, which leads to the same final state measured for $t\bar{t}$ events. In the $e^\pm \mu^\mp$ channel Drell-Yan events are suppressed, since the Z

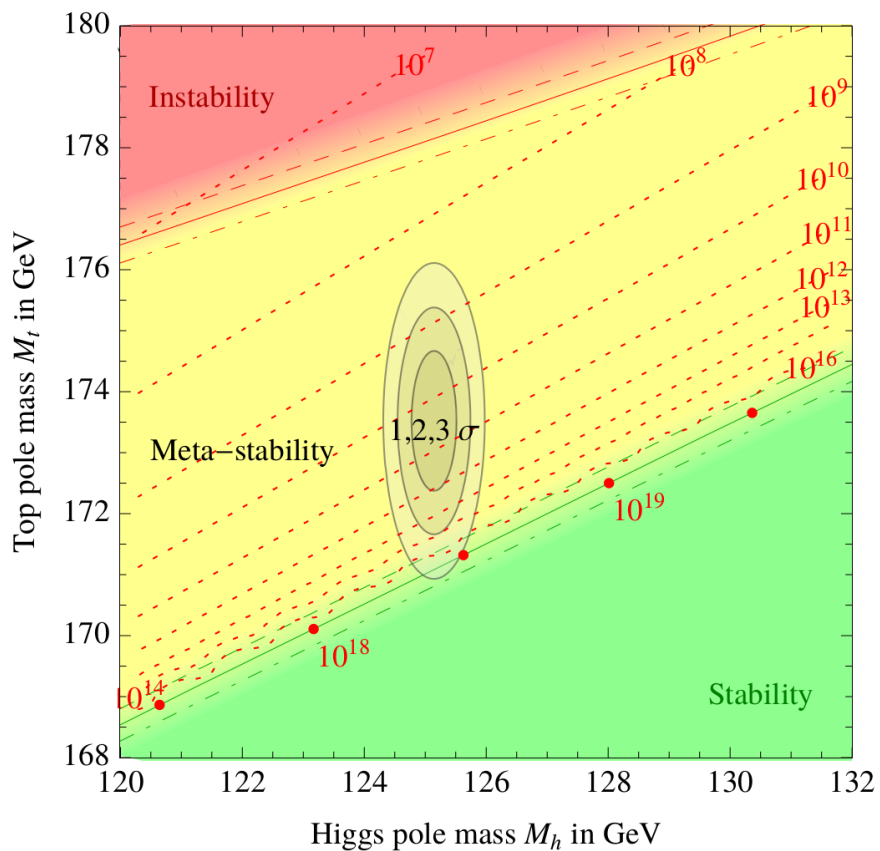


Figure 2.7: SM phase diagram depending on the mass of the top quark and the Higgs boson [42]. The boundary lines denote the uncertainty on the strong coupling $\alpha_S(M_Z) = 0.1184 \pm 0.0007$

boson cannot directly decay into opposite flavor leptons. The total cross section for the $pp \rightarrow \gamma^*/Z \rightarrow e^+e^-/\mu^+\mu^-$ process is calculated to be $\sigma_{\text{DY}} = 28.6 \text{ fb}$ for $m_{ll} < 10 \text{ GeV}$ at NNLO with FEWZ 3.1 [44].

Events with W bosons are produced via the electroweak interaction, similar to Drell-Yan events [45]. In this case the W boson decays into a lepton and a neutrino and two b quarks can be the result of initial state radiation. Since there is only one lepton in the final state, the contribution of W+jets events is strongly suppressed in the dilepton channel. An additional jet can be reconstructed as a lepton, but this happens rarely. The cross section for $pp \rightarrow W \rightarrow l\nu_l$ is calculated to be $\sigma_W + jets = 61 \text{ fb}$ at NNLO with FEWZ 3.1 [44].

Events where two bosons are produced (WW, WZ and ZZ events)[46] are another background for t̄t events in the dilepton channel. They can easily have 2 leptons in the final state, depending on the decay. These events can also contribute in the opposite flavor channel, especially when both bosons decay into leptons. The cross sections for WZ and ZZ production are calculated at NLO with MCFM [47, 48] to be $\sigma_{WZ} = 45 \text{ pb}$ and $\sigma_{ZZ} = 15 \text{ pb}$. The cross section for WW production is calculated at NNLO to be $\sigma_{WW} = 119 \text{ pb}$ [49].

Single top production with an associated W boson can result in a final state that has the same signature as the t̄t signal process (see Section 2.2.1). The process is hard to distinguish from the t̄t signal experimentally, but its cross section is small compared to the t̄t production cross section. The cross section is calculated at NLO and NNLL to be $\sigma_{tW} = 71.2 \text{ pb}$ [50].

2.4 Simulation

The simulation of events involves multiple algorithms, most of which are shown in Figure 2.8.

The hard interaction for a given process like the production of t̄t in proton-proton collisions is simulated by the matrix element generator. This algorithm calculates the scattering amplitude of a given process and the kinematic properties of the resulting partons. A large number of events is needed to avoid any bias due to the probabilistic nature of these distributions. The interaction itself is calculated at a fixed order of QCD and can include additional radiation of quarks or gluons from the initial as well as the final state. In the case of t̄t events, the matrix element generator also calculates the decay of the top quarks and the W bosons including the impact of spin correlations.

Since the particles in the initial state of the hard process are the constituents of the proton, the probability to find a given constituent in a proton with a certain fraction of energy needs to be known. This probability is given by Parton Distribution Functions (PDFs) that predict the energy fraction of a given quark or gluon that is part of the proton. In order to avoid singularities in the PDF calculation as well as in the hard interaction, scales

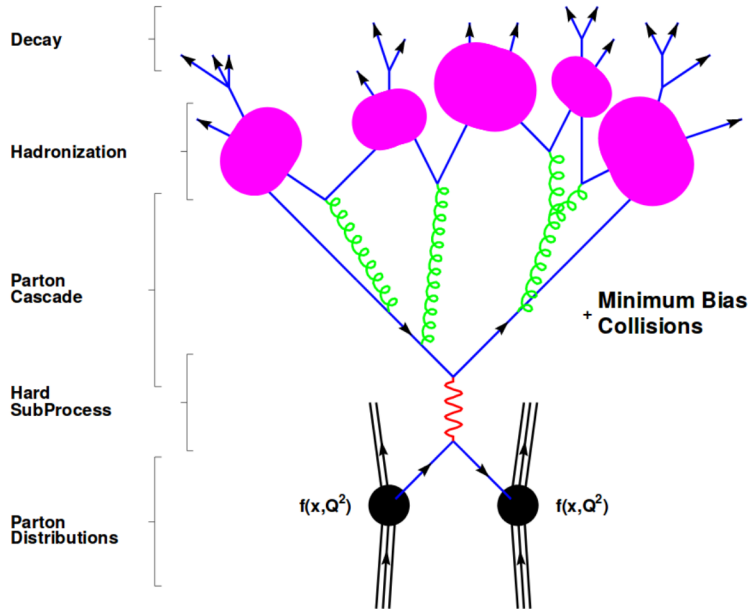


Figure 2.8: Illustration of a simulated event split in multiple steps. Starting from the protons and the PDF continuing with the hard interaction, the parton shower, the hadronization and the decay of the hadrons [51].

for the calculations of these divergences are introduced. For the calculation of the proton substructure the factorization μ_F is used, while the scattering amplitude calculation uses the renormalization scale μ_R . The value of these scales is normally motivated by the mass of the heaviest particle involved in the process.

Radiation beyond the scale of the matrix element generator is simulated by parton shower algorithms. The radiation is calculated at a scale that can be set separately for initial and final state radiation. The parton shower algorithms generally follow phenomenological models and principally include QCD calculations up to all orders. However, the parameters of these models are commonly tuned to match data from previous measurements.

As indicated by the name, the parton shower also simulates the showering of the partons that are the result of the hard process. Especially quarks and gluons carrying a color charge contribute to further radiation forming hadronic showers. These parton showers start from a maximum scale and evolve until a minimum scale on the order of a few GeV.

The combination of radiation of matrix element generator and parton shower can lead to double counting of radiation when the phase space overlaps. This double counting can be minimized by using a matching procedure which varies according to the generator of parton shower that is used.

After the parton shower is cut off by the scale, the resulting parton showers form color neutral hadrons. This process is called hadronization and is part of the parton shower algorithm. Again, the hadronization is based on phenomenological methods, the settings of which have to be tuned.

The proton constituents not involved in the hard interaction are called proton remnants. The interaction of these proton remnants usually involve low energy processes and form the underlying event (UE). The UE modeling is again tuned to data and included in the Parton Shower algorithm.

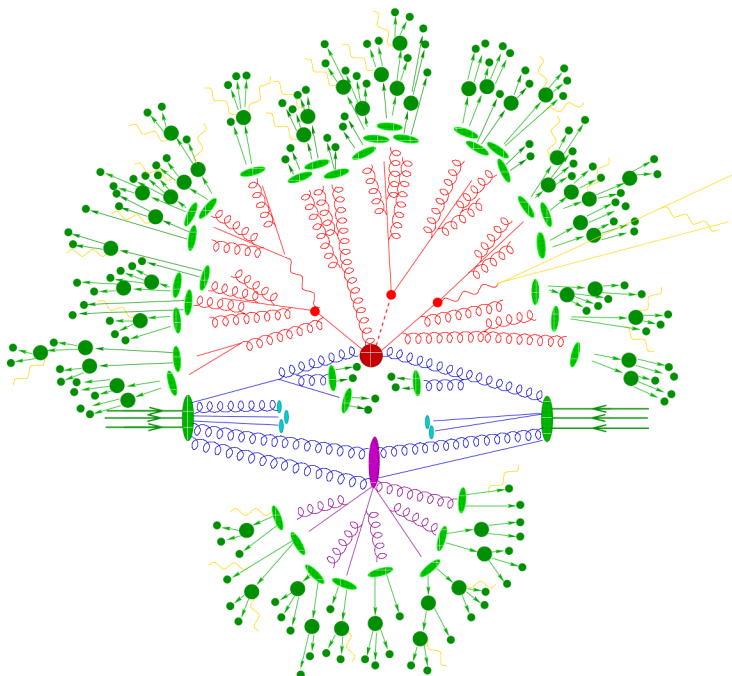


Figure 2.9: Representation of a simulated event from the Sherpa generator. It includes the hard interaction as well as showering, hadronization and underlying event [52].

A whole event including the hard process and the parton shower is illustrated in Figure 2.9 showing the production of a top quark pair in association with a Higgs boson. The incoming protons on the left and right sides are shown in the middle, with the blue gluons representing the initial state of the hard interaction. The large red circle stands for the hard interaction, with the initial state radiation shown in blue below. The partons resulting from the hard interactions are shown above the hard process with smaller red circles. The final state radiation of gluons is also shown in red, while additional radiation of photons is shown in orange. The partons from the parton shower hadronize as illustrated by the green ellipses.

The hadrons then decay into further hadrons. Below the whole interaction, the underlying event is shown in violet.

The last part of the simulation is the modeling of the detector response which includes modeling the complete detector, simulating the interaction of particles with the detector material and the corresponding response of the detector electronics. The full response of all detector subsystems including the trigger system is modeled for each event.

In this analysis the main generator is PowHEG (v. 2) [53–55], which calculates the relevant process at NLO. It is used for the simulation of the $t\bar{t}$ signal [56] as well as for the tW [57] and the Drell-Yan [58, 59] background process. The W+jets process is generated using MG5_AMC@NLO 2.2.2 [60, 61] at NLO including up to two additional jets. The diboson background samples are generated with PYTHIA 8.2 [62]. All samples are simulated with the NNPDF3.0 [63] PDF set.

PYTHIA 8.2 is also used as parton shower algorithm for all samples. The CUETP8M2T4 tune [64, 65] is used for the simulation of the signal and the tW and Drell-Yan backgrounds. The tuning is optimized for top physics by including $t\bar{t}$ data taken with the CMS detector at a center of mass energy of 8 TeV. For the remaining backgrounds, the standard tune for CMS CUETP8M1 tune is used. GEANT 4 [66] is used to simulate the detector response for all samples.

The relevant cross sections for the relevant processes are taken from specific theory calculations as described in Section 2.3.

After describing the theoretical motivation for the measurement of the $t\bar{t}$ production cross section in this chapter, the next chapter describes the experimental setup with the LHC and the CMS detector.

Chapter 3

The LHC and the CMS experiment

3.1 The Large Hadron Collider

The LHC, situated at CERN in the Geneva area, is a circular hadron accelerator with a circumference of 27 km, that is designed for a collision energy of $\sqrt{s} = 14 \text{ TeV}$ [67]. This analysis uses data from proton-proton collisions taken in 2016 where the LHC reached a center of mass energy of $\sqrt{s} = 13 \text{ TeV}$. The protons are assembled in bunches and accelerated to an energy of 450 GeV by various pre-accelerators before being injected into the LHC. The two beams in the LHC run in opposite directions and are kept on their path by 2136 superconducting dipole magnets.

Collisions are induced at four points along the ring of the LHC, as shown in Figure 3.1. The four main experiments are situated at these interaction points. The ALICE (A Large Ion Collider Experiment) experiment is designed for heavy ion collisions resulting in events with a very high track multiplicity. LHCb (Large Hadron Collider beauty) is focused on heavy flavor physics. The two multi purpose experiments ATLAS (A Toroidal LHC Apparatus) and CMS (Compact Muon Solenoid) are designed to measure and search for low cross section processes.

The instantaneous luminosity \mathcal{L} is a measure for the rate of pp collisions. It is related to the rate of events \dot{N} of a process k through the cross section σ_k :

$$\dot{N}_k = \mathcal{L} \cdot \sigma_k. \quad (3.1)$$

The luminosity itself can be calculated from the beam properties:

$$\mathcal{L} = \frac{N_b \cdot N_p^2 \cdot v}{\Sigma_x \Sigma_y}. \quad (3.2)$$

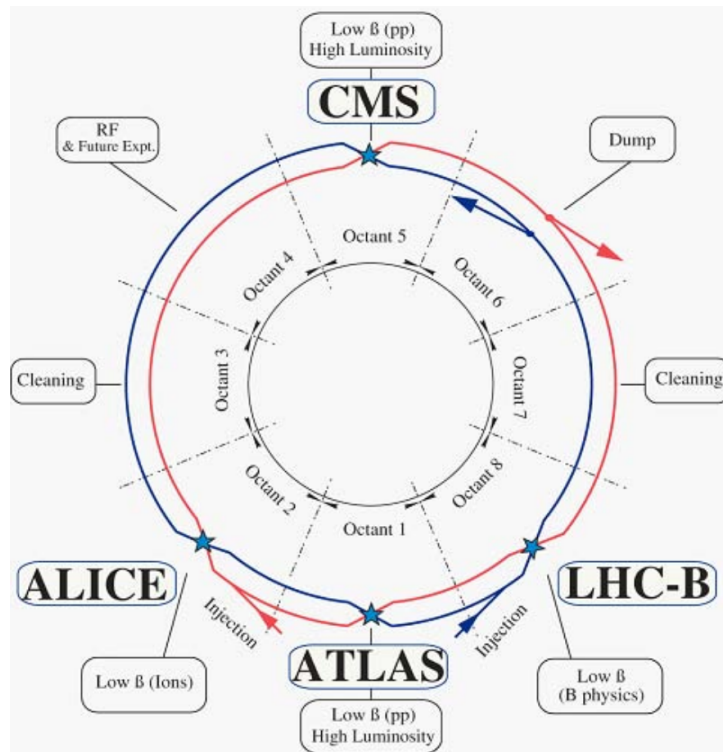


Figure 3.1: Schematic of the LHC ring showing the two beams as well as the four major experiments. It also shows the injection points as well as the cleaning point and the beam dump [67].

Here, N_b stands for the number of bunches, N_p for the number of protons per bunch and v for the rotation frequency of the LHC. Σ_x and Σ_y are the effective widths of the overlap of the two beam profiles in x or y direction respectively. The luminosity is determined by measuring those beam profiles. Special LHC conditions are used to calibrate the relevant parts of the detector for this measurement of the beam profiles. In a Van-der-Meer scan [68] the two beams are shifted against each other, which allows to calibrate the detector for known configurations of $\Sigma_{x,y}$. The calibrated detectors are then used to determine the instantaneous luminosity during data taking.

In this analysis the data corresponds to an integrated luminosity of $35.9 \pm 0.9 \text{ fb}^{-1}$ taken at a center of mass energy of $\sqrt{s} = 13 \text{ TeV}$.

3.2 The CMS detector

The CMS experiments detector is a multi purpose detector for the study of particles from proton-proton, proton-lead and lead-lead collisions. With a length of 21.6 m and a diameter of 15 m it is relatively small and dense for its weight of 14000 tons [69], thus the name 'compact'.

The detector is built of multiple radial layers ("onion structure") and split into a barrel region in the middle and two endcaps closing the detector structure, as shown in the overview in Figure 3.2. The innermost part of the detector is the tracker, followed by the electromagnetic and then the hadronic calorimeter. These parts of the detector are surrounded by the superconducting solenoid. The muon system is the last part of the detector and is situated outside the solenoid. It is interleaved with the iron return yoke of the magnet.

The solenoid provides a magnetic field of 3.8 T for the inner part of the detector (the tracker and calorimeters) and a field of about 2 T in the muon system. A total energy of 2.6 GJ is stored in 2168 loops of superconducting cables. This strong magnetic field leads to strongly bent tracks for charged particles, allowing a precise measurement of their momenta. The tracks of particles outside the magnet are bent in the opposite direction of those in the inner part.

The detector is described in a right-handed coordinate system with the origin in the interaction point. The z -axis points in the direction of the counterclockwise beam, the y -axis points vertically upwards and the x -axis radially points towards the center of the LHC ring. The φ angle is defined in the x - y plane, while the angle θ is defined in the y - z plane. Instead of θ the pseudorapidity η is used, since it is invariant under Lorentz transformation as long as the momentum of a particle is large compared to its mass ($|\vec{p}| \gg m$):

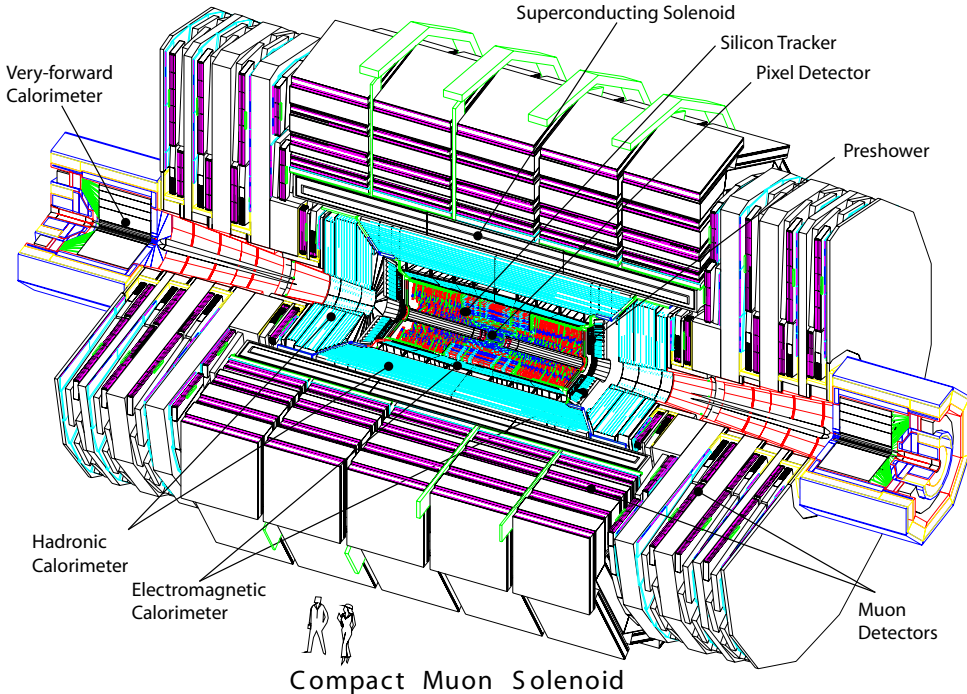


Figure 3.2: The CMS detector and its relevant subsystems. [70]

$$\eta = -\ln \tan \frac{\theta}{2}. \quad (3.3)$$

The subsequent sections describe the different parts of the detector including the triggering system that is used to select the collisions for which the data is stored for offline analysis.

3.2.1 The tracking system

The tracking system [69] is designed to measure both tracks and vertices with the highest possible precision. This requires high granularity and, in the LHC environment, a fast response.

The tracking system is comprised of two parts: the inner one with pixels, the outer one with strips. Its structure in the barrel as well as the endcaps is shown in Figure 3.3.

The first pixel layer is located at a radius of 4.4 cm in the barrel and at 34.5 cm in the endcaps. Both parts cover a range of $|\eta| < 2.5$. The barrel region includes three layers of pixel detectors and ten layers of strip detectors, while the endcap includes two layers of pixels and twelve layers of strips. The 66 million pixels measure $150 \times 100 \mu\text{m}$. The 9.6 million strips have a width of $80 - 180 \mu\text{m}$, together with the pixel detector that allows to separate even

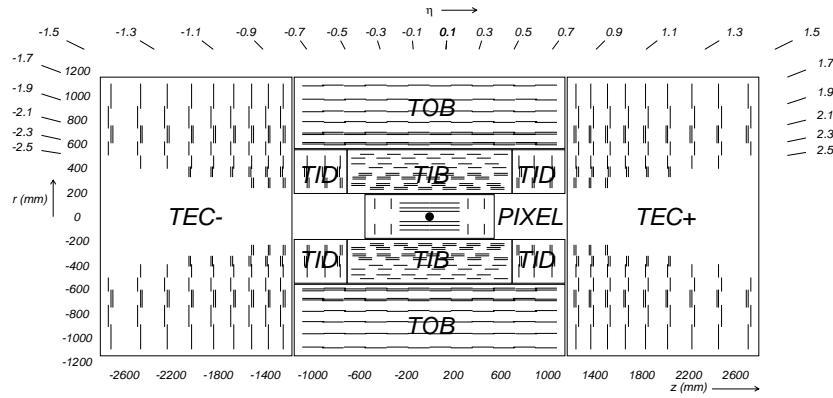


Figure 3.3: The tracking system of the CMS detector in the barrel and endcap regions. The sketch shows the pixel as well as the strip tracker. The strip tracker consists of the inner barrel (TIB), outer barrel (TOB), inner disks (TID) and endcaps (TEC) parts [71].

closely spaced particle trajectories. The position of each tracker part is precisely known from alignment analyses using tracks from collision events and cosmic muons [72].

The momenta of charged hadrons with a $p_T < 20 \text{ GeV}$ are measured with a resolution of 1% at an incidence of ninety degrees [73]. The relative resolution decreases for higher p_T , reaching a resolution corresponding to the energy resolution of the calorimeter at several hundred GeV. At low p_T , the resolution is dominated by multiple scattering of the particle in the tracker material [74]. At high p_T , the resolution decreases as the bend of the track is reduced making the p_T determination more difficult. The resolution in p_T is shown in Figure 3.4 for muons and charged pions. Since high p_T partons usually produce multiple charged hadrons of lower p_T through fragmentation, the tracker can still contribute significantly to the measurement of high- p_T jets.

3.2.2 The electromagnetic calorimeter

The electromagnetic calorimeter (ECAL)[69] measures the energy of electrons and photons that produce showers in the ECAL. These electromagnetic showers should be contained within the ECAL. Additionally, the high granularity of the ECAL helps separate the signals from different particles. A sketch of the structure of the ECAL is shown in Figure 3.5.

The ECAL is made of lead tungstate with the barrel region covering about $|\eta| < 1.5$ and the endcaps covering $1.5 < |\eta| < 3.0$. The crystals are 23(22) cm deep in the barrel (endcap) corresponding to about 26(25) radiation lengths. For electrons and photons up to an energy of 1 TeV, more than 98% of the energy of each particle is completely contained in the

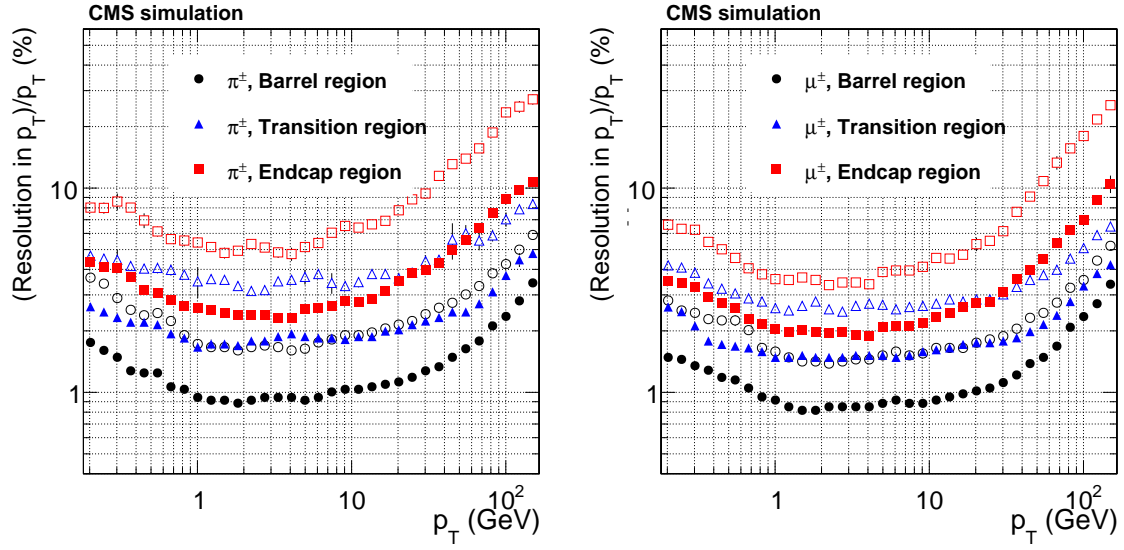


Figure 3.4: Resolution of track p_T resolution as a function of the track p_T for simulated charged pions (left) and muons (right) [74].

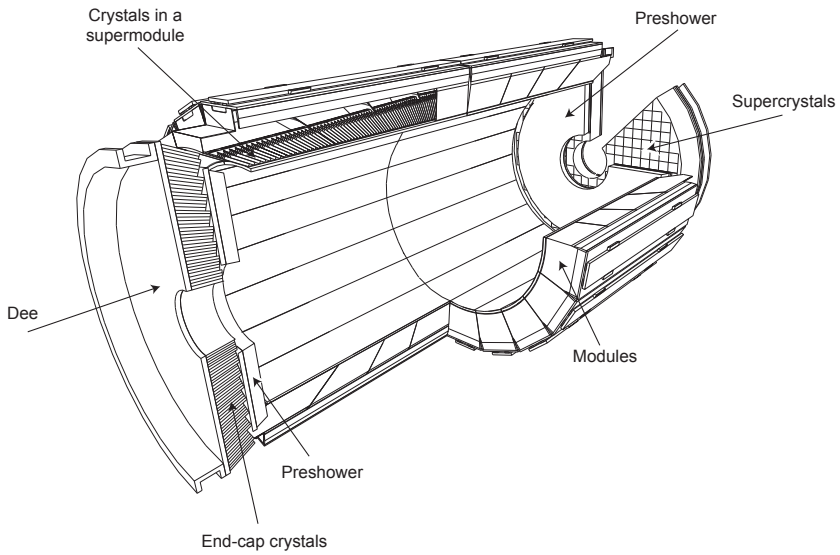


Figure 3.5: A sketch of the electromagnetic calorimeter showing the structure in the barrel and the endcaps as well as the preshower detectors [75].

ECAL. The crystal depth also corresponds to roughly one interaction length. This implies that approximately two thirds of hadrons start their shower in the ECAL.

The front of the crystals has a size of $2.2 \times 2.2 \text{ cm}^2$ in the barrel and $2.9 \times 2.9 \text{ cm}^2$ in the endcaps. This size corresponds to the Moliere radius of lead tungstate of 2.2 cm. The electronic noise in the ECAL is measured to be about 40 MeV per crystal in the barrel and about 100 MeV in the endcaps.

The energy resolution for an electron measured in the ECAL can be parameterized depending on the electron energy as follows [73]:

$$\frac{\sigma}{E} = \frac{2.8\%}{\sqrt{E/\text{GeV}}} \oplus \frac{12\%}{E/\text{GeV}} \oplus 0.3\%. \quad (3.4)$$

The first term represents a stochastic term caused by fluctuations such as the amount of intrinsic variations of the showering itself. The second term is caused by noise from the electronics and the constant third term is related to calibration uncertainties, detector non-uniformity and radiation damage.

Photons in jets have a typical energy range of 1 – 50 GeV where the resolution of the ECAL is excellent.

The so-called preshower detector is situated in front of the two ECAL disks in the endcaps. The preshower contains two layers: The first is a lead radiator followed by silicon strip sensors. The detector has a much higher granularity than the ECAL, which allows measuring the initial position of a shower from an electron or photon with a high precision. The purpose of the preshower is to discriminate between neutral pions decaying into two photons and prompt single photons. Additionally, a coincidence between ECAL and preshower can be used to identify electrons and photons. The performance of the preshower is degraded through a large number of neutral pions caused by hadrons interacting with the tracker material.

3.2.3 The hadronic calorimeter

The hadronic calorimeter(HCAL) [69] is a sampling calorimeter consisting of layers of brass absorbers and plastic scintillators. Its purpose is to measure the energy of hadronic showers with a high precision. Additionally, it prevents the hadronic showers from leaking into the muon system. In the barrel it covers a range of $|\eta| < 1.3$ with a corresponding endcap coverage of $1.3 < |\eta| < 3.0$. In the barrel the HCAL is about six interaction lengths thick at normal incidence, increasing to over ten interaction lengths at lower incidence angles. The whole HCAL is shown as a sketch in Figure 3.6.

The outer hadronic calorimeter (HO) is situated outside the solenoid coil, increasing the interaction length as an additional absorber. In the very central region, the interaction length

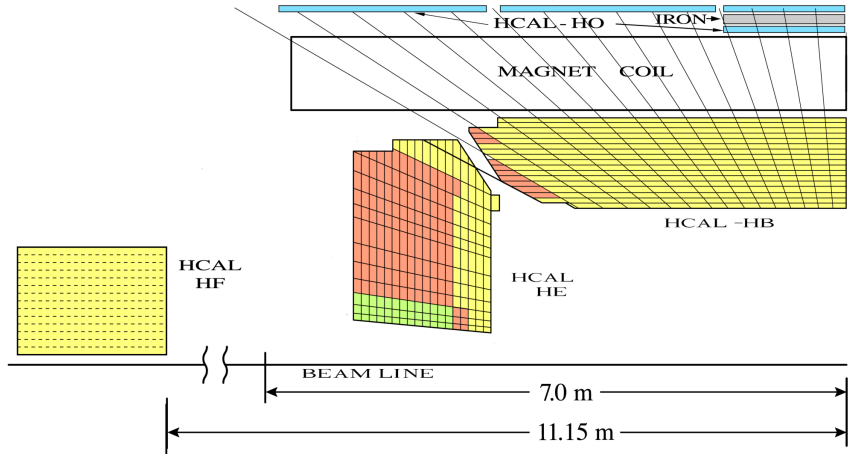


Figure 3.6: A quarterly schematic of the hadronic calorimeter showing the HCAL in the barrel(HB) and the endcaps(HE), the outer HCAL(HO) and the forward HCAL(HF) [76].

is further increased by additional layers of steel. Including the ECAL, the total calorimeter system has a thickness corresponding to a minimum of about twelve interaction lengths in the barrel and ten interaction lengths in the endcaps. The individual towers of the ECAL have a cross section of $\Delta\eta \times \Delta\varphi = 0.087 \times 0.087$ in the central region of $|\eta| < 1.6$ and a cross section of $\Delta\eta \times \Delta\varphi = 0.017 \times 0.017$ in the more forward region [69].

The electronic noise is measured to be about 200 MeV per tower [73]. The combined energy resolution for ECAL and HCAL has been measured with a pion beam to be

$$\frac{\sigma}{E} = \frac{110\%}{\sqrt{E/\text{GeV}}} \oplus 9\%. \quad (3.5)$$

The two parts of the hadron forward calorimeter (HF) are positioned in the very forward(backward) region of the detector at a distance of 11 m from the interaction point. It covers a region of up to $|\eta| \approx 5$. It consists of steel absorbers and quartz fibers of two different lengths. The long quartz fibers correspond to roughly ten interaction lengths. The difference in the signal from the short and the long fibers is used to estimate the hadronic and electromagnetic components of the shower.

3.2.4 The muon system

High energy muons mostly interact with matter through ionization. They are generally neither stopped by, nor decay within the detector, so the momentum can only be measured by reconstructing their tracks.

The purpose of the muon system as the outermost part of the detector is to identify muons and measure their momentum.

The muon system [69] consists of four layers with three steel layers of the return yoke of the solenoid between them. The central region is covered by Drift Tubes (DT) in the region of $|\eta| < 1.2$. The outer region is covered by Cathode Strip Chambers (CSC) in the region of $0.9 < |\eta| < 2.4$. Additionally, Resistive Plate Chambers (RPC) cover the range of $|\eta| < 1.6$. A sketch of the whole muon system is shown in Figure 3.7.

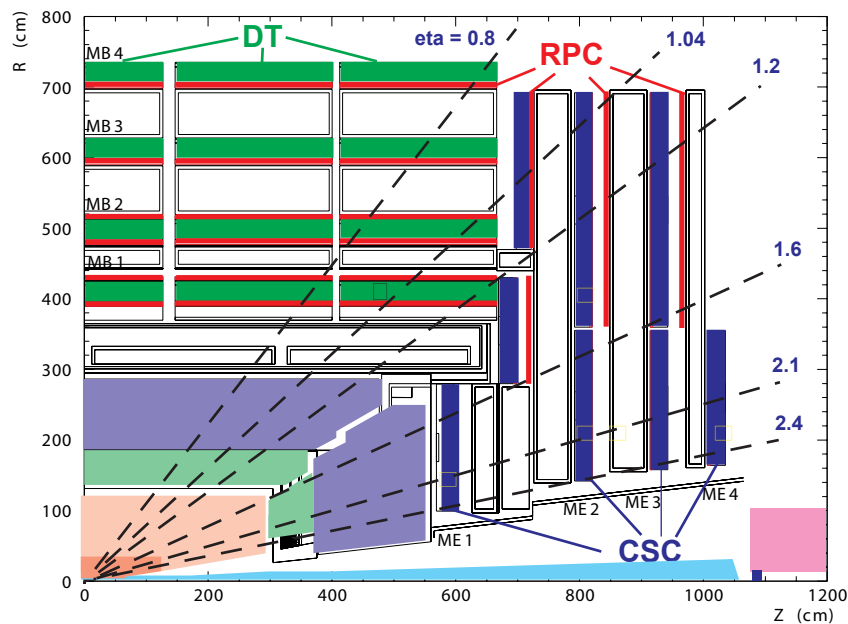


Figure 3.7: A quarterly schematic of the muon system showing the Drift Tubes(DT) in the central part, the Cathode Strip Chambers(CSC) in the outer part and the Resistive Plate Chambers(RPC) [69].

The DT chambers are filled with a mixture of argon and carbon dioxide. The chambers themselves contain layers which are rotated against each other, which allows measuring both the φ and the η projection of the track. The DTs are also used for triggering.

The CSCs are positioned at a right angle with respect to the DTs. The single chambers consist of six gas gaps each. The two coordinates of the track are determined by radial cathode strips and perpendicular anode wires. The spatial resolution of both the CSCs and the DTs is in the range of $100 - 200 \mu\text{m}$, depending on η .

The RPC system consists of 480 chambers. Their very high time resolution in the sub nano second range allows them to be used for triggering and the association of muon tracks with a specific bunch crossing.

3.2.5 Triggering

The LHC delivers a collision rate of 40 MHz. In order to record the data, as it is measured by the detector, this data volume has to be reduced to a manageable size. This reduction is achieved by only keeping those events for further study in which a relevant result is observed. A two-tiered triggering system is used to reduce the final rate of events to 100 Hz. First the hardware-based Level-1(L1) Trigger is used to reduce the number of events for the software-based high-level trigger (HLT) [77, 78].

The L1 trigger consists of programmable electronics using information from the calorimeters as well as the muon system as shown in Figure 3.8. The L1 trigger is separated into the muon trigger and the calorimeter trigger. The tracking system is not used at this stage of triggering. The muon trigger combines track information from the CSCs, DTs and RPCs. It uses information from the calorimeters to measure the isolation of the muons. The calorimeter trigger combines the ECAL, HCAL and HF. Besides muon triggers, algorithms targeting electrons/photons, taus, jets and the overall energy deposition in the detector are used. Requiring a muon to be contained within a jet allows to target jets originating from a b quark, where the B hadron decays further into a final state containing a muon. The L1 trigger has a maximal latency of 3.8 μ s in which a trigger decision has to be delivered to the HLT.

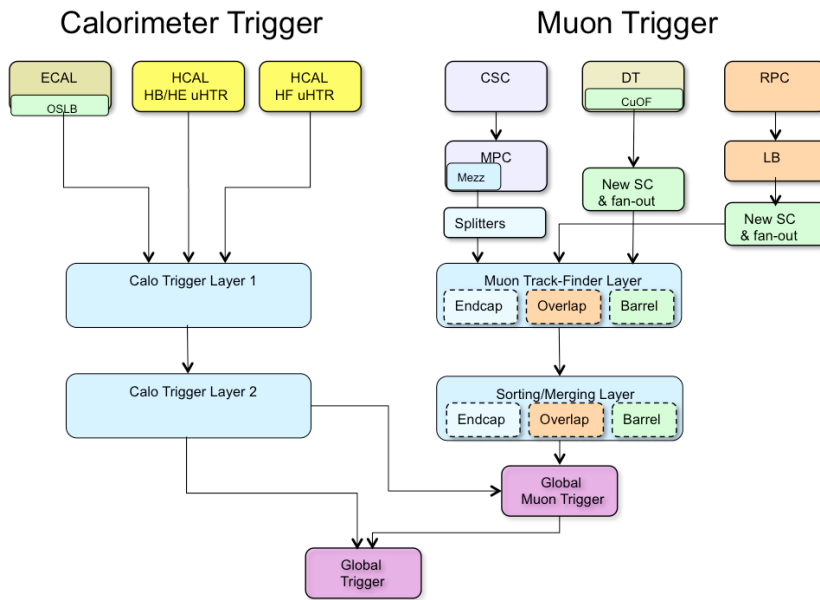


Figure 3.8: Data flow of the L1 trigger system showing the combination of information from the different subsystems [78].

The HLT is the second step of the triggering system. It reduces the number of events from 100 kHz to 100 Hz. Compared to the L1 trigger, it uses more sophisticated reconstruction techniques, which are generally close to the final reconstruction that is used for analysis. The HLT starts from the L1 decision. It then combines information from the complete detector, including tracks, to reconstruct the respective particle in the path. Finally, further thresholds on the kinematics, the isolation or the reconstruction quality are required. These steps are performed sequentially. If one step fails the sequence is stopped.

In order to be able to reduce the rate of certain trigger paths for both the L1 and the HLT, some trigger paths only consider a fraction of events. This technique is called prescaling. If a trigger path is prescaled by two it only considers every second event.

A detailed study of the lepton triggers which are used in this analysis is presented in Chapter 5. The measurement of the trigger efficiency is discussed as well.

The next chapter describes the reconstruction of particles from the detector information.

Chapter 4

Reconstruction

Before it is used in the measurement of a physics process, such as $t\bar{t}$ production, the data taken by the detector are reconstructed. The reconstruction is performed offline, opposed to the online reconstruction for the trigger system. The purpose of the reconstruction is to identify particles or groups of particles like jets, together called physics objects, and measure their kinematic properties. Observables like the p_T and η of a particle are basic parameters of interest, but the reconstruction also includes other features like the charge or the isolation of particles.

Following a general introduction, this chapter describes the reconstruction for the different objects starting with tracks and vertices in Section 4.1. The reconstruction of electrons is described in Section 4.2. The reconstruction of muons is described in Section 4.3. The reconstruction of jets is described in Section 4.4, while Section 4.5 describes the identification of jets originating from a b quark.

As illustrated in Figure 4.1, different particles deposit energy in different parts of the detector. The tracks of charged particles are bent by the magnetic field, while neutral particles are unaffected. Similarly, only charged particles leave a signal in the tracker, as particles without a charge do not ionize the tracker material. Electrons and photons deposit the main amount of their energy in the ECAL, whereas neutral and charged hadrons mainly deposit energy in the HCAL. Muons are mainly detected by muon system in the outermost parts of the detector and in the inner tracker.

Physics objects are reconstructed by combining the information from all parts of the detector using the Particle Flow algorithm [73]. The tracks from the tracker and the muon system and the clusters from the calorimeters are combined to identify each final state particle. This includes charged and neutral hadrons within jets. The Particle Flow algorithm allows for a more precise measurement of the energy and (for charged particles) the direction of

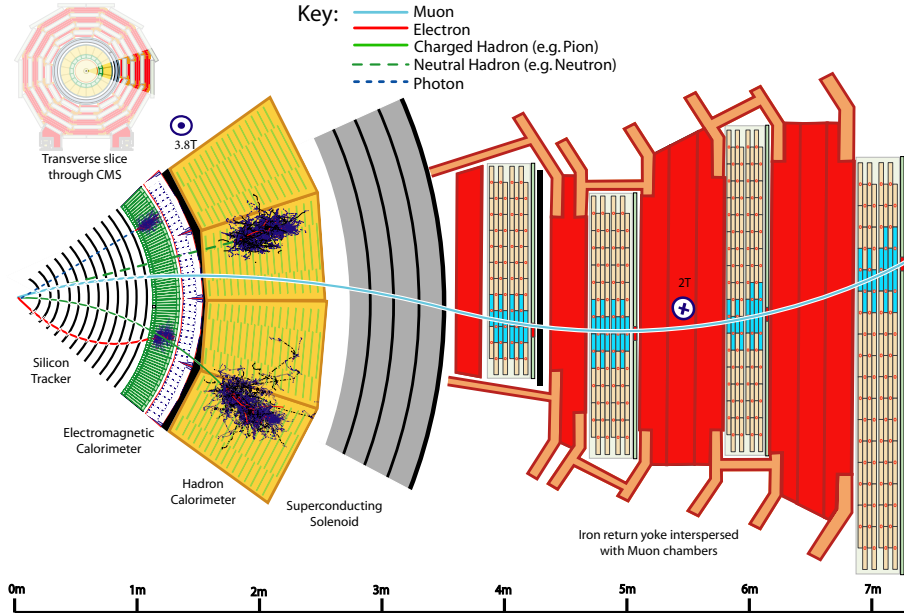


Figure 4.1: Illustration of the interaction of specific particles in a transverse slice of the CMS detector [73].

particles. It also allows to calibrate and to validate the different parts of the detector. All reconstruction methods described in this chapter are based on Particle Flow techniques.

In general, the probability to correctly reconstruct a particle can be different in simulation and data. Typically, these differences are small, since the detector response is modeled and the reconstruction algorithms for data and simulation are the same. Nevertheless, small differences remain, which are corrected in simulated events. These corrections are typically defined separately for each physics object by measuring the reconstruction efficiency independently in simulation and measured data. The simulation is then corrected to fit the efficiency measured in data. Resolution effects are corrected in a similar manner.

4.1 Tracking and vertex reconstruction

The aim of the tracking algorithm is to provide the properties of charged particles, for example the origin, the transverse momentum and the direction [73]. The CMS track reconstruction itself is based on Kalman-Filtering [79] and consists of three steps starting with a seed of a few hits consistent with the trajectory of a charged particle. The subsequent steps are the collection of hits from all tracker layers along the trajectory and the fitting of the track to precisely determine the kinematic properties of the particle. The tracking efficiency can be

increased by repeating the track finding with different conditions [74], such as the quality requirements of the initial seed or the result of the fit.

The gain in efficiency through iterative tracking is presented in Figure 4.2 showing the efficiency and the misreconstruction rate for tracks depending on the p_T of the charged particle for multiple different tracking algorithms. The efficiency is determined from simulation where tracks are considered to be reconstructed correctly if they can be associated to a simulated particle. Correspondingly, misreconstructed tracks cannot be associated to a simulated particle. Including all iterations shows the highest efficiency and a comparative mistag rate. In general, the efficiency decreases dramatically for high p_T tracks (see Section 3.2.1), especially for tracks with $p_T > 100 \text{ GeV}$. As shown in Figure 4.2, the misreconstruction rate increases with higher p_T , but the effect can be mitigated when the rest of the detector is taken into account.

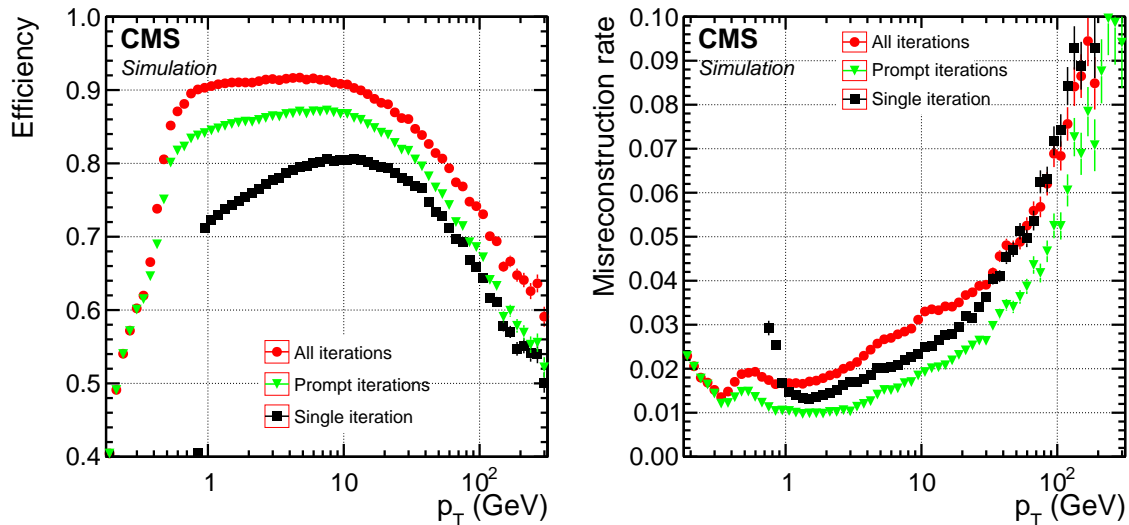


Figure 4.2: Performance of the iterative tracking procedure [73]. The left figure shows the tracking efficiencies depending on the p_T of the charged particle for multiple different tracking approaches. The right figure shows the rate to misreconstruct a track depending on the p_T of the charged particle for multiple different tracking approaches. Prompt iterations require at least one hit in the pixel detector.

The origins of the tracks along the beam axis are considered as primary vertices and sorted according to the p_T of the associated tracks. The vertex with the highest p_T is assumed to be connected to the hard interaction. Additional vertices are caused by additional proton-proton collisions occurring in the same bunch crossing as the hard interaction. This so-called pile-up leads to an average of 16 primary vertices in the 2016 dataset. In order to suppress

the influence of pile-up, tracks originating from a pile-up vertex are removed from the reconstruction. This applies to tracks within jets as well as other particles.

4.2 Electron reconstruction

The reconstruction of electrons is based on the combination of information from the tracker and the calorimeters. Both electron and photon reconstruction require an ECAL cluster with a significant energy deposit. For an electron, this cluster also contains the energy deposited by the bremsstrahlung photons. The energy deposited in the HCAL region corresponding to the ECAL cluster is required to have less than 10% of the energy deposited in the ECAL. This requirement allows to separate electrons and photons from hadrons. In order to be identified as an electron, a physics object needs a cluster of ECAL energy to be associated with a track. In case no track is found, the physics object is identified as a photon.

The association between ECAL cluster and track is either seeded from both the tracker or from the ECAL. The combination of both approaches increases reconstruction efficiency as shown in Figure 4.3. The main gain of efficiency applies to electrons with a p_T below 10 GeV, but even for electrons with higher p_T a few percent of efficiency are recovered. Both the ECAL cluster and the track need to fulfill certain quality criteria applying to shower shape or track fitting.

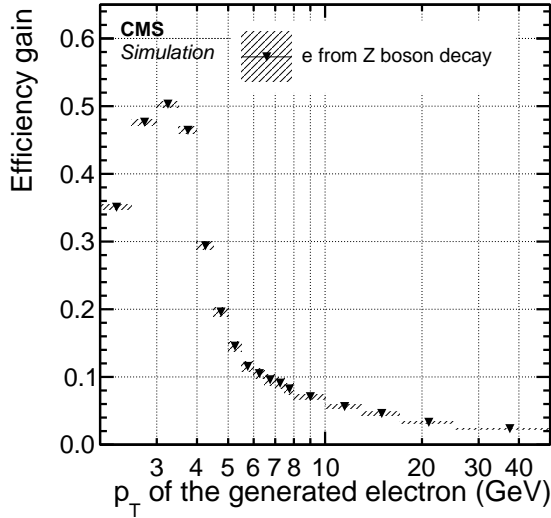


Figure 4.3: Absolute gain in efficiency of the tracking in electrons when adding tracker-based seeding as a function of electron p_T [73]. The efficiency is measured in simulated Z boson decays.

Electrons also need to be isolated: The energy deposited in a cone around an electron is required to be below 6% of the p_T of the electron. The relative isolation is sensitive to contributions from pile-up. Contributions from charged particles that are not coming from the vertex of the hard collisions are subtracted from the isolation. The pile-up contribution from non-charged particles is harder to determine. It is estimated according to the general energy density in the event and subtracted from the isolation. The combined efficiency to identify an electron is shown in Figure 4.4 as a function of the p_T and the η of the electron. It is measured with the tag-and-probe method, described in Section 5.3. As shown in Figure 4.4, the efficiency depends more strongly on the p_T of the electron than on its η coordinate. The efficiency measured in data agrees with the one measured in simulation within 10%.

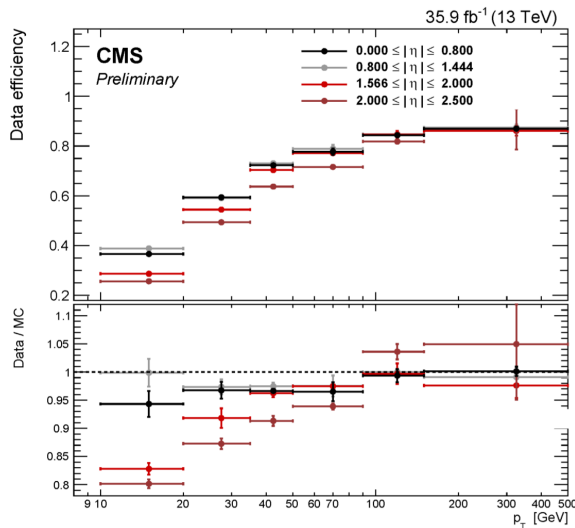


Figure 4.4: Efficiency of the electron identification depending on the p_T and the η of the electron[80]. The upper panel shows the efficiency measured in data. The lower panel shows the efficiency in data divided by the efficiency in simulation.

The simulation is corrected according to the efficiency measurement in data. For each reconstructed electron, an η and p_T dependent weight is assigned to each event, so that the simulation is rescaled to match the data. The weight itself is calculated by dividing the efficiency in data by the efficiency in simulation: $w = \epsilon_{\text{data}}(p_T, \eta)/\epsilon_{\text{MC}}(p_T, \eta)$. A correction of the same type is applied for the reconstruction of muons and the efficiency to trigger an event.

The electron energy is corrected to cover known biases from the electromagnetic calorimeter. Additionally, the energy resolution is found to be higher in simulation when compared to data. Those biases are especially visible when comparing the Z boson mass peak in data and simulation [81]. Since the mass and width of the Z boson are extremely well known

from LEP, and the behavior of these events in the detector is well understood, they allow correcting the electron energy and resolution in simulation.

4.3 Muon reconstruction

Muons leave tracks in both the tracker and the muon system. The track in the muon system has to be matched to a track in the tracker to reconstruct a global muon. The tracks need to be compatible with each other when propagated to a common surface. Further quality requirements are applied to the inner track in the tracker.

Similar to the electrons, the muons are also required to be isolated. The energy in a cone around the muon(isolation) is required to be below 15% of the muon p_T . This energy is measured from charged particles coming from the primary vertex, neutral hadrons or photons. The impact of the pile-up on the neutral hadron and photon components is estimated to be half of the contribution from charged pile-up and is subtracted from the total isolation. The efficiency (measured with the tag-and-probe method, see Section 5.3) for the identification and isolation requirements used in the analysis is shown in Figure 4.5. The efficiency is above 90% over nearly the whole range of η and p_T .

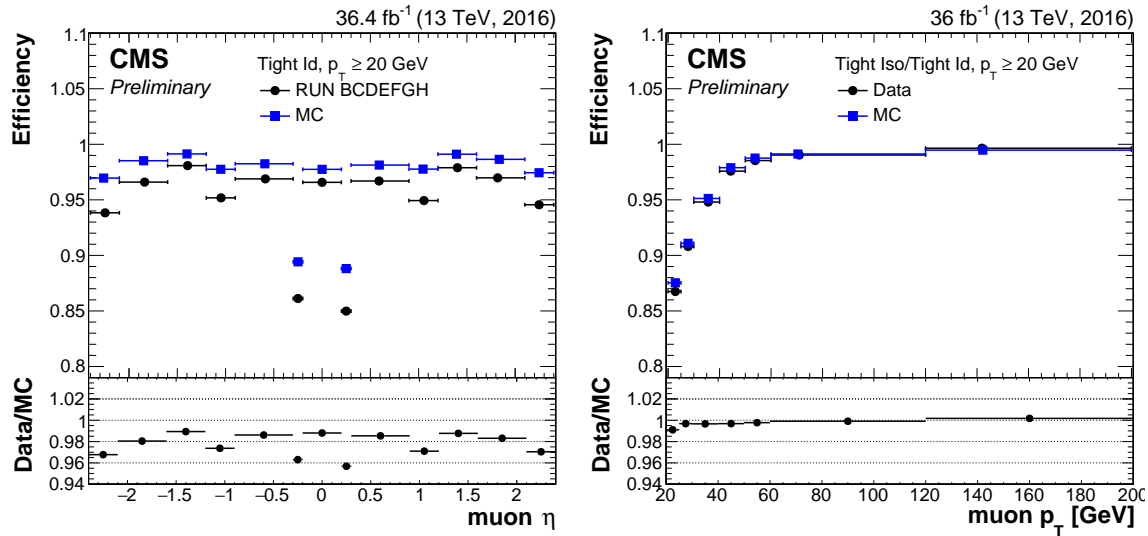


Figure 4.5: Efficiency of the identification (left) and isolation (right) for muons depending on η (left) and p_T right of the muon. The upper panels show the efficiency in data and simulation, while the lower panels show the ratio.

As described above for electrons, the small discrepancies of the simulation are corrected by event reweighting.

The resolution and scale of the p_T of the muons in data and simulation can be investigated by comparing the mass peak of the Z boson depending on the η and ϕ of the two leptons. Additionally, the forward and backward charge asymmetry is sensitive to differences between data and simulation. The p_T of the muons is then corrected in simulation according to the disagreement observed. The corrections depend on the kinematics of the muon, its charge, the properties of the track of the muon and the simulated p_T of the muon before the detector simulation.

4.4 Reconstruction of jets

Jets are clustered from the individual particles reconstructed from the Particle Flow algorithm [82]. The clustering uses the anti- k_T algorithm [83] as implemented in FASTJET [84] with a distance parameter of $R = 0.4$. The impact of pile-up is reduced by removing charged hadrons not originating from the primary vertex [85]. Neutral particles originating from pile-up are taken into account by correcting the jet 4-momenta for each event based on the jet area [86, 87].

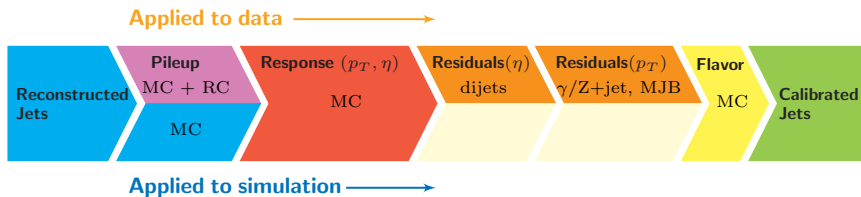


Figure 4.6: Illustration of the sequential jet energy scale corrections applied to measured data and simulation [88]. The flavor correction is not applied.

The corrections for the jet energy scale are illustrated in Figure 4.6. They are applied sequentially to both measured data and simulation [88, 82]. The first step corrects for remaining contributions from pile-up, which are determined by comparing jets in simulated events with and without the simulation of additional pile-up collisions. In data, an additional correction is derived from the Random Cone method in zero bias events, where the energy deposition in randomly distributed areas is measured [89]. These areas (cones) have the same geometrical properties as the cones used for the jet clustering, which allows to measure the average pile-up contribution to a jet depending on η and ϕ . The correction is parametrized depending on the energy density in the event, the jet area and the kinematic properties of the jet. The pile-up correction also depends on the data taking period.

In the next step, the reconstructed jet energy in the simulation is compared to the energy of a simulated jet before the detector simulation. Neutrinos are explicitly excluded, since they cannot be measured in the detector. The correction depends on p_T and η of the jets and is applied to both measured data and simulation.

The last correction is only applied to data (the flavor corrections shown in Figure 4.6 are not used). It corrects for remaining differences in the jet response between data and simulation, which are determined from dijet events. The correction depends on the p_T and η of the jets.

The different jet response in measured data and simulation is illustrated in Figure 4.7 showing the response measured in events containing photons and jets, and Drell-Yan events. It also shows the uncertainty of the jet energy scale corrections. The numbers shown here are derived only for a subset of the full dataset and do not correspond to the corrections used later in the measurement of the $t\bar{t}$ production cross section.

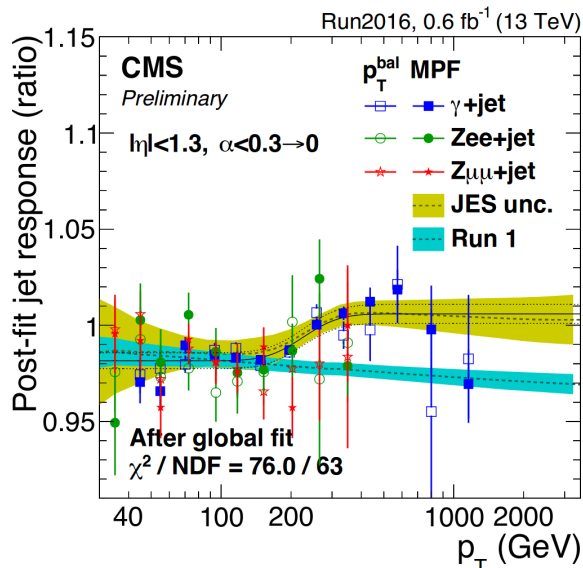


Figure 4.7: The data to simulation ratio of the jet response measured in photon + jets and Z + jets events for a subset of data [90]. The uncertainty for this dataset as well as the uncertainty for the dataset taken by the CMS collaboration in Run 1 of the LHC are shown as colored bands.

The jet energy resolution is determined from the width of the jet response function, defined as the ratio between the p_T of a simulated jet before and after reconstruction. It is found to be different in measured data and simulation. The p_T of the jets in simulation is rescaled depending on the simulation by the following factor:

$$SF = 1 + (SF_{\text{reso.}} - 1) \frac{p_T - p_T^{\text{gen}}}{p_T}. \quad (4.1)$$

Here, $SF_{\text{reso.}}$ denotes the resolution scale factor and p_T^{gen} stands for the p_T of the simulated jet before the simulation of the detector response.

If all particles from a collision are correctly reconstructed, the overall p_T of the events should be balanced, due to momentum conservation and the initial state particles not having momentum in the transverse direction. Particles that cannot be reconstructed, such as neutrinos, lead to an imbalance in the overall measured transverse momentum. This quality is often referred to as missing transverse energy E_T^{miss} [91]. The E_T^{miss} is reconstructed by a multivariate analysis using all other physics objects as well as unassociated energy deposits. It also takes the resolution of the other objects into account. Since it is not used in the $t\bar{t}$ production cross section measurement, it is not described in further detail.

4.5 Identification of b jets

The large lifetime of a B hadron leads to a signature in which the decay vertex is often displaced from the original interaction. These secondary vertices together with the displaced tracks and the properties of the jet itself are combined in the CSVv2 algorithm to identify jets originating from a b quark [92]. Sensitive variables are combined into a neural network which is trained against both jets originating from light jets as well as jets originating from c quarks. The result is a single value (discriminator) with the cut chosen according to the desired efficiency and background rejection.

The tight working point chosen for this analysis has a very low rate of misidentifying a light jet as a b jet (mistag rate) with $\sim 0.1\%$. The efficiency to correctly identify a jet from a b quark as a b jet is measured to be $\sim 40\%$ [92]. These numbers are obtained for jets with an average transverse momentum of $p_T = 70$ GeV. A lower efficiency can be expected for b jets with a lower p_T .

The efficiency in simulation is corrected according to the efficiency measured in data. The difference measured in events containing both muons and jets and in $t\bar{t}$ events is shown in Figure 4.8.

The difference between data and simulation is corrected by applying event weights. These event weights are not calculated directly from the scale factor but depend on the number of jets and the efficiency to correctly identify a b jet in data as well as simulation. The weights are calculated as the ratio of the probabilities to find b tagged jets in data and simulation:

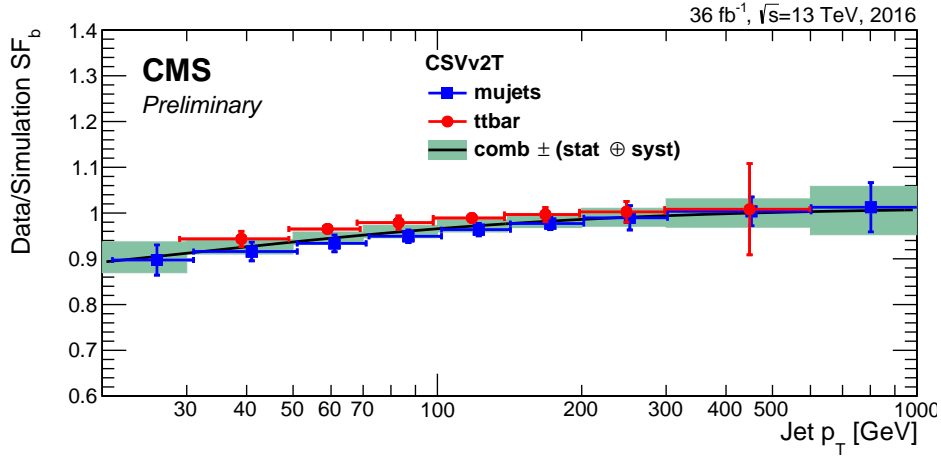


Figure 4.8: Scale factor between the b jet identification efficiency measured in data and simulation. The measurement is performed with events containing jets and muons and in $t\bar{t}$ events [93]

$$P(\text{Data}) = \prod_{i=\text{tagged}} \epsilon_i^{\text{data}} \prod_{j=\text{nottagged}} (1 - \epsilon_j^{\text{data}}) \quad (4.2)$$

$$P(\text{MC}) = \prod_{i=\text{tagged}} \text{SF}_i \epsilon_i^{\text{MC}} \prod_{j=\text{nottagged}} (1 - \text{SF}_j \epsilon_j^{\text{MC}}). \quad (4.3)$$

Here, ϵ denotes the identification efficiency for a b jet in data and simulation respectively, while SF stands for the scale factor for that jet. Both the efficiency and the scale factor depend on the kinematic properties of the jet.

The next chapter will detail the trigger selection used in the $t\bar{t}$ production cross section measurement. It also describes the measurement of the trigger efficiency and the precise determination of its uncertainty.

Chapter 5

Trigger efficiency measurement

In this chapter, the trigger configuration for the $t\bar{t}$ production cross section measurement is described and the trigger efficiency is determined. The trigger efficiency and its uncertainty are important parameters in measuring the $t\bar{t}$ production cross section. In previous analyses, the uncertainty on the trigger efficiency was one of the dominant uncertainties. Similar to other efficiencies described in Chapter 4, the trigger efficiency is measured independently for both data and simulation, and the simulation is rescaled according to the efficiency measured in data.

The trigger selection used in this measurement is described in Section 5.1. The efficiency measurement itself is explained in Section 5.2, together with an alternative method. In order to estimate the precision of the trigger efficiency, another alternative method is applied, as described in Section 5.3. The results from all three methods are compared in Section 5.4. The final set of scale factors between data and simulation used for the subsequent $t\bar{t}$ cross section measurement is described in Section 5.5.

5.1 Trigger selection

The trigger selection aims at reaching maximum efficiency, optimizing the amount of data available for the subsequent $t\bar{t}$ production cross section measurement. Increasing the trigger efficiency also automatically reduces its statistical uncertainty, due to the statistical properties of the binomial distribution. The trigger efficiency itself is measured with respect to the reconstructed and identified leptons (see Chapter 4 for details on this reconstruction). The efficiencies of the trigger and offline selection factorize, i.e., they can be multiplied.

Several triggers, depending on the flavor of the two leptons, are used in this analysis. Dilepton triggers typically have asymmetric p_T requirements for the two leptons, such that the leading lepton has a significantly higher p_T requirement than the subleading lepton.

Using single-lepton triggers for dilepton events has similar consequences. In general, particle properties reconstructed for the trigger are slightly different from the properties of particles used in the offline analysis. This leads to an inefficiency of the trigger compared to the offline selection close to the trigger threshold.

In the case of the dilepton trigger this mainly affects the efficiency at the p_T threshold for the two leptons. One way to mitigate this is to require a higher offline p_T for the leptons than is required by the trigger (see Section 6.2 for the offline selection). Another way to reduce this inefficiency is to combine the dilepton trigger with other triggers which only depend on one lepton, mitigating any inefficiency from the second lepton. Dilepton and single-lepton triggers are combined with a logical 'OR' in the trigger selection.

This combination increases the trigger efficiency by about ten percentage points compared to only using the dilepton trigger, as shown in Figure 5.1. The trigger selection is successfully optimized, since the trigger efficiency is close to 100%

Because of changing conditions during data taking, certain trigger configurations are only available for certain periods of data taking. The triggers chosen here give the most relaxed kinematic requirements possible. This results in the trigger selection depending on the data taking period, as shown in Table 5.1 for each of the three dilepton channels.

Events triggered with certain classes of triggers (such as single-muon or single-electron triggers) are written to separate data sets, leading to a possible overlap when combining these data sets. Double counting of events is prevented by explicitly requiring triggers in their respective data set, but vetoing them in the other data sets.

5.2 Methods using independent triggers

In this analysis, the trigger efficiency is mainly measured using a data set taken with triggers that are independent from the lepton triggers. In general, this allows to measure the trigger efficiency without bias in data and simulation independently. It is important that these independent triggers are as uncorrelated with the lepton triggers as possible. In this Section two methods, with two different sets of independent triggers, are described.

Here, triggers based on the missing transverse energy (E_T^{miss}) are used. They are especially useful for a $t\bar{t}$ analysis, as dileptonic $t\bar{t}$ events are expected to produce E_T^{miss} due to the two neutrinos. Choosing triggers based on E_T^{miss} allows measuring the trigger efficiency for data in an event sample that contains $t\bar{t}$ events. The efficiency in simulation can be measured in a sample of $t\bar{t}$ events. The correlation between the E_T^{miss} and dilepton triggers is studied in simulation and found to be minimal.

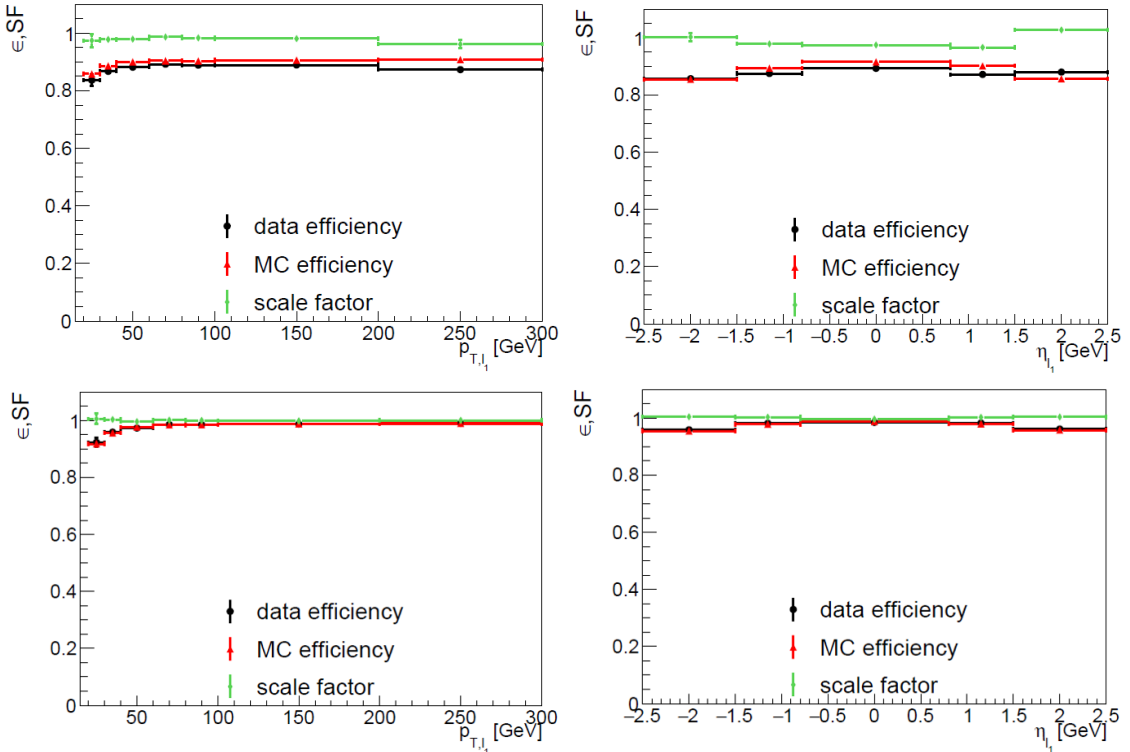


Figure 5.1: Efficiencies of the trigger selection in the $e^\pm\mu^\mp$ channel for simulation and data and the corresponding scale factor. The upper row shows the efficiency when using dilepton triggers only, while the lower row shows the efficiency for a combination of dilepton and single-lepton triggers. The left column shows the efficiency as a function of the p_T of the leading lepton. The right column shows the efficiency as a function of η of the leading lepton. The data used for this comparison corresponds to an integrated luminosity of about 19 fb^{-1} .

Table 5.1: The trigger selection applied on data. It differs between the different run periods because of changing trigger configurations.

Channel	Run	Trigger
$\mu^+\mu^-$	B-G	Mu17_TrkIsoVVL_Mu8_TrkIsoVVL
	B-G	Mu17_TrkIsoVVL_TkMu8_TrkIsoVVL
	H	Mu17_TrkIsoVVL_Mu8_TrkIsoVVL_DZ
	H	Mu17_TrkIsoVVL_TkMu8_TrkIsoVVL_DZ
	B-H	IsoMu24
	B-H	IsoTkMu24
e^+e^-	B-H	Ele23_Ele12_CaloIdL_TrackIdL_IsoVL_DZ
	B-H	Ele27_WPTight_Gsf
$e^\pm\mu^\mp$	B-G	Mu23_TrkIsoVVL_Ele12_CaloIdL_TrackIdL_IsoVL
	B-G	Mu8_TrkIsoVVL_Ele23_CaloIdL_TrackIdL_IsoVL
	H	Mu23_TrkIsoVVL_Ele12_CaloIdL_TrackIdL_IsoVL_DZ
	H	Mu8_TrkIsoVVL_Ele23_CaloIdL_TrackIdL_IsoVL_DZ
	B-H	Ele27_WPTight_Gsf
	B-H	IsoMu24
	B-H	IsoTkMu24

As an alternative, the efficiency of the single-lepton triggers can be measured in an $e^\pm\mu^\mp$ data set. This method is used to determine the systematic uncertainty on the trigger efficiency measurement by comparing these efficiencies to single lepton trigger efficiencies determined with E_T^{miss} triggers.

The trigger efficiency is measured by dividing the amount of events that pass both the offline selection and the dilepton trigger by the number of events that only pass the offline selection. All events have to pass the E_T^{miss} triggers in order to guarantee an unbiased sample. The efficiency is defined as follows:

$$\varepsilon_{\text{trig}} = \frac{N(\text{Offline selection} + E_T^{\text{miss}} \text{ trigger} + \text{dilepton trigger})}{N(\text{offline selection} + E_T^{\text{miss}} \text{ trigger})}, \quad (5.1)$$

where N denotes the number of events that fulfill the given requirements.

The efficiency is measured per event, so the resulting scale factors, to correct simulation to data, are applied per event as well. This is especially useful if a combination of multiple triggers is used in the trigger selection.

The statistical uncertainty is calculated assuming a binomial distribution using the Clopper-Pearson method [94, 95]. It offers at least nominal coverage of the given confidence level and a conservative option to estimate the uncertainty.

Results for efficiencies and scale factors for the e^+e^- , $\mu^+\mu^-$, and $e^\pm\mu^\mp$ channel are shown in Figures 5.2, 5.3, and 5.4, respectively.

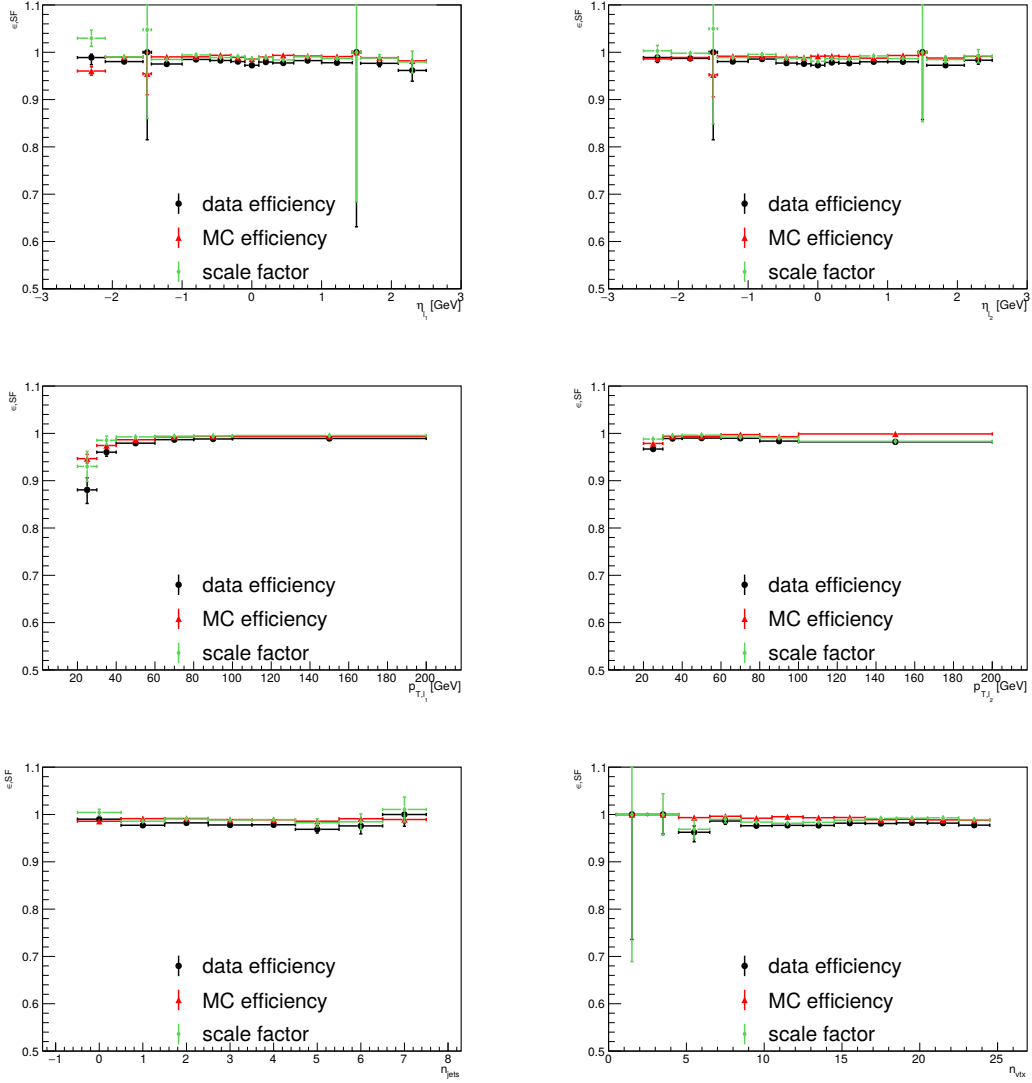


Figure 5.2: Efficiencies of the trigger selection in the e^+e^- channel for simulation and data and the corresponding scale factor. The upper row shows the efficiency as a function of η of the leading (left) and subleading (right) electron. The middle row shows the efficiency as a function of p_T of the leading (left) and subleading (right) electron. The lower row shows the efficiency as a function of the jet multiplicity on the left and the vertex multiplicity on the right. The error bars indicate statistical uncertainties.

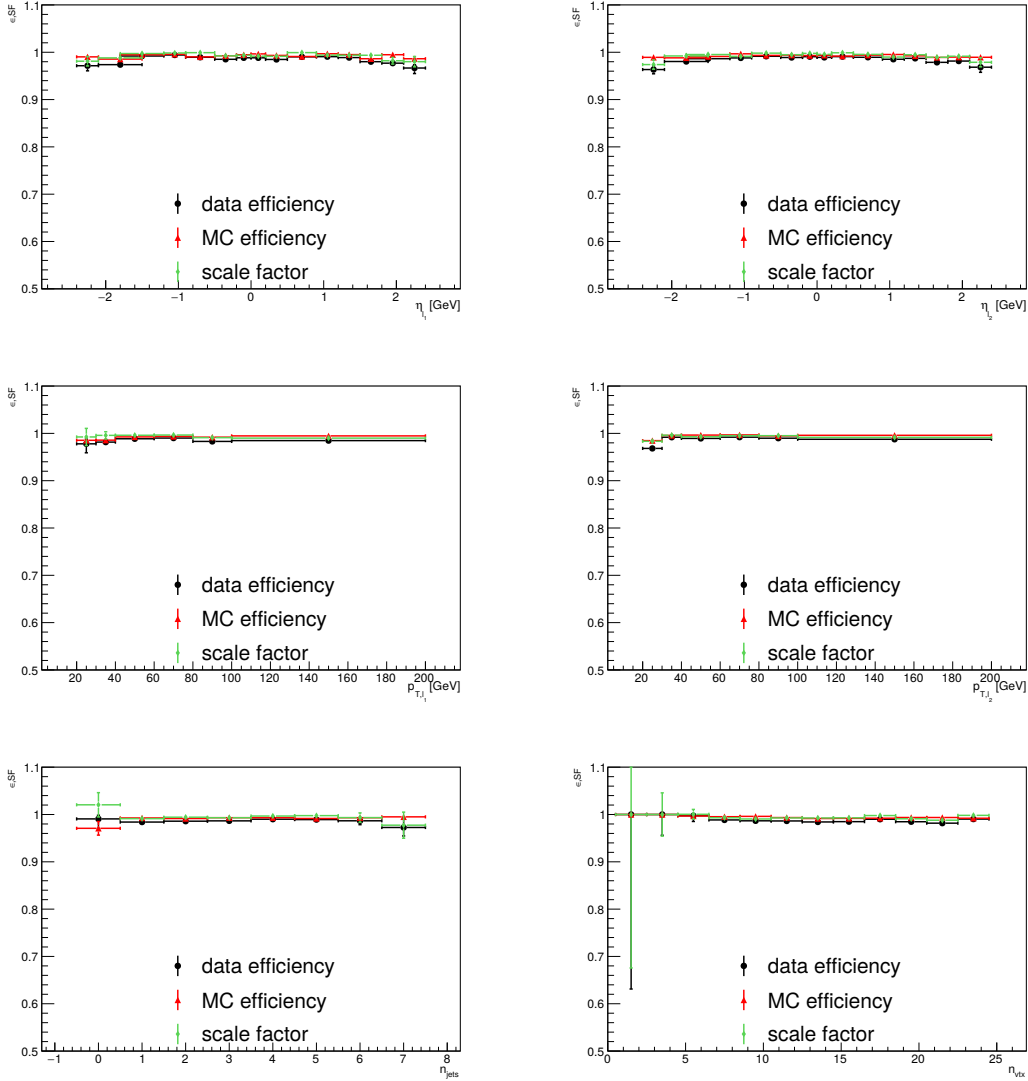


Figure 5.3: Efficiencies of the trigger selection in the $\mu^+\mu^-$ channel for simulation and data and the corresponding scale factor. The upper row shows the efficiency as a function of η of the leading (left) and subleading (right) lepton. The middle row shows the efficiency as a function of p_T of the leading (left) and subleading (right) lepton. The lower row shows the efficiency as a function of the jet multiplicity on the left and the vertex multiplicity on the right. The error bars indicate statistical uncertainties.

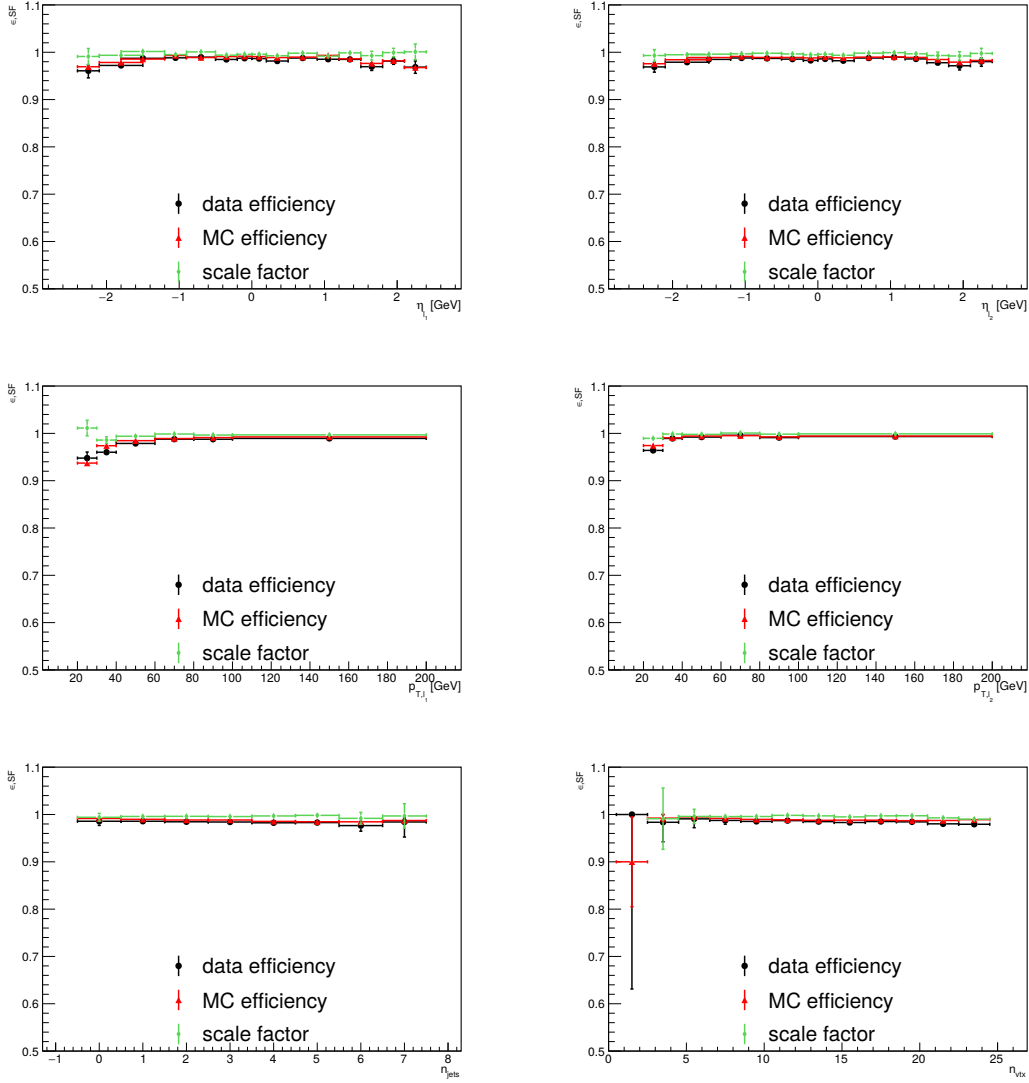


Figure 5.4: Efficiencies of the trigger selection in the $e^\pm \mu^\mp$ channel for simulation and data and the corresponding scale factor. The upper row shows the efficiency as a function of η of the leading (left) and subleading (right) muon. The middle row shows the efficiency as a function of p_T of the leading (left) and subleading (right) muon. The lower row shows the efficiency as a function of the jet multiplicity on the left and the vertex multiplicity on the right. The error bars indicate statistical uncertainties.

The trigger efficiencies are shown as a function of p_T and η of the leading and subleading electrons, the number of jets in the event, and the number of primary vertices. For the e^+e^- channel (see Figure 5.2) the trigger efficiency is close to 100% in most parts of the phase space and the efficiencies in data and simulation agree within uncertainties. The efficiency shows small variations depending on the η of the two electrons. The small bins with a very low number of events around $|\eta| \approx 1.4$ correspond to a region of the detector where the electromagnetic calorimeter is not instrumented. The trigger efficiency shows some dependence on the p_T of the leading electron, especially for $p_T < 30\text{ GeV}$. The single lepton trigger has a requirement of $p_T \geq 27\text{ GeV}$ which contributes to the p_T dependence. The statistical uncertainty in the threshold region is large. The number of $t\bar{t}$ events in that region is comparably low, so that the impact of the decreased efficiency for low p_T (also referred to as the turn-on of the trigger efficiency) is small. There is very little dependence of the trigger efficiency on the p_T of the subleading electron, due to the lower threshold in the dielectron trigger and the addition of the single-electron trigger. The trigger efficiency does not depend on the number of jets, which is especially important for $t\bar{t}$ events, which may contain a large amount of jets. The number of primary vertices is an indication for the number of pile-up collisions in an event. The trigger efficiency does not depend on the number of vertices, which shows that the impact of additional pileup collisions is small.

The trigger efficiency in the $\mu^+\mu^-$ channel is close to 100% and flat for most of the phase space (see Figure 5.3). There are small variations of the efficiency depending on η of the leading and subleading muon. The efficiency also shows a small turn-on effect for the p_T of the subleading muon. Other variations are not statistically significant.

The trigger efficiency in the $e^\pm\mu^\mp$ channel is again very close to 100% and efficiencies in data and simulation agree very well. There is a small drop in the efficiency for high $|\eta|$ for both the leading and the subleading lepton, but the agreement between data and simulation shows that detector effects are well modeled. Similar to the efficiency in the e^+e^- channel the efficiency decreases for $p_T < 30\text{ GeV}$, likely due to the behavior of the electron triggers. The trigger efficiency is flat against the number of jets and primary vertices.

Overall the trigger efficiency is close to 100% for all three channels. The simulation generally agrees with the data, leading to scale factors that are close to unity.

For the $e^\pm\mu^\mp$ data set, the efficiency of the single-lepton triggers can also be measured from data sets selected with a trigger for a single lepton of a different flavor. The electron trigger efficiency can be measured in a data set selected with a single-muon trigger and vice versa. These events closely correspond to the events selected for the $t\bar{t}$ cross section measurement. This method cannot be used for the measurement of dilepton trigger efficiencies, since there are not enough events that contain three leptons. The method can be used to check the

E_T^{miss} based trigger efficiency measurement by comparing the single lepton trigger efficiency obtained with both methods, as shown in Section 5.4.

5.3 Method using tag-and-probe

The tag-and-probe method provides an alternative trigger efficiency measurement that is independent from the measurement described in the last section. In a tag-and-probe measurement, the trigger efficiency is measured independently in data and simulation by using the decay of a Z boson into two leptons.

In general, one of the leptons (the tag) is required to pass a tight selection. This selection includes matching the offline lepton to the lepton reconstructed at trigger level by requiring them to have a minimal distance and difference in p_T . The second lepton (the probe) is only required to pass the lepton selection later used in the $t\bar{t}$ cross section measurement (see Section 6.2). The invariant mass of the two leptons then needs to be within the Z boson mass window, in which case it is assumed that the leptons are real leptons. The probe can either pass the trigger requirement for the trigger that is measured ("passing probe") or fail it ("failing probe"). The efficiency is then determined by dividing the number of passing probes by the number of all probes.

Even in the region of the Z boson mass a background of pairs with at least one fake lepton remains. This residual fake lepton contamination is determined by fitting distributions for real leptons (signal) and fake leptons (background) to the invariant mass of the dilepton system. The fit is done for both passing and failing probes. The background is often described by an exponential function. The signal has a more complicated functional form and can for example be parametrized by a double Voigtian function. The Voigtian function is a convolution of a Lorentz and a Gaussian function. When the trigger efficiency is measured in data it is also possible to fit templates from MC. This can allow a better modeling of detector effects that are included in the simulation. The trigger efficiency in simulation is often measured for a background-free sample (pure Drell-Yan sample). In these cases a fit is not needed and it is sufficient to count the number of passing and failing probes.

The efficiency is measured differentially as a function of kinematic properties of the lepton. The measurement is performed independently in each bin of the distribution. It commonly depends on both the η and the p_T of the lepton.

In contrast to the efficiency measurement using orthogonal triggers (see Section 5.2), the tag-and-probe measurement depends on a specific lepton. It measures the efficiency for each lepton, consequently several measurements have to be combined for a multilepton trigger or an efficiency measurement with multiple triggers (see Section 5.4).

Examples for the efficiency measurement in one bin as well as the overall scale factor for the muon part ("muon leg") of the Mu23_TrkIsoVVL_Ele12_CaloIdL_TrackIdL_IsoVL trigger both for data and simulation and the resulting overall scale factors are shown in Figure 5.5. The fits are successful in modeling the $M_{\ell\ell}$ distribution for passing and failing probes in both data and simulation. The scale factor being close to unity shows that the simulation mostly reproduces the behavior in data.

Figure 5.6 shows the efficiency measurement for the electron part ("electron leg") of the Mu8_TrkIsoVVL_Ele23_CaloIdL_TrackIdL_IsoVL trigger. The fit is performed for passing and failing probes in data, while the efficiency in simulation is measured without a fit by counting the events in the Z boson mass peak. The fits are successful and the efficiency in data and simulation agree within a few percent.

The trigger efficiency for each of the two leptons in the dilepton trigger is combined and compared to the trigger efficiency measured with independent triggers in the next section.

5.4 Comparison of trigger efficiency measurements

In order to assess the systematic uncertainty of the trigger efficiency measurement, the three methods described in Sections 5.2 and 5.3 are compared. The independent trigger method measures the trigger efficiency mostly in $t\bar{t}$ events, while the tag-and-probe method uses Z boson decays. The comparison consequently covers two very different phase spaces and serves as a good estimation of the systematic uncertainty.

The comparison of the independent trigger and the tag-and-probe methods has to contend with one fundamental difference: the independent trigger method using E_T^{miss} triggers measures the trigger efficiency for a complete trigger selection (multiple triggers) and per event, defined by the existence of two isolated leptons fulfilling the kinematic cuts. In contrast, the tag-and-probe method measures the trigger efficiency for each lepton of each trigger separately.

These per-leg efficiencies are combined to the efficiency for each dilepton trigger. This is done by multiplying the efficiencies of the single trigger legs, considering them to be uncorrelated. Next, the efficiencies of each of the lepton triggers (trig_A and trig_B) involved in the trigger selection need to be combined. Since they are combined with a logical OR, this is done by multiplying the inefficiencies of the two triggers:

$$\epsilon(\text{trig}_{\text{combined}}) = 1 - (1 - \epsilon(\text{trig}_A)) \cdot (1 - \epsilon(\text{trig}_B)). \quad (5.2)$$

The combined trigger efficiency measured with the tag-and-probe method can be applied per event for the complete trigger selection. It can then be compared to the trigger efficiency

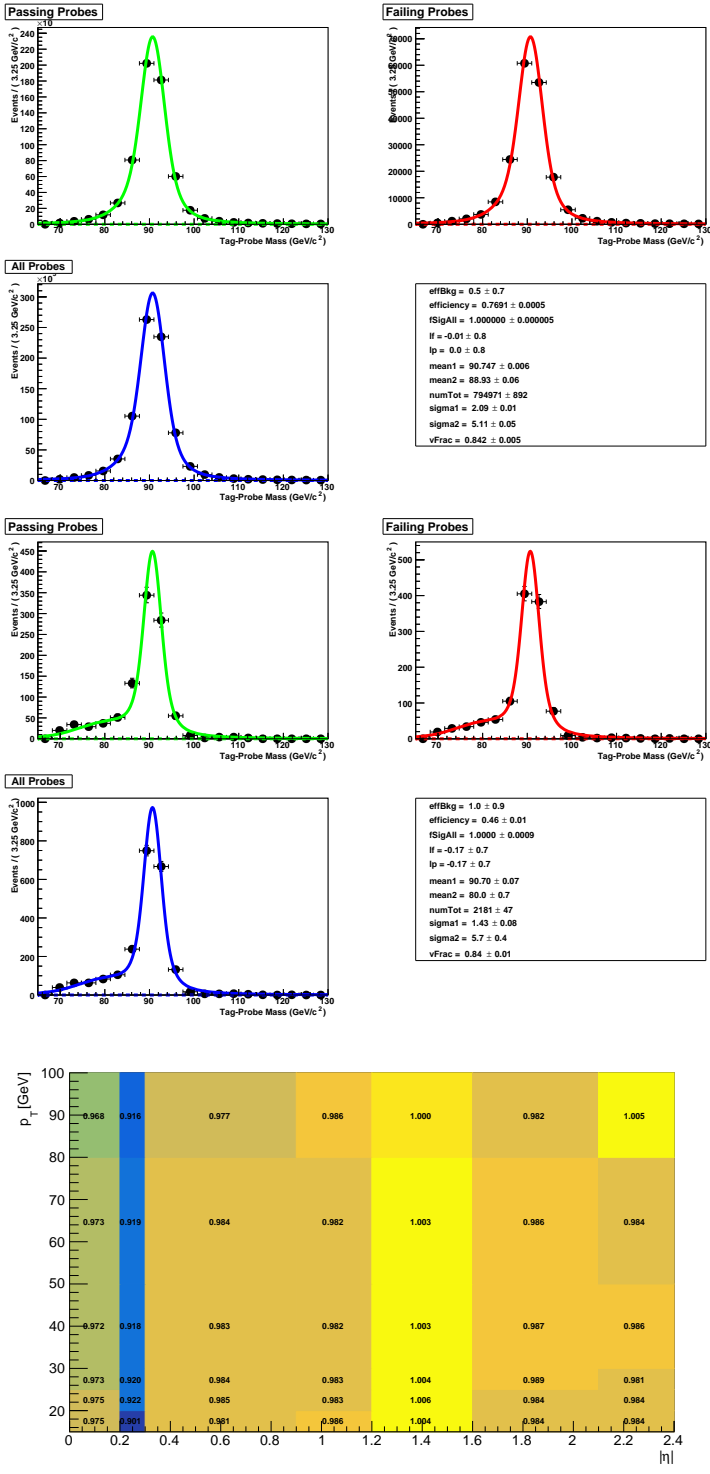


Figure 5.5: Results of the trigger efficiency measurement with the tag-and-probe method for the Mu23 trigger leg. The four upper figures show the measurement for one bin for data while the middle four figures show the same for simulation. The lower figure shows the scale factor between data and simulation binned in η and p_T .

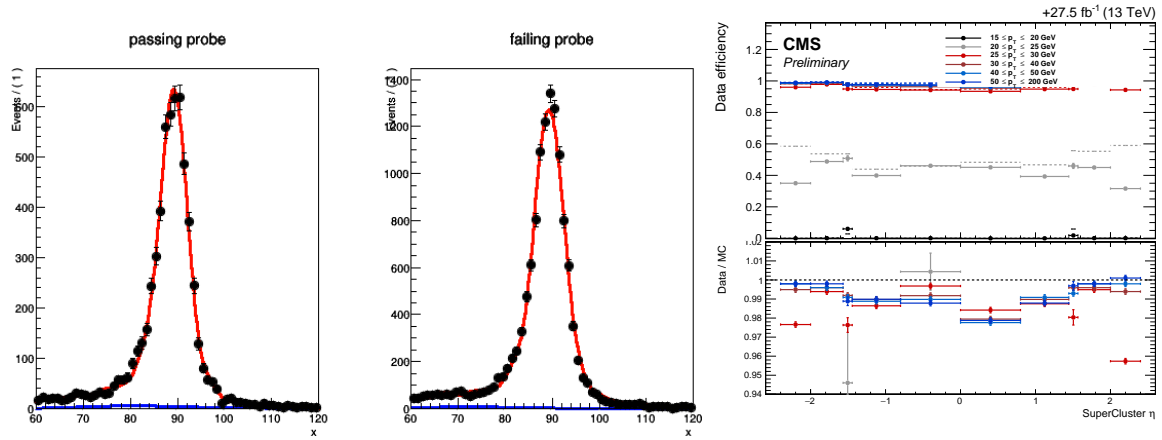


Figure 5.6: Results of the trigger efficiency measurement with the tag-and-probe method for the Ele23 trigger leg. In the left figure the fit for one example bin in data is shown. The right figure shows the efficiency in data and simulation in bins of η with multiple colored graphs showing the p_T dependence. In the lower panel the scale factors are shown in the same format.

measured with the independent E_T^{miss} triggers. For this comparison, both efficiencies are applied to scale the same simulated $t\bar{t}$ sample. These $t\bar{t}$ events are required to contain an electron and a muon (as described for the event selection in Section 6.2) and the trigger efficiency scale factors are applied depending on the η of these leptons. After the rescaling, properties of these two sets of $t\bar{t}$ events are compared as shown in Figure 5.7.

The distributions are consistent with each other in nearly the whole phase space. The largest disagreement is found for events with electrons with $p_T < 20 \text{ GeV}$, but these events are not considered in the final event selection. This agreement shows that there is no systematic difference between the two methods, when measuring a trigger efficiency in the $t\bar{t}$ phase space. This does not necessarily apply to any other possible phase space, but the trigger efficiency measurement here specifically applies to the $t\bar{t}$ phase space. This agreement is considered for the determination of the systematic uncertainties on the trigger efficiency.

Another way to estimate the systematic uncertainty of the independent trigger method is to compare it to a different set of independent triggers, as described in Section 5.2. Since a set of independent triggers that still delivers enough statistics is hard to find for the dilepton triggers, the trigger efficiency of single-lepton triggers is used for the comparison. Beside measuring the single-lepton trigger efficiency in a data set triggered by E_T^{miss} triggers, it is also measured in a data set triggered by opposite lepton flavor triggers. So the electron trigger efficiency is measured in a muon data set and the muon trigger efficiency is measured in an electron data set. The data set triggered by E_T^{miss} triggers is dominated by $W + \text{jets}$

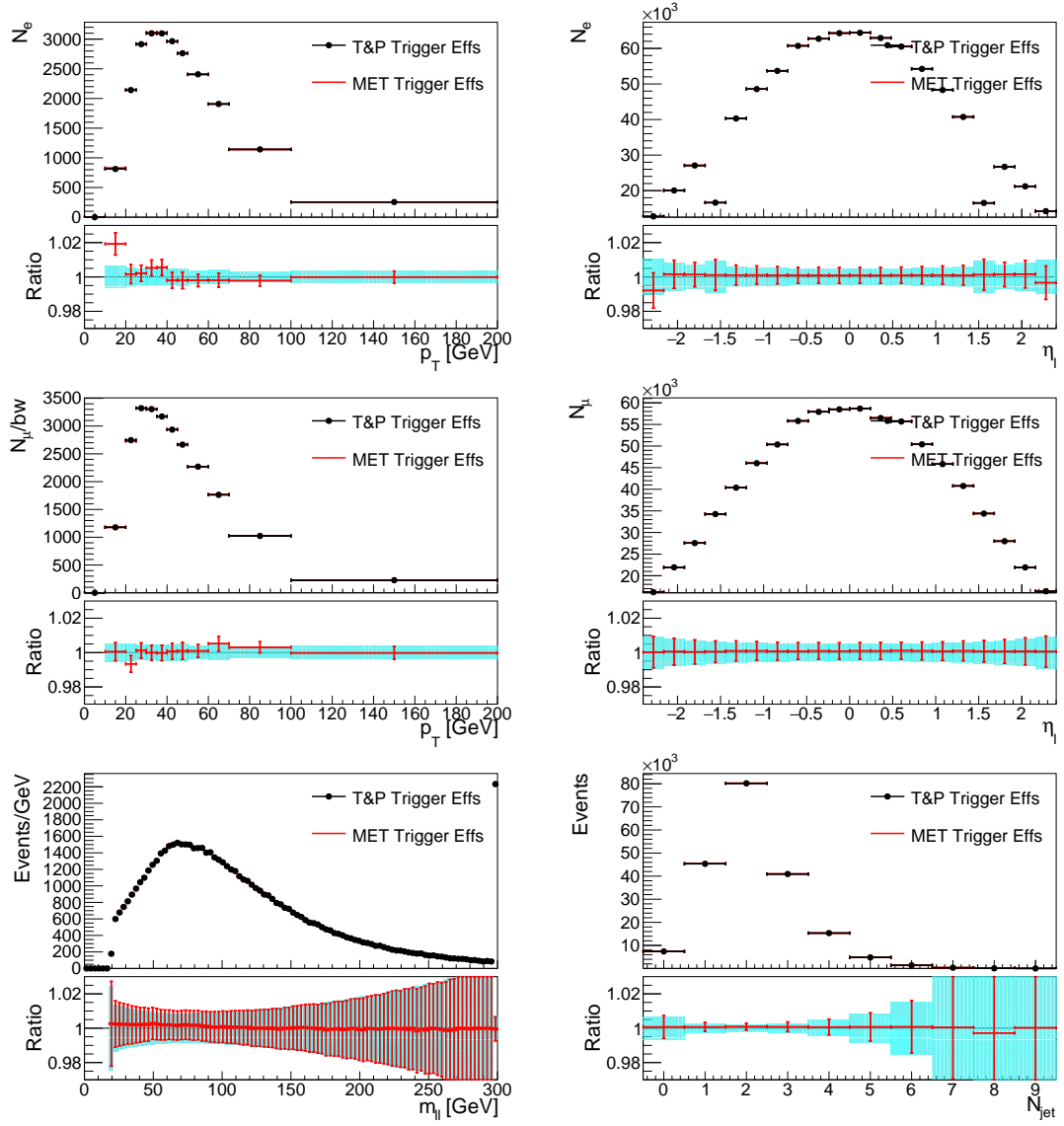


Figure 5.7: Comparison of $t\bar{t}$ simulation reweighted according to the trigger efficiencies measured with the tag-and-probe method and with independent E_T^{miss} triggers. The upper row shows the comparison in bins of p_T (left) and η (right) of the electron. The middle row displays distributions in bins of p_T (left) and η (right) of the muon. The lower row displays distributions in bins of the invariant mass of the dilepton system (left) and the number of jets (right). The uncertainties shown are statistical. The lower panels show the ratio of the distribution reweighted with the efficiency from the E_T^{miss} trigger method divided by the distribution reweighted by the tag-and-probe method.

events, since a lepton and missing transverse energy are required. The data set triggered with single-lepton triggers is dominated by $t\bar{t}$ events, as an electron and a muon are required.

The trigger efficiency for each of the single-lepton triggers is measured as a function η and p_T in data and simulation for both methods. Since the phase space for both efficiency measurements is very different, the trigger efficiencies themselves do not necessarily agree with each other. The scale factor between data and simulation should however agree for both methods.

The comparison is shown in Figure 5.8 for the single-electron and single-muon trigger efficiency. The efficiency is shown as a function of p_T of the leptons in slices of η of the lepton. The η slices are for $|\eta| < 0.9$, $|\eta| < 1.2$, $|\eta| < 2.1$, and $|\eta| < 2.4$. The efficiency for the single-muon trigger is measured in a subset of data, due to problematic conditions for the single-muon trigger in parts of the data.

The scale factors measured for the single-electron trigger with both methods agree in a wide range of the phase space. For $p_T < 20$ GeV the two methods do not agree, but that region is not part of the phase space of the analysis. Similarly, the two methods agree within statistical uncertainties for the full η range.

The scale factors measured for the single-muon trigger also agree for most of the phase space. For $p_T > 100$ GeV the two methods do not give the same scale factor for two regions of $|\eta|$, but this part of the phase space is not very relevant for an inclusive $t\bar{t}$ production cross section measurement. In summary, no significant systematic difference between the methods is observed.

5.5 Determination of the trigger scale factor

The scale factors that correct the trigger efficiency in simulation to the data are determined using the independent trigger method with E_T^{miss} triggers, as described in Section 5.2. It has advantages over the tag-and-probe method: it measures the trigger efficiency directly per event for the complete trigger selection and does not require any additional assumptions on the correlations between the triggers.

Based on the comparison of the two methods (see Section 5.4) and the additional study of the single-lepton triggers, a remaining systematic uncertainty of 0.3% is applied in addition to the statistical uncertainty. Systematic and statistical uncertainty are added in quadrature.

The scale factors are binned in $|\eta|$ of the two leptons, as shown in Figure 5.9. This provides a good compromise between covering disagreements between data and simulation seen in Section 5.2 and sufficient statistical power for each bin.

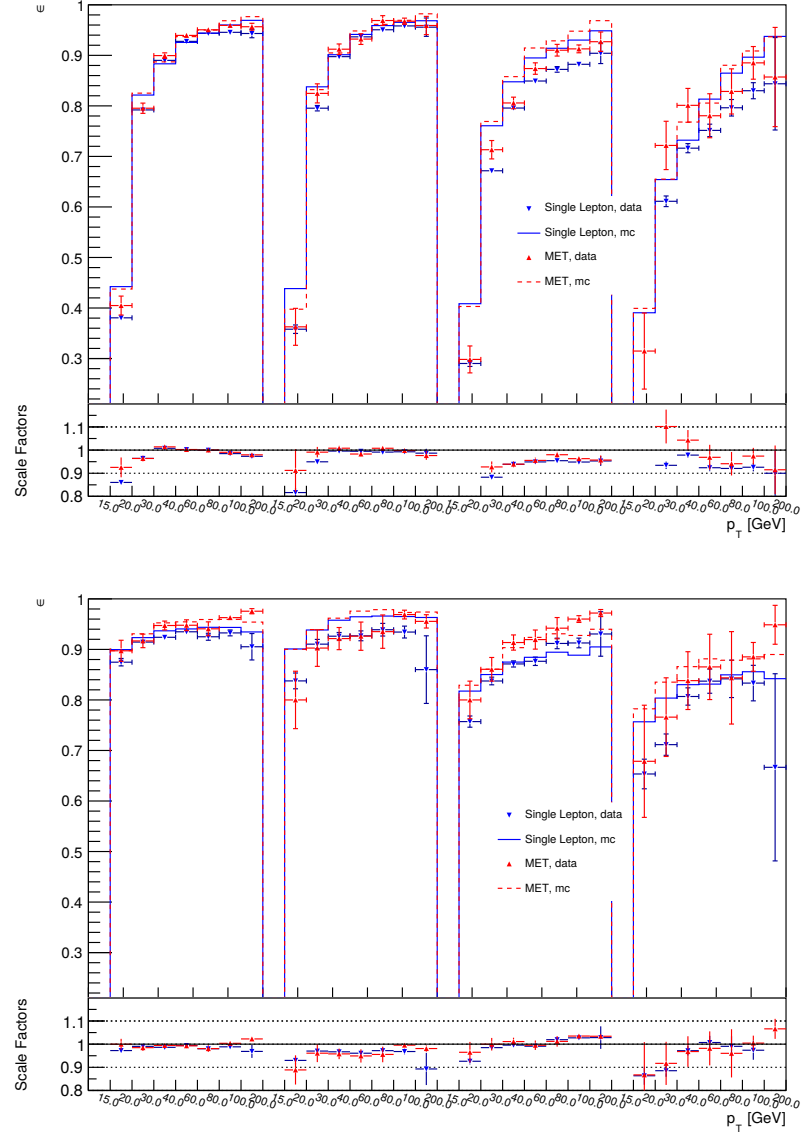


Figure 5.8: Trigger efficiency for the single-electron trigger (upper figure) and single-muon trigger (lower figure) as a function of p_T in slices of η . The efficiency is measured in data and simulation with the independent trigger method. For the single-electron trigger the independent triggers are either single-muon triggers or E_T^{miss} triggers. For the single-muon trigger the independent triggers are either single-electron triggers or E_T^{miss} triggers. The lower panels show the scale factor between data and simulation for both methods. The uncertainties shown are statistical uncertainties.

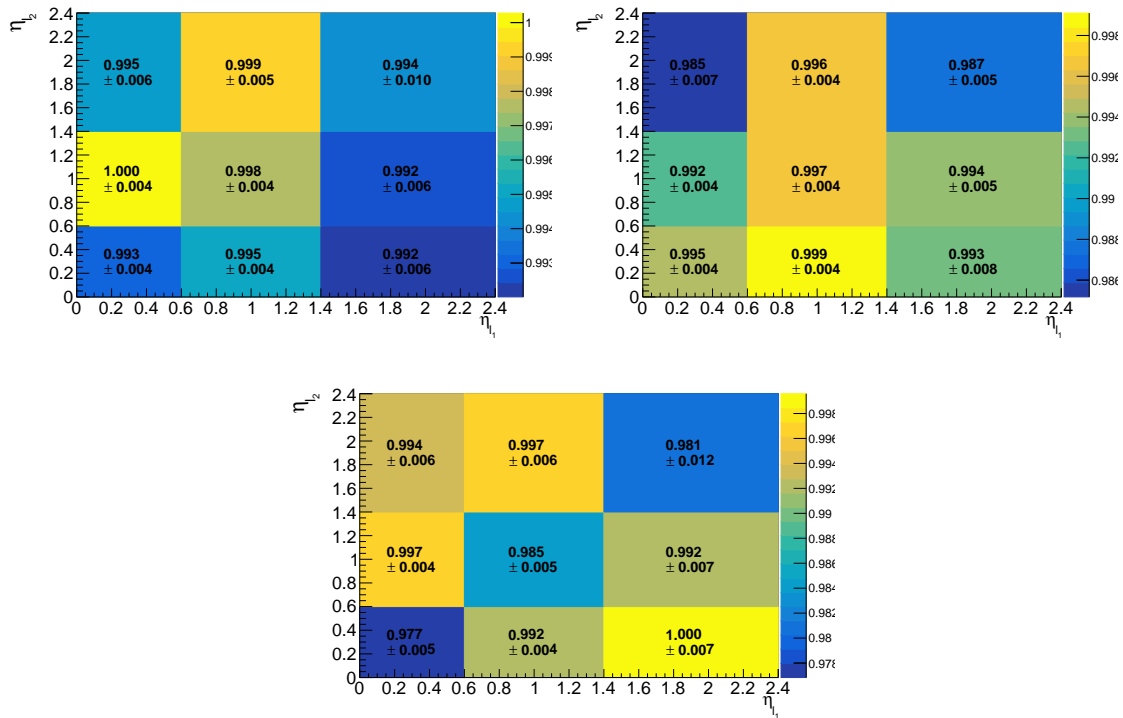


Figure 5.9: Scale factors from the trigger efficiencies of the trigger selection in the $e^\pm\mu^\mp$ (upper left), $\mu^+\mu^-$ (upper right) and e^+e^- (lower middle) channel. The scale factors are given in bins of the $|\eta|$ of the two leptons. The uncertainties denote the combination of statistical and systematic uncertainties.

With the trigger efficiency determination all necessary corrections to simulation are made and the $t\bar{t}$ cross section can be measured. This measurement is described in the following chapter.

Chapter 6

Cross section measurement

This chapter describes the measurement of the $t\bar{t}$ production cross section. A general overview of the analysis strategy is given in Section 6.1. The event selection is described in detail in Section 6.2. The agreement between measured data and simulation is verified for several relevant distributions in Section 6.3. To extract the cross section a template fit is performed, which is described in Section 6.4. A detailed description of the fitting function to be minimized and the parameters involved are given in Section 6.5, including a discussion of the statistics model and the nuisance parameters which account for systematic uncertainties. The description of the extrapolation of the cross section to the full phase space concludes this chapter in Section 6.6.

6.1 Analysis strategy

In general, the cross section in the full phase space can be measured using Equation 6.1. Here, N_{top} denotes the number of selected events containing a top quark pair, A stands for the kinematic acceptance of the selection, ϵ corresponds to the detector efficiency within the visible phase space and \mathcal{L}_{int} is the integrated luminosity.

$$\sigma_{t\bar{t}} = \frac{N_{top}}{A \cdot \epsilon \cdot \mathcal{L}_{int}} \quad (6.1)$$

The integrated luminosity is determined from an independent measurement [96], briefly described in Section 3.1. It is uncorrelated to other aspects of this measurement.

The efficiency ϵ is defined as the ratio of selected $t\bar{t}$ events divided to the number of $t\bar{t}$ events within the visible, or fiducial, phase space, taking into account the event selection. The efficiency is defined as the product of the efficiencies of the reconstruction, identification and kinematic selection of the objects on which the selection is based. The efficiencies for

these specific objects, such as the efficiencies for the reconstruction and identification of two different lepton flavors, are assumed to be uncorrelated. Consequently, the single efficiencies are combined multiplicatively to obtain the total efficiency. It is possible to measure these single object efficiencies independently in data and simulation. In practice, the efficiency is taken from simulation, but only after the simulation has been corrected to describe the efficiency in data. The simulation is corrected by applying event-by-event weighting (see Chapter 4).

The acceptance is defined by a set of kinematic cuts on basic physics objects, which mostly depend on the geometry of the detector and the trigger thresholds described in Section 5.1. The phase space determined by these cuts is also called visible phase space and the acceptance is then given by the ratio of the number of simulated $t\bar{t}$ events within the visible phase space to the total number of simulated $t\bar{t}$ events.

The above definition of the cross section (Equation 6.1) can be modified to only measure the cross section in the visible phase space, as opposed to the larger full phase space. The so called visible cross section $\sigma_{t\bar{t},\text{vis}} = N_{top}/(\varepsilon \mathcal{L}_{\text{int}})$, i.e. A is set to unity, is less dependent on theoretical assumptions as all ingredients can be determined from data. In this analysis the visible cross section is measured and then extrapolated to the full phase space.

The remaining quantity to be determined is the number of $t\bar{t}$ events in the selected data sample. The selected data contain events from signal and numerous background processes. A likelihood fit based on binned observables that distinguish between signal and backgrounds is used to estimate N_{top} . As the simulation used to produce the histogram inputs (templates) depends on systematic variations, nuisance parameters are incorporated to account for these uncertainties.

Due to the large dataset used in this measurement, statistical uncertainties are expected to be negligible with systematic uncertainties limiting the precision. The estimation and minimization of these systematic uncertainties is a key component of this work and is described in detail in Chapter 7. The systematic uncertainties are included as nuisance parameter and fitted simultaneously in the template fit allowing to reduce their impact on the final result and take their full correlation into account.

The precision of the measurement depends on the observables chosen for the templates. Events are also grouped into categories, with each category corresponding to a template. Different observables are chosen for the templates in different categories. Following previous analyses [37], events are split according to the number of b-tagged jets. This enables an in-situ measurement of the b-tagging efficiency using $t\bar{t}$ events (see Section 6.5 for a detailed explanation). The events are also divided according to the final state leptons. The two leptons with the highest p_T define the decay channel ($e^\pm\mu^\mp$, $\mu^+\mu^-$ or e^+e^-). The further division of

the events into the three dilepton channels allows constraining the uncertainties on the lepton efficiencies (see Section 6.4 for a detailed description).

Distributions of the p_T of non b-tagged jets are used as observables for the templates. Beside uncertainties related to the jet reconstruction these distributions are also sensitive to theoretical variations affecting the kinematics of the top quark or the strong coupling.

The main result of the template fit is the $t\bar{t}$ production cross section in the visible phase space. This cross section is then extrapolated to the full phase space using predictions from theory and their respective uncertainties.

6.2 Event selection

As explained above, the aim of the selection is to obtain an event sample that is dominated by signal events. The selection defines the acceptance and, conversely, the visible phase space. The visible phase space should be as large as possible to limit the amount of phase space covered by the extrapolation and to correspondingly reduce additional uncertainties from the extrapolation. In the context of this measurement all systematic uncertainties can be constrained within the visible phase space, therefore it has to correspond to the region of the phase space defined by the selection to avoid over constraining uncertainties.

The $e^\pm\mu^\mp$ decay channel was chosen to measure the $t\bar{t}$ cross section because it already excludes a large amount of background events that affect the same-flavor channels. For example, in the Drell-Yan process, the decay of the photon or Z boson can only produce an $e^\pm\mu^\mp$ final state via intermediate tau lepton decays. The small branching ratio of tau lepton pairs into one electron and one muon results in a relatively small background contribution from the Drell-Yan process in the $e^\pm\mu^\mp$ channel. The contradiction between the aims of a pure sample of signal events and a large visible phase space can be reconciled by exploiting specific topologies of $t\bar{t}$ decays, especially the low background contamination in the $e^\pm\mu^\mp$ decay channel. The same-flavor channels have a large background contribution from the Drell-Yan process that needs to be suppressed. Looser selection requirements can be applied in the $e^\pm\mu^\mp$ channel while still reducing the background contribution in the same-flavor channels with stricter requirements. These additional phase space cuts in the same-flavor channels do not need to be considered for the definition of the visible phase space, based on the assumption that the $t\bar{t}$ signal process shows analogous behavior to the $e^\pm\mu^\mp$ channel. Since the leptons in $t\bar{t}$ events originate from the decay of W bosons and the mass of the leptons themselves is far below the scale of the process, the event kinematics do not depend on the flavor of the leptons. Consequently, the requirements in the $e^\pm\mu^\mp$ channel define the visible phase space (see below for the specific requirements).

First, all events need to fulfill the trigger selection, described in detail in Section 5.1.

Moreover, all events need to contain two isolated and well reconstructed leptons (see Chapter 4). Both leptons should be within the coverage of the tracker fulfilling the condition of $|\eta| < 2.4$. Electrons in the range $1.4442 < |\eta| < 1.566$ are rejected to exclude a region in the calorimeter that is poorly described in simulation. The channel is then defined according to the two leptons requiring the lepton with the leading p_T to have $p_T > 25 \text{ GeV}$ and the subleading lepton to have $p_T > 20 \text{ GeV}$. The events are then categorized into the $\mu^+\mu^-, e^+e^-$ or $\mu^+\mu^-$ channel according to the lepton flavors.

The mass of the dilepton system, $M_{\ell\ell}$, is required to be above 20 GeV to avoid contamination from low-mass DY events. In the same-flavor channels, events within the Z-mass resonance $76 \text{ GeV} < M_{\ell\ell} < 106 \text{ GeV}$ are vetoed to reduce the dominant background of resonant Drell-Yan production.

Jets are required to have $p_T > 30 \text{ GeV}$ and $|\eta| < 2.4$. In order to identify b jets correctly, a tight working point is chosen that minimizes the amount of jets wrongly misidentified as b jets (see Section 4.5).

In the same-flavor channels events are required to contain at least one b-tagged jet, while events in the $e^\pm\mu^\mp$ channel are not required to include any jets.

The visible phase space is defined as follows: The leading lepton in p_T is required to have $p_T > 25 \text{ GeV}$ and the trailing lepton is required to have $p_T > 20 \text{ GeV}$ while the dilepton system fulfills $M_{\ell\ell} > 20 \text{ GeV}$. The definition applies to particles in simulation: The leptons have to be final state particles after the simulation of the parton shower, after all final state radiation, but before the detector simulation.

The selection results in an acceptance of 3% (including $t\bar{t}$ decay branching ratio) and an efficiency of 37%.

6.3 Comparison of simulation and data

Distributions for events passing the event selection are shown in the following for all three decay channels. The systematic uncertainties affecting the respective observables are shown in the ratio of data and simulation shown in the lower panels of the figures. The uncertainties include all systematic uncertainties except for the uncertainties on the luminosity and the normalization of the background processes. The figures show that the simulation can reproduce the behavior of the data very well.

The p_T for the leading and subleading lepton for all three decay channels is shown in Figure 6.1. Signal events have the largest contribution in all three channels. The background contribution in the same-flavor channels is smaller than in the $e^\pm\mu^\mp$ channel. For $t\bar{t}$ events the

p_T of the leading lepton peaks around 40 GeV, which is especially visible for events in the same-flavor channel. The p_T of the subleading lepton follows a falling distribution for all processes. Both the subleading and the leading lepton tend to have higher p_T in $t\bar{t}$ compared to the backgrounds. Overall, the simulation mostly agrees with the data, whereas the same-flavor channels have a somewhat larger statistical uncertainty for both data and simulation, especially in the e^+e^- channel. This is expected, since the $e^\pm\mu^\mp$ channel has a higher branching ratio for $t\bar{t}$ decays. In the high p_T region the data tends to have a softer p_T compared to the simulation for both the leading and the subleading lepton. The disagreement can be explained by the failure of the simulations to model the top p_T spectrum in $t\bar{t}$ events [97, 98]. A dedicated systematic uncertainty is introduced (described in Section 7.2), which accounts for this effect.

The η distribution for the leading and subleading lepton for all three decay channels is shown in Figure 6.2. For electrons ($e^\pm\mu^\mp$ and e^+e^- channel) the η distribution shows a gap around $|\eta| \approx 1.5$. This reduction in the number of events is caused by an instrumentation gap in the ECAL (see Section 6.2). Otherwise, the η distribution is smooth as seen for the $\mu^+\mu^-$ channel. The simulation generally agrees with the data within uncertainties. The systematic uncertainties are generally higher for larger η values, as uncertainties on the lepton reconstruction tend to increase if the lepton is detected in the endcaps of the detector.

The number of jets for all three channels is shown in Figure 6.3. The largest number of $t\bar{t}$ events is found in the bin with exactly two jets. Events with zero jets are rejected for the e^+e^- and $\mu^+\mu^-$ channel, but the $e^\pm\mu^\mp$ channel shows that the signal contribution in that region of phase space is comparatively small. As seen in all channels, $t\bar{t}$ signal events tend to contain more jets compared to background events, as two jets come from the top quark decays and gluons can be radiated from both the initial state and the final state. In Drell-Yan events with two leptons, radiation of additional gluons is only possible for the initial state quarks.

The simulation and the data do not agree for a high number of jets in the $e^\pm\mu^\mp$ and $\mu^+\mu^-$ channels. In the specific simulation used here (see Section 2.4) up to three jets are simulated in the hard process, while any other jets are produced in the parton shower. The more extreme ranges of the phase space, such as events with more than five additional jets, are not well modeled. This is a well-known issue in the simulation of $t\bar{t}$ events and as shown in the figures it is well covered by the systematic uncertainties. Especially the systematic variations for the parton shower parameters chosen for the simulation (see Section 7.2) contribute in this region of phase space. In the e^+e^- channel the statistical uncertainty on both the data and the simulation is too large to draw decisive conclusions.

The number of b-tagged jets for all three channels is shown in Figure 6.4. Events with zero b-tagged jets are rejected for the same-flavor channels. A significant amount of $t\bar{t}$ signal

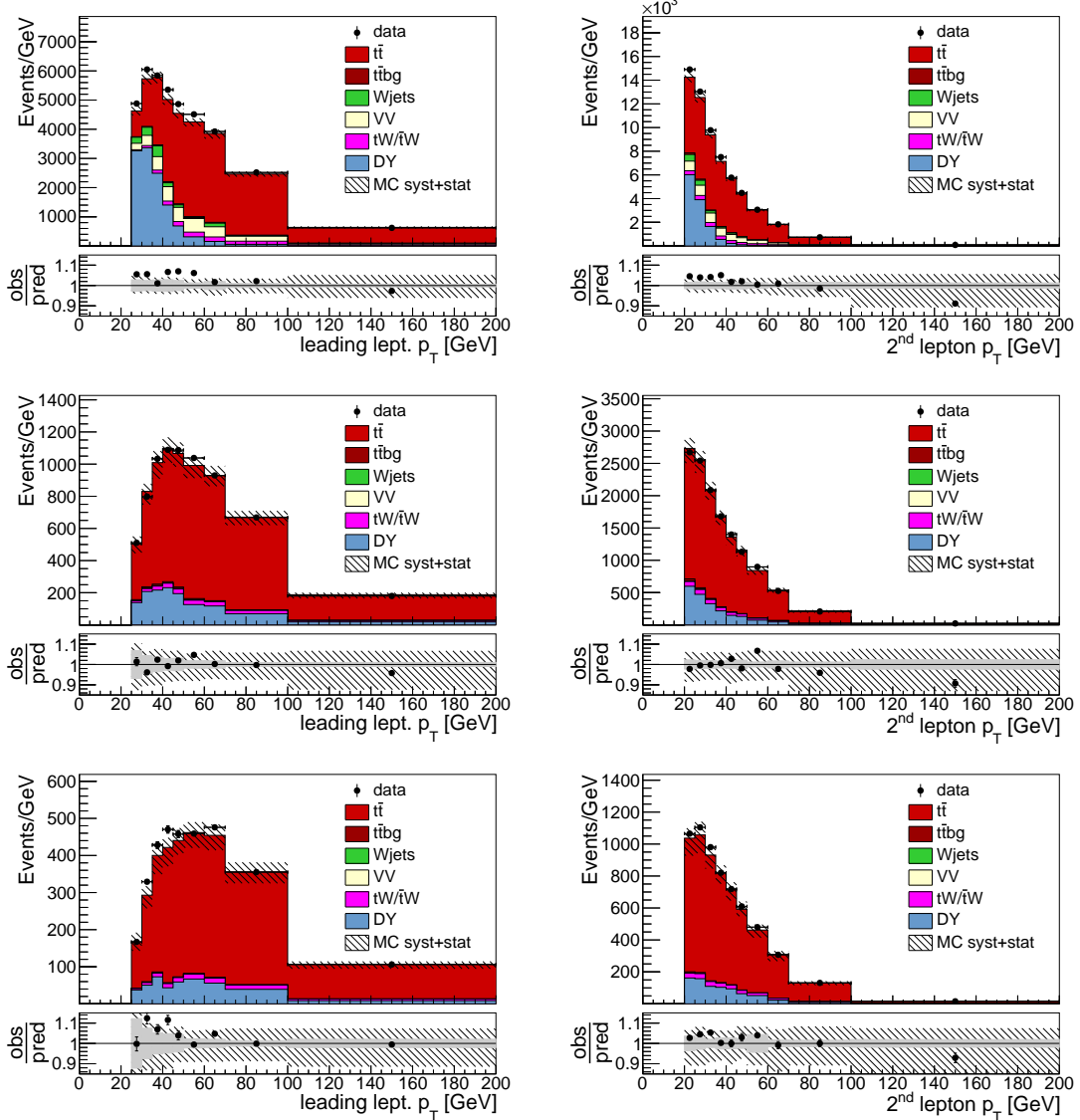


Figure 6.1: Transverse momentum of the leading (left) and subleading (right) lepton in the $e^\pm \mu^\mp$ (upper row), $\mu^+ \mu^-$ (middle row) and $e^+ e^-$ (lower row) decay channels. The events are shown after the event selection. The hatched bands correspond to the total uncertainty on the sum of the predicted yields , excluding luminosity and background normalization uncertainties. The ratios of data to the sum of the predicted yields are shown at the bottom panel of each figure. The solid gray band represents the contribution of the statistical uncertainty.

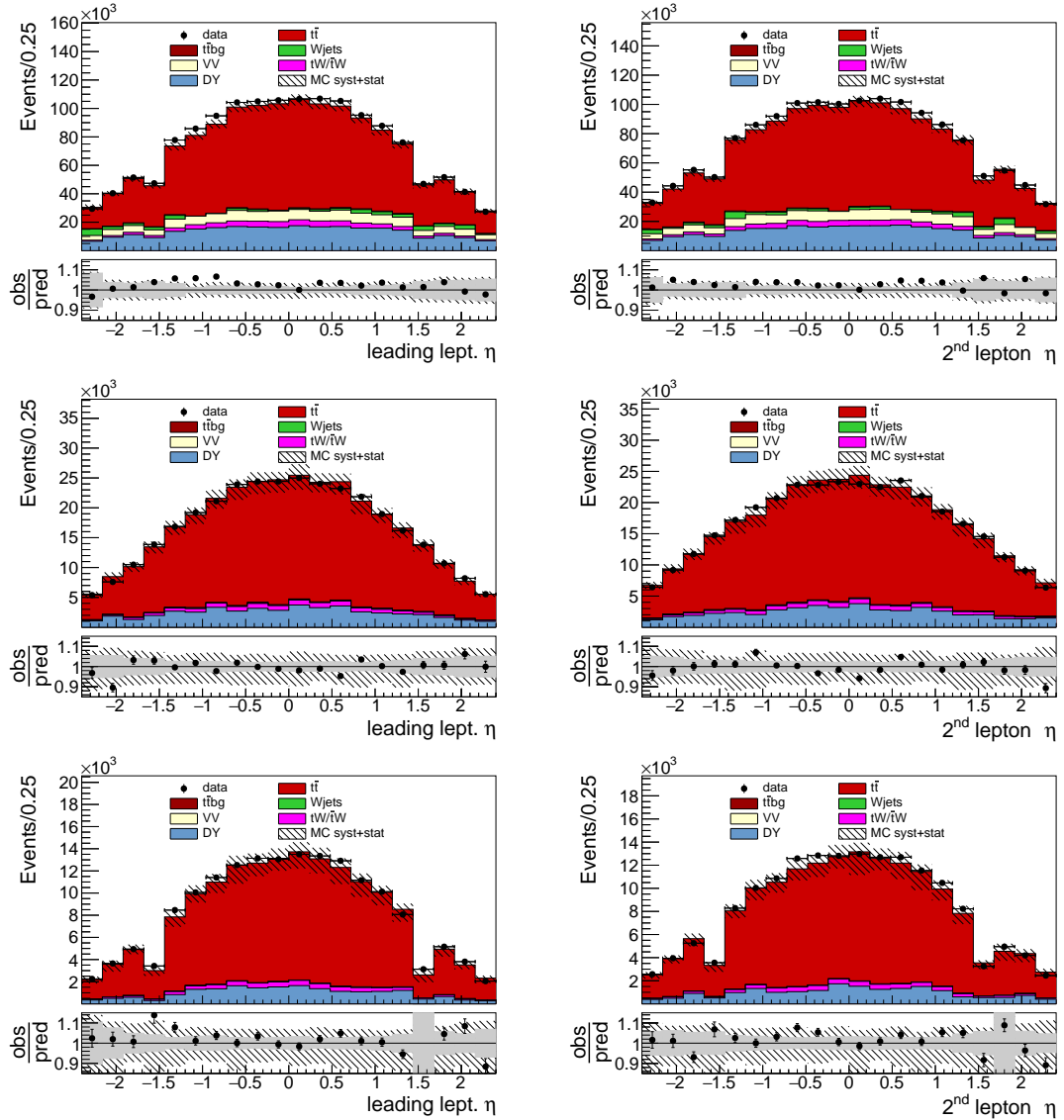


Figure 6.2: Pseudo rapidity for the leading (left) and subleading (right) lepton in the $e^\pm\mu^\mp$ (upper row), $\mu^+\mu^-$ (middle row) and e^+e^- (lower row) decay channels. The events are shown after the event selection. The hatched bands correspond to the total uncertainty on the sum of the predicted yields, excluding luminosity and background normalization uncertainties. The ratios of data to the sum of the predicted yields are shown in the bottom panel of each figure. The solid gray band represents the contribution of the statistical uncertainty.

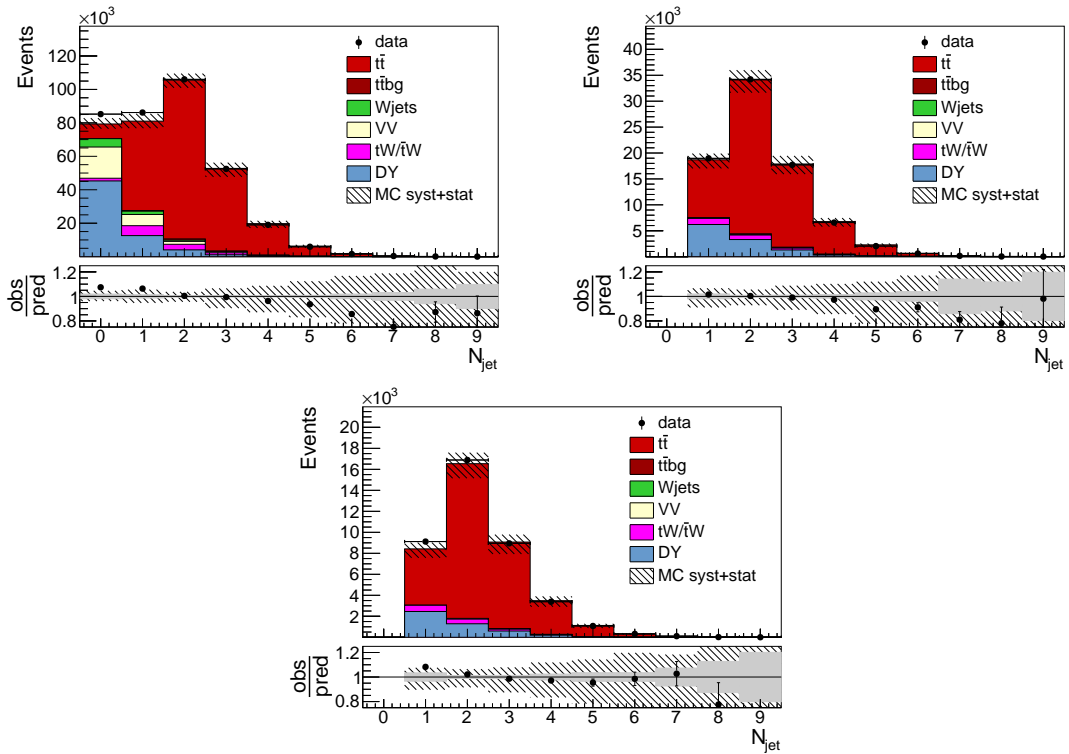


Figure 6.3: Number of jets $e^\pm\mu^\mp$ (upper left), $\mu^+\mu^-$ (upper right) and e^+e^- (lower row) decay channels. The events are shown after the event selection. The hatched bands correspond to the total uncertainty on the sum of the predicted yields, excluding luminosity and background normalization uncertainties. The ratios of data to the sum of the predicted yields are shown in the bottom panel of each figure. The solid gray band represents the contribution of the statistical uncertainty.

events contain zero b-tagged jets, due to the comparably low efficiency to identify a jet containing a b quark. However, the small amount of background events containing one or more b-tagged jet indicates the low probability to wrongly identify a jet as b-tagged. The main remaining background contribution with one or more b-tagged jet in the $e^\pm\mu^\mp$ channel are events which contain a b quark from the top-quark decay. In the same-flavor channel Drell-Yan events contribute significantly as well. The behavior of the data is well modeled by the simulation in all three channels.

As shown in the figures, variables relating to (b-tagged) jets provide discrimination between signal and background. Hence these variables are used to further separate signal and background

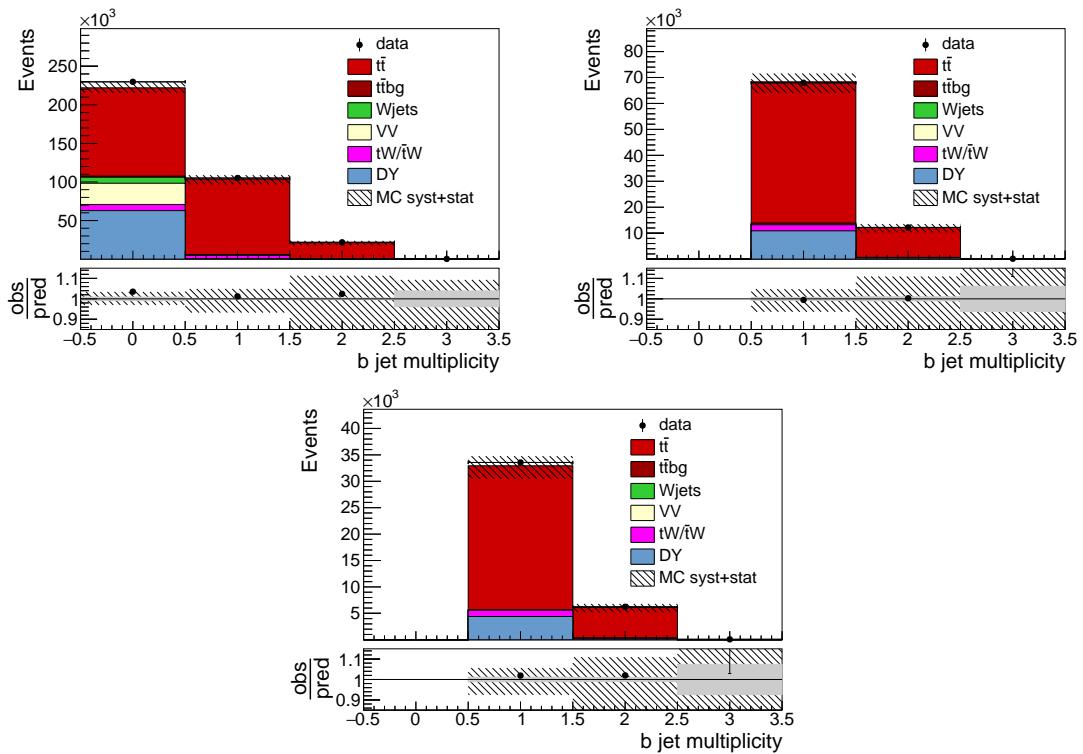


Figure 6.4: Number of b-tagged jets $e^\pm\mu^\mp$ (upper left), $\mu^+\mu^-$ (upper right) and e^+e^- (lower row) decay channels. The events are shown after the event selection. The hatched bands correspond to the total uncertainty on the sum of the predicted yields, excluding luminosity and background normalization uncertainties. The ratios of data to the sum of the predicted yields are shown in the bottom panel of each figure. The solid gray band represents the contribution of the statistical uncertainty.

The invariant mass of the dilepton system is shown in Figure 6.5 for the $e^\pm\mu^\mp$ channel and depending on the number of b-tagged jets (for zero, one and two or more b-tagged jets). The

distribution for signal events has a broad maximum in the region of 60 – 100 GeV with long tails up to 300 GeV. Drell-Yan events show the expected peak at the mass of the Z boson.

In most distributions the data are well modeled by the simulation. In regions where the modeling is poor, the discrepancies are accounted for with systematic uncertainties.

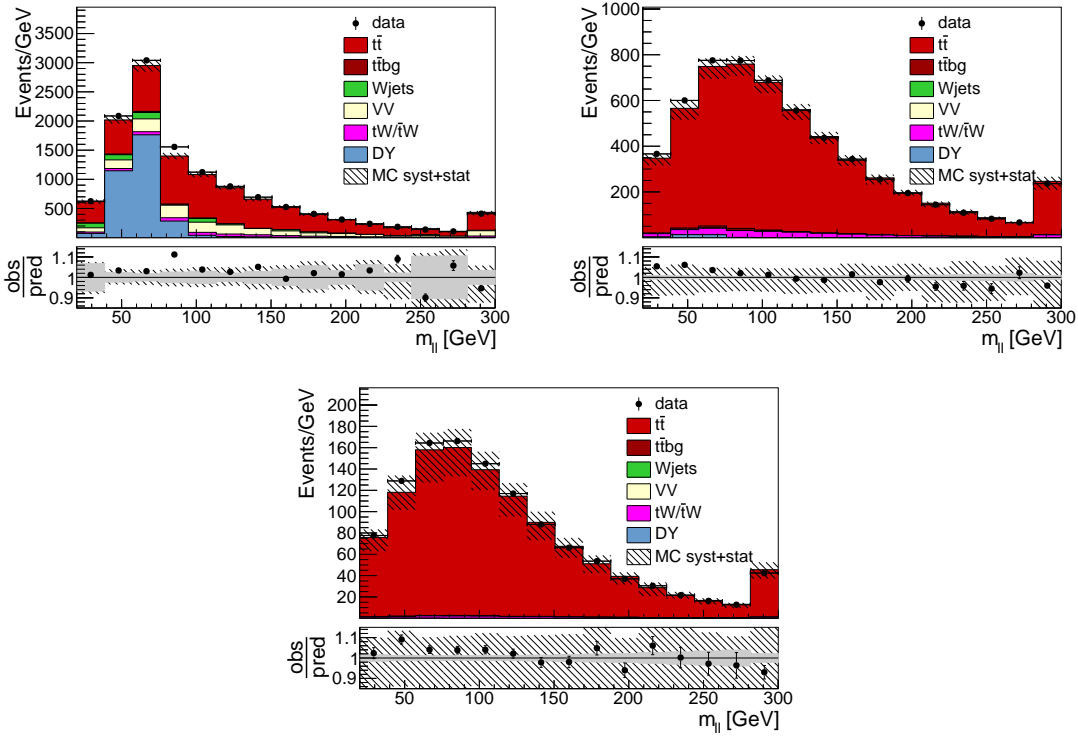


Figure 6.5: Invariant mass of the dilepton system with zero (upper left), one (upper right) and two (lower row) b-tagged jets in the $e^\pm\mu^\mp$ channel. The hatched bands correspond to the total uncertainty on the sum of the predicted yields, excluding luminosity and background normalization uncertainties. The ratios of data to the sum of the predicted yields are shown in the bottom panel of each figure. The solid gray band represents the contribution of the statistical uncertainty.

6.4 Choice of event categories and template distributions

The events are categorized by lepton flavor, number of b-tagged jets and number of non b-tagged jets. This leads to 28 different categories. In each category a template distribution is used to constrain the uncertainties. An overview is given in Table 6.1.

In order to maximize the separation between signal and background the events are divided according to the number of b-tagged jets. There are three categories of events corresponding

Table 6.1: Table of the template distributions chosen for the fit. They are listed for each of the three decay channels and are further split according to the number of b-tagged jets and additional non b-tagged jets.

Number of b jets	Number of add. jets	Decay channel		
		$e^\pm\mu^\mp$ channel	$\mu^+\mu^-$ channel	e^+e^- channel
0 or ≥ 3 b jets	0 add. jets	event yield	-	-
	1 add. jets	p_T (1st jet)	-	-
	2 add. jets	p_T (2nd jet)	-	-
	≥ 3 add. jets	p_T (trail. jet)	-	-
1 b jet	0 add. jets	event yield	event yield	event yield
	1 add. jets	p_T (1st jet)	event yield	event yield
	2 add. jets	p_T (2nd jet)	event yield	event yield
	≥ 3 add. jets	p_T (trail. jet)	event yield	event yield
2 b jets	0 add. jets	event yield	event yield	event yield
	1 add. jets	p_T (1st jet)	p_T (1st jet)	p_T (1st jet)
	2 add. jets	p_T (2nd jet)	p_T (2nd jet)	p_T (2nd jet)
	≥ 3 add. jets	event yield	event yield	event yield

to $N_{b-jet} = 1$, $N_{b-jet} = 2$ or $N_{b-jet} = 0$ and $N_{b-jet} \geq 3$. This categorization also allows determining the efficiency to find a b-tagged jet in a signal event using the topology of $t\bar{t}$ decays. Since each of the top quarks decays into a W boson and a b quark, every $t\bar{t}$ event should contain two jets originating from b quarks. Decays of a top quark to a W boson and a light quark are considered negligible. Therefore, the number of $t\bar{t}$ events with less than two b-tagged jets can be used to measure the efficiency to select a b-tagged jet.

In this way, the b-tagging efficiency is determined independently for data and simulation (see Section 6.5). The efficiency of the b-tagging algorithm is independent of the lepton flavor and is assumed to be the same for all $t\bar{t}$ decay channels. The in-situ measurement of the b-tagging efficiency in the phase space of the $t\bar{t}$ cross section measurement reduces the impact of the uncertainty on the b-tagging efficiency. The b-tagging efficiency can also be measured in an independent measurement, but measuring it in-situ is preferable to avoid extrapolation to a different phase space.

Besides the number of b-tagged jets, the number of light (non b-tagged) jets is one of the main discriminators between $t\bar{t}$ and background events. Events containing a top quark pair tend to have a larger amount of additional jets from final state radiation. Events are split according to the number of light jets for one, two and zero or more than two jets. In each event the p_T of the trailing light jet is chosen as template distribution. Together with the p_T of the light jets, their multiplicity is sensitive to the systematic uncertainty on the response of

the jet reconstruction and the systematic uncertainties introduced by theoretical assumptions in the simulation.

The separation of events into the $e^\pm\mu^\mp$, $\mu^+\mu^-$ and e^+e^- channels is explained in Section 6.2. The $t\bar{t}$ cross section is assumed to be constant in all three decay channels. Any difference in branching ratio can be assumed to be described correctly in simulation. By simultaneously fitting the three channels with the two uncorrelated lepton identification efficiencies ϵ_e and ϵ_μ the nuisance parameters related to the two efficiencies are correlated. The relation between the number of $t\bar{t}$ events in each dilepton channel ($s_{e^\pm\mu^\mp}$, s_{ee} and $s_{\mu\mu}$), the ttbar cross section ($\sigma_{t\bar{t}}$) and the lepton efficiencies is shown in simplified form in Equation 6.4.

$$s_{e\mu} \propto \sigma_{t\bar{t}} \epsilon_e \epsilon_\mu \quad (6.2)$$

$$s_{ee} \propto \sigma_{t\bar{t}} \epsilon_e^2 \quad (6.3)$$

$$s_{\mu\mu} \propto \sigma_{t\bar{t}} \epsilon_\mu^2. \quad (6.4)$$

These relations can be rewritten as:

$$\frac{s_{\mu\mu}}{s_{ee}} \propto \frac{\epsilon_\mu^2}{\epsilon_e^2} \quad \frac{s_{\mu\mu}}{s_{e\mu}} \propto \frac{\epsilon_\mu}{\epsilon_e} \quad (6.5)$$

By measuring $s_{\mu\mu}$ and s_{ee} the efficiencies are constrained. Since the uncertainties on the lepton efficiencies are uncorrelated before the fit, the constraints of the efficiency ratio suppress the larger of the two lepton efficiency uncertainties. Here, prior to the fit, the muon identification uncertainty is smaller, and thus in the fit the single-electron identification uncertainty is constrained to that of the muon.

The final 28 templates are listed in Table 6.1 and shown in Figures 6.6, 6.7 and 6.8 for the $e^\pm\mu^\mp$, $\mu^+\mu^-$ and e^+e^- channel respectively.

6.5 Definition of the likelihood

A binned likelihood fit is used to extract the $t\bar{t}$ cross section using the event categorization described above. The number of expected events for signal and background is fitted to the number of measured events. The likelihood function used for the fit is based on poisson statistics:

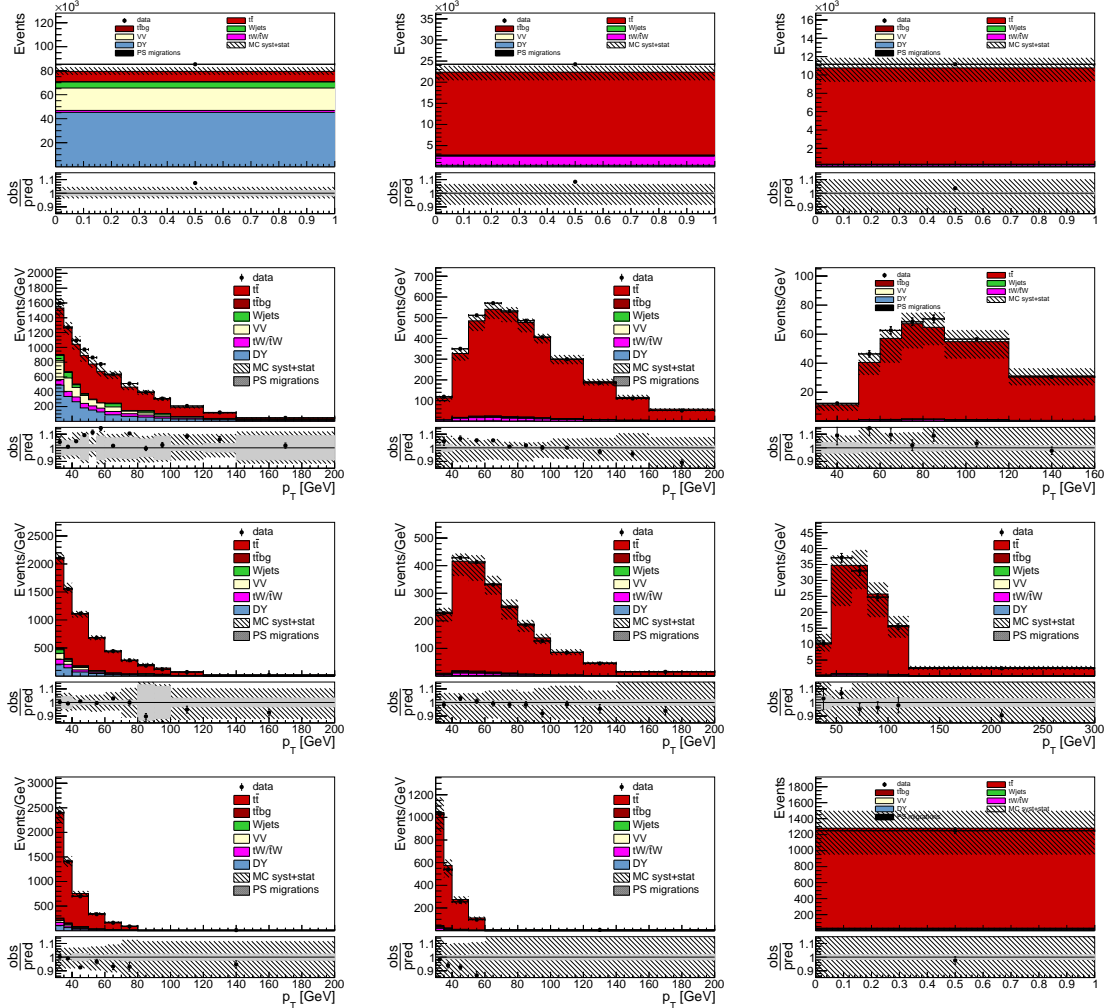


Figure 6.6: Template distributions for events in the $e^\pm\mu^\mp$ channel with zero as well as three or more b-tagged jets (left column), one b-tagged jet (middle column), or two b-tagged jets (right column). The distributions show the total event yield for zero jets (top), the p_T of the jet with the lowest p_T for one (second from top), two (second from bottom) or three or more (bottom) additional jets. The hatched bands correspond to the total uncertainty on the predicted number of events, excluding luminosity and background normalization uncertainties. The ratios of the event yields in data and the sum of the predicted yields are shown at the bottom of each figure. Here, the solid gray band represents the contribution of the statistical uncertainty.

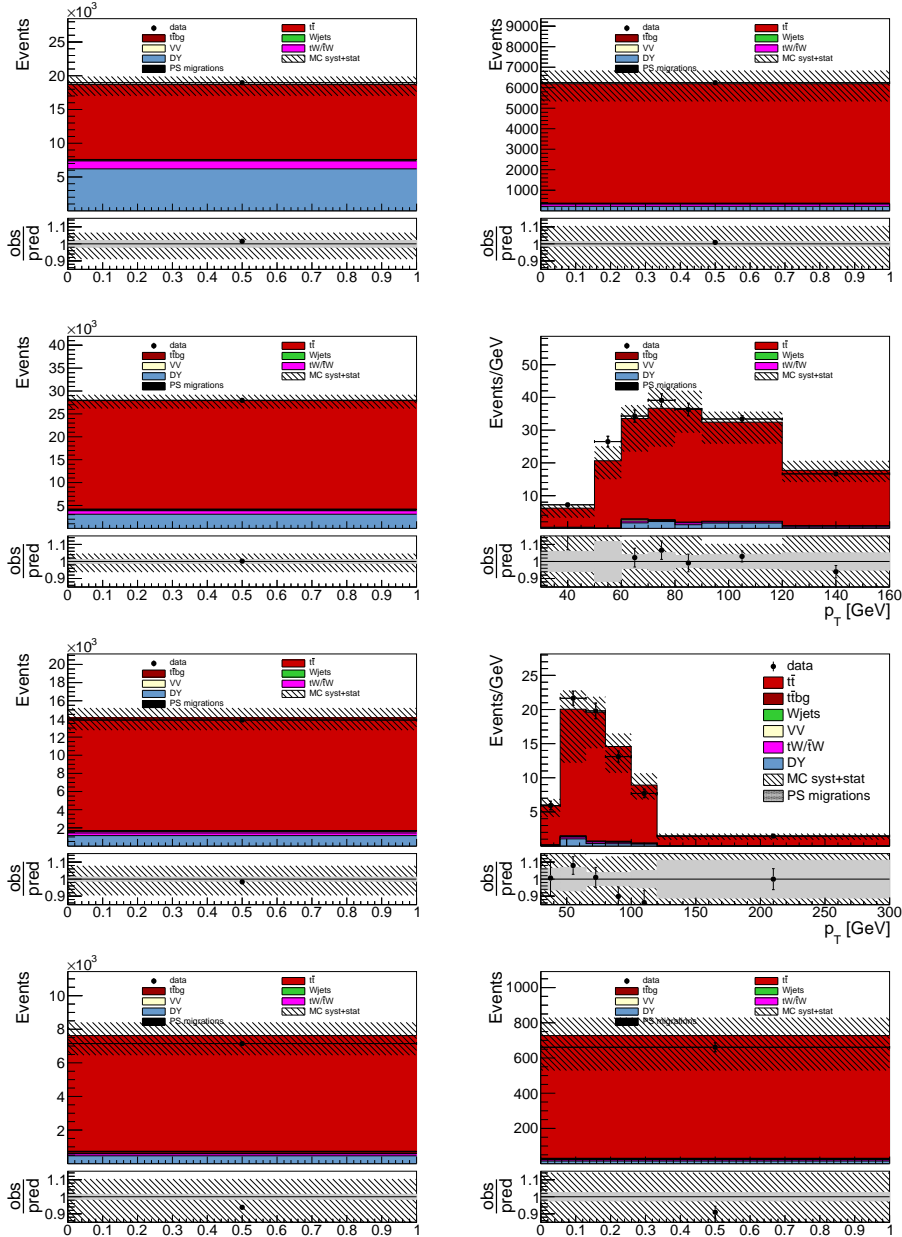


Figure 6.7: Template distributions for events in the $\mu^+\mu^-$ channel with one b-tagged jet (left column) or two b-tagged jets (right column). The distributions show the total event yield for zero (top), the p_T of the jet with the lowest p_T for one (second from top), two (second from bottom) or three or more (bottom) additional jets. The hatched bands correspond to the total uncertainty on the predicted number of events, excluding luminosity and background normalization uncertainties. The ratios of the event yields in data and the sum of the predicted yields are shown at the bottom of each plot. Here, the solid gray band represents the contribution of the statistical uncertainty.

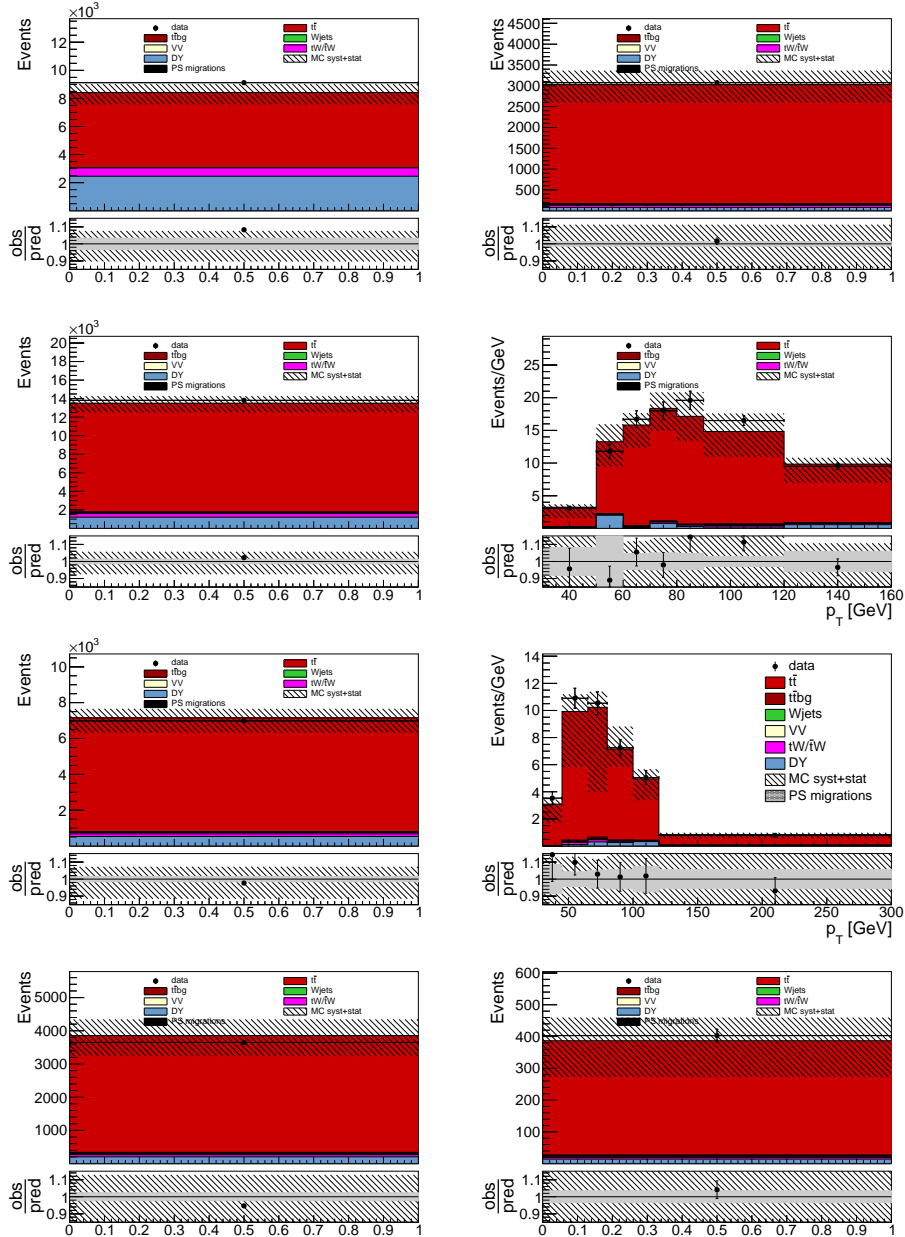


Figure 6.8: Template distributions for events in the e^+e^- channel with one b-tagged jet (left column) or two b-tagged jets (right column). The distributions show the total event yield for zero (top), p_T of the jet with the lowest p_T for one (second from top), two (second from bottom) or three or more (bottom) additional jets. The hatched bands correspond to the total uncertainty on the predicted number of events, excluding luminosity and background normalization uncertainties. The ratios of the event yields in data and the sum of the predicted yields are shown at the bottom of each figure. Here, the solid gray band represents the contribution of the statistical uncertainty.

$$\mathcal{L} = \prod_i \frac{\exp(\mu_i) \mu_i^{n_i}}{n_i!} + \prod_l \pi(\omega_l) + \prod_m \pi(\lambda_m) \quad (6.6)$$

$$\text{where } \mu_i = s_i(\sigma_{t\bar{t},\text{vis}}, \vec{\lambda}) + \sum_l b_{l,i}(\omega_l, \vec{\lambda}). \quad (6.7)$$

Here the index i represents a single bin, while n_i is the number of measured events in data. The symbol μ_i represents the number of expected events in simulation. The terms ω_l and λ_m denote the nuisance parameters, with the π standing for the penalty term related to the assumption of a Gaussian distribution for the nuisance parameter. The second equation breaks down the expected number of events μ_i per bin i into the number of signal events s_i , depending on the $t\bar{t}$ cross section in the visible phase space $\sigma_{t\bar{t},\text{vis}}$ and all relevant nuisance parameters $\vec{\lambda}$, and the number of background events $b_{l,i}$ for each background process l . The backgrounds also depend on the nuisance parameters and the normalization of the respective background process ω_l .

The number of $t\bar{t}$ events depends on the $t\bar{t}$ production cross section, which allows to extract the latter from a fit of the former. Systematic uncertainties are included with nuisance parameters. The normalization of the background processes is also included as a nuisance parameter separately for each of the background processes.

The nuisance parameters are fitted as well, but the allowed parameter space of each nuisance parameter is typically restricted according to a priori assumptions based on external measurements. These assumptions are usually expressed as probability distributions also denoted as priors. In case these probability distributions are not flat a so-called penalty term is introduced to the fit to express the improbability of finding such a value for this specific systematic uncertainty.

A unit normal distribution is chosen as probability density function for nuisance parameters with Gaussian priors. Other nuisance parameters have a uniform prior and do not contribute any penalty terms. Since a uniform probability distribution has either a constant value or a value of zero, no special term for the nuisance parameter is preferred (unless it is forbidden), consequently no penalty term is needed.

As described above, the number of expected events for a background process also depends on the nuisance parameters. Especially nuisance parameters related to experimental systematic uncertainties affect the signal as well as the background processes. For example, the uncertainty on the muon reconstruction efficiency affects all events containing a muon (background as well as signal), while an uncertainty related to theory uncertainties usually only applies to the relevant process. The details can be found in Chapter 7.

The number of background events can then be decomposed into:

$$b_{l,i}(\omega_l, \vec{\lambda}) = b_{l,i}^{MC}(\vec{\lambda}) \cdot (1 + \omega_l). \quad (6.8)$$

Here, $b_{l,i}^{MC}$ denotes the expected number of events from the simulation of the respective background process and ω_l denotes the normalization. The number of background events in simulation depends on the nuisance parameters $\vec{\lambda}$. The uncertainty on the normalization of a specific process is propagated by variation of the respective ω_l .

Following the description in Section 6.4, the number of signal events is further divided according to the number of b-tagged jets. The number of events in the categories for events with zero or more than two b-tagged jets $s_{0,b}$, for events with exactly one $s_{1,b}$ and for events with exactly two b-tagged jets $s_{2,b}$ are expressed as follows:

$$s_{0,b} = \mathcal{L}_{\text{int}} \cdot \sigma_{t\bar{t},\text{vis}} \cdot \epsilon_{e\mu} \cdot (1 - 2\epsilon_b(1 - C_b\epsilon_b) - C_b\epsilon_b^2) \quad (6.9)$$

$$s_{1,b} = \mathcal{L}_{\text{int}} \cdot \sigma_{t\bar{t},\text{vis}} \cdot \epsilon_{ll} \cdot 2\epsilon_b(1 - C_b\epsilon_b) \quad (6.10)$$

$$s_{2,b} = \mathcal{L}_{\text{int}} \cdot \sigma_{t\bar{t},\text{vis}} \cdot \epsilon_{ll} \cdot \epsilon_b^2 C_b. \quad (6.11)$$

Only events in the $e^\pm\mu^\mp$ channel contribute to category $s_{0,b}$. Here, \mathcal{L}_{int} denotes the integrated luminosity, $\sigma_{t\bar{t},\text{vis}}$ the visible $t\bar{t}$ cross section and ϵ_{ll} the efficiency of the dilepton selection. The b-tagging efficiency ϵ_b is the probability to reconstruct a b-tagged jet in a $t\bar{t}$ event. It includes the efficiency of the b-tagging algorithm, the geometrical acceptance of the kinematic cuts on the b-tagged jet ($p_T > 30$ GeV, $|\eta| < 2.4$) and the probability of a light jet to be b-tagged. In general, the contribution of the geometrical acceptance and the mis-tag rate is comparably low (see Section 4.5 for the mistag rate). It is assumed that the two b-tagged jets can be identified independently of each other. Remaining correlations between the b-tagging efficiencies for both jets are described by the parameter C_b . These correlations can also be expressed in terms of the events measured in the separate categories: $C_b = 4s_{ll}s_{2,b}/(s_{1,b} + 2s_{2,b})^2$ where s_{ll} is the total number of selected $t\bar{t}$ events.

The values for ϵ_{ll} and s_i are obtained from simulation and depend on the nuisance parameters $\vec{\lambda}$. Any constraint of ϵ_{ll} and s_i also constrains the related nuisance parameters λ .

The visible cross section $\sigma_{t\bar{t},\text{vis}}$ corresponds to the cross section in the fiducial phase space as defined in Section 6.2. The requirement to select one b-tagged jet in the same-flavor channels is absorbed into ϵ_{ee} or $\epsilon_{\mu\mu}$ respectively. In the fiducial phase space all systematic uncertainties and the related nuisance parameters can be constrained.

The dependence of the template distributions on the nuisance parameters is modeled with a second order polynomial which is constructed using the nominal and the two systematically

varied values of each nuisance parameter $\lambda_m = 0, 1, -1$. The variation of the respective template distributions in each bin depends on the value of λ , with $\lambda = \pm 1$ corresponding to a $\pm 1 \cdot \sigma$ variation. If multiple template distributions are affected by one uncertainty or nuisance parameter, all of them are varied coherently. The template distributions are then added up to the expected number of events in each bin, as shown in Equation 6.7. The expected number of events consequently mirrors the dependence of the template distributions on the nuisance parameters. Some nuisance parameters are based on a one-sided variation so only one systematically varied value exists. In these cases, the dependence of the template distributions on the nuisance parameters is modeled by a linear function.

The MINUIT [99] algorithm is used to minimize the $-2 \ln(\mathcal{L})$ term (see 6.7) as function of the free fit parameters $\sigma_{t\bar{t}}$, $\vec{\omega}$ and $\vec{\lambda}$.

The nuisance parameters are a priori assumed to be uncorrelated, but the simultaneous fit takes possible correlations into account. Nuisance parameters having a similar effect on the fitted observables will be correlated by the fit. An example for this are the nuisance parameters for the uncertainties on the lepton efficiencies, as already discussed in Section 6.4. Both lepton efficiencies affect the number of events and the overall selection efficiency in a similar way in the $e^\pm \mu^\mp$ channel, leading to a strong correlation between these two parameters.

The choice of event categories and the parametrization of the likelihood function allow constraining several relevant systematic uncertainties of the $t\bar{t}$ cross section. Uncertainties related to jets and especially b jets are expected to be constrained after the fit. As shown below (see Chapter 7) this includes a wide array of different systematic uncertainties from the uncertainty on the b jet identification to the uncertainty on the scale for final state radiation in the parton shower. The uncertainties on the lepton efficiencies are expected to be constrained as well, due to the separation into the three decay channels. Uncertainties that change the normalization of all processes like the uncertainty on the trigger efficiency or the luminosity are not expected to be constrained by the fit.

6.6 Extrapolation from the visible to the full phase space

The previous section referred to the visible cross section in the fiducial phase space. In order to extrapolate this result to the full phase space an acceptance correction is determined. Similar to the cross section itself, some of the uncertainties need to be extrapolated.

The acceptance can be introduced by replacing the efficiency of the dilepton selection as follows:

$$\epsilon_{ll} = A_{ll}\epsilon_{ll}. \quad (6.12)$$

Here A_{ll} is the acceptance and ϵ_{ll} is the efficiency in the visible phase space, both depending on the nuisance parameters $\vec{\lambda}$. Correspondingly, the visible cross section can be extrapolated to the full cross section by dividing it by the acceptance: $\sigma_{t\bar{t}} = \sigma_{t\bar{t},\text{vis}}/A_{ll}$, again both the visible cross section and the acceptance depend on the nuisance parameters.

The acceptance is defined by the kinematic selection requirements on the leptons. As detailed in Section 6.2 the two leptons are required to be part of the $t \rightarrow Wb$ decay. They are further required to be within $|\eta| < 2.4$ with the leading lepton having $p_T > 25$ GeV and the trailing lepton $p_T > 20$ GeV. The invariant mass of the dilepton system is required to be $M_{\ell\ell} > 20$ GeV. The acceptance is calculated as the ratio of the number of $t\bar{t}$ events that fulfill these requirements to all $t\bar{t}$ events.

The values for the nuisance parameters that are determined in the fit of the visible cross section are propagated to the acceptance, including the correlations between the nuisance parameters. Similarly, the constraints for most of the nuisance parameters are applied to the calculation of the uncertainty of the acceptance. Some of the nuisance parameters that are constrained in the visual phase space are unconstrained in the extrapolation. Since the acceptance is defined in the simulation, after the parton shower, but before the detector simulation, uncertainties on the matrix element and parton shower affect the acceptance.

The following uncertainties are extrapolated: The uncertainty on the PDF, the top p_T uncertainty, the uncertainty on the matrix element scale and the uncertainties on the parton shower tune, the initial and final state radiation scales.

The extrapolation of an uncertainty takes the fitted value of each relevant nuisance parameter as central value. Then the change of acceptance for the explicit $\pm 1\sigma$ variation is considered as the $\pm 1\sigma$ variation on the acceptance. The additional uncertainties are then added to the uncertainty of the cross section, extrapolated to the full phase space, for each relevant nuisance parameter. The additional uncertainties are treated as uncorrelated and are added up in quadrature. This procedure can lead to asymmetric variations, even for originally symmetric variations in case the fitted value of the nuisance parameter is not the original central value.

Before discussing the results in Section 8.2, the next chapter gives a detailed description of the systematic uncertainties.

Chapter 7

Systematic uncertainties

Due to the size of the available dataset, the precision of the measurement of the $t\bar{t}$ cross section is dominated by systematic uncertainties and not by statistic uncertainties. In this analysis, the systematic uncertainties are treated as nuisance parameters in a template fit, as described in Chapter 6 . The nuisance parameters are determined in-situ allowing to reduce the impact of the systematic variations. Correlations between the variations are taken into account by fitting the nuisance parameters simultaneously. The nuisance parameters are usually described by a unit Gaussian distribution, describing the prior assumptions made about their behavior. These prior distributions (or priors) can also follow a uniform distribution depending on the specific nuisance parameter.

In this chapter the systematic uncertainties are described in detail starting with the uncertainties due to experimental effects in Section 7.1. The uncertainties based on theoretical assumptions are discussed in Section 7.2. The treatment of the systematics as nuisance parameters and the priors that are chosen to model the behavior of the respective nuisance parameter is discussed as well.

Broadly speaking there are two ways the systematic uncertainties can change the templates: They can affect the normalization of the templates, the shape or both. In practice, most uncertainties affect both the shape and the normalization, but some clearly affect one more than the other. An uncertainty can affect separate categories of events differently than others or affect all events similarly. Uncertainties on the normalization of all templates are in general harder to constrain than those affecting the shape of the templates as the normalization of the $t\bar{t}$ template is directly tied to the cross section which is the parameter of interest and thus not constrained by a prior.

All systematic uncertainties are summarized in Table 7.1. This includes a short summary of the systematic as well as the dominant effect (normalization or shape) and the assumed prior.

7.1 Experimental uncertainties

7.1.1 Uncertainties related to leptons

As described in Chapter 4, the simulated events are reweighted to model the lepton identification efficiencies in data using lepton p_T and η dependent scale factors. The efficiency measurements (expressed by the scale factors) have an uncertainty that is propagated to the final measurement by varying the scale factor for the electrons or muons within its uncertainty, resulting in a two-sided variation. The efficiency is measured with the tag-and-probe method, as described in Section 5.3.

For the electrons, the uncertainty on the efficiency measurement is the sum of several single sources, such as using alternative models for both the background contribution and the shape of the Z boson mass peak in the fit to the $M_{\ell\ell}$; distribution. The uncertainty due to the selection of the tag lepton is evaluated by changing the selection criteria in both data and simulation. These contributions are considered to be uncorrelated and are added up in quadrature. Since the uncertainties vary based on the kinematics of the electron, the electron efficiency uncertainty also has a small shape effect on the templates for signal and background. The larger effect is on the normalization and is of the order of $\sim 0.5\% - 2\%$ in the majority of the phase space.

In contrast, the muon efficiency uncertainty is estimated as an envelope of multiple effects. These include the binning and range that is used to model the Z boson mass peak as well as the variation of the assumed signal shape. As for the uncertainty on the electrons it also includes a change in the tag selection. The total uncertainty is 1.25% independent of the muon kinematics, resulting in a pure normalization uncertainty.

The measured energy of the leptons is scaled to correct the reconstruction for possible bias, as described in Sections 4.2 and 4.3. Additionally, the energy is smeared in simulation, such that the energy resolution is representative of the resolution in data. For both electrons and muons the corrections on simulation are varied to model the uncertainty.

For the electron energy, this uncertainty combines the effects of obtaining these corrections either in an electron or photon dominated sample, the choice of cuts used in the training and the choice of the simulated sample that is used in the training. It also includes an uncertainty on the method itself evaluated with a closure test and a correction for a possible dependence of the original energy of the electron. The uncertainty on the electron energy scale and smearing are then treated as separate nuisance parameters. The total effect follows a steeply falling function with the majority of the electrons having an energy variation in the range of $\leq 0.5\%$.

For muons, the uncertainty includes changing the mass range of the Z peak as well as a statistical component. The maximum deviation of each contribution are then added in quadrature to obtain the total systematic uncertainty. The majority of the muons receive an energy variation between 0.05% – 0.2%.

The variation on the lepton energies affect the number of selected events if a lepton has a nominal lepton p_T close to the threshold of the event selection. Otherwise, the impact of these uncertainties is small, as the template distributions in the fit do not directly depend on the leptons.

The systematic uncertainty on the trigger efficiency measurement is described in Section 5.5. This uncertainty is applied by varying the respective correction scale factor and it is correlated for all three lepton decay channels. Since it only weakly depends on the lepton kinematics it mainly affects the normalization of the templates used in the fit.

7.1.2 Uncertainties related to jets

As described in Section 6.4 the templates used for the cross section measurement are based on jet-related observables. Consequently, uncertainties related to jets tend to affect the templates directly. Since the event selection is inclusive for the number of jets in the $e^\pm\mu^\mp$ channel, the total number of events only weakly depends on the systematics related to jets.

The uncertainty on the correction of the jet energy, as described in Section 4.4, is split into 19 different sources depending on the p_T and η of the jets. These sources are treated as separate uncorrelated nuisance parameters [82, 88]. Similar to the nominal jet energy scale correction, the uncertainty is applied by rescaling the energy of each jet in the simulation. These variations include the differences in the behavior of jet fragmentation, initial and final state radiation between PYTHIA6 and HERWIG++ [100, 101]. They also include uncertainties due to the flavor of the jet again coming from a comparison of PYTHIA6 and HERWIG++, differentiating between gluons, b quarks, c quarks or all other quarks. Different methods to evaluate the correction of the jets themselves are compared and their difference is used as another uncertainty. Other sources of uncertainty are the variation of the response to a single particle in both the hadronic and electromagnetic calorimeters. The uncertainty due to the resolution of the jets is split into different regions depending on η . The uncertainty on the estimation of pile up is taken into account by both applying the uncertainty on the pile up correction (see Chapter 4) in simulation and comparing simulation with and without added pile-up. Finally the dependence on changing conditions during data taking, such as different calorimeter configurations, is taken into account by applying differences between corrections limited to a certain run period and the total average correction as uncertainties. The total

uncertainty on the jet energy scale combining all these sources is in the range of 1% – 2% in the phase space of this measurement.

The jets in simulation are corrected to match the resolution of the jet energy in data (see Section 4.4). The uncertainty depends on the η of the jet and on the p_T of the simulated jet (before detector reconstruction). The uncertainty on the correction is applied to each jet separately by repeating the resolution correction with a changed scale factor. This scale factor is not applied to the jet energy, but to the relative difference between the reconstructed jet and the jet at generator level. The uncertainty on this scale factor is in the range of $\sim 1\%$ in the barrel region and around 3.5% – 5% in the endcap region of the detector. The impact of this uncertainty is lower than the impact of the uncertainty on the jet energy scale corrections.

The systematic uncertainty on the efficiency to correctly identify a jet originating from a b quark is taken from a dedicated and unrelated measurement of the b-tag efficiency [92] using di-jet events. It is applied by reweighting simulated events according to these uncertainties. The uncertainty generally depends on p_T and η of the jet. Various sources are taken into account like the uncertainty on the simulation of B meson fragmentation, gluon splitting into quarks and meson branching fractions. Furthermore, experimental uncertainties like the impact of the jet energy scale are included by propagating them to the b-tagging efficiency. The uncertainty introduced through pile up (see Chapter 4) is evaluated by propagating the uncertainty on the pile-up determination to the b-tagging efficiency measurement. The uncertainty on the b-tagging efficiency is on the order of 2% – 6% in the bulk of the measured phase space.

The uncertainty on the probability that a jet originating from a light quark could be b-tagged is treated in a similar way.

The effect of the uncertainty on the b-tagging efficiency is well visible in the multiplicity of b-tagged jets in each event shown in Figure 7.1, especially in the ratio between the data and prediction. It also shows that the variation on the predicted number of events is larger than the statistical uncertainty on the amount of measured events, indicating that this variation is constrained in the template fit.

7.1.3 Further experimental uncertainties

The estimation of pile-up (see Chapter 4) in simulation is corrected according to the number of additional collisions per bunch crossing in data. The number of additional collisions is derived from the product of from the total inelastic proton proton cross section and the instantaneous luminosity. Events in simulation are reweighted depending on the number of primary vertices. The inelastic proton-proton cross section is measured with a precision of 4.6% by the ATLAS collaboration [102]. This uncertainty is propagated by varying the

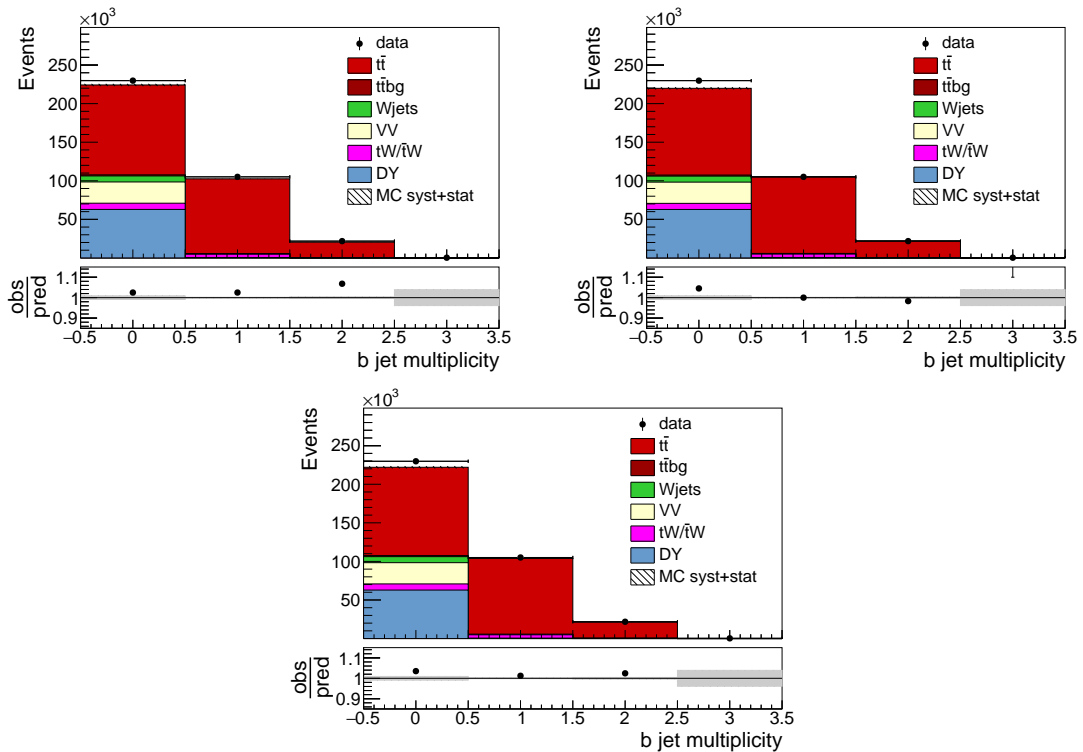


Figure 7.1: Multiplicity of b-tagged jets in the $e^\pm \mu^\mp$ channel for the two systematic variations (left, right) and the nominal (middle) b-tagging efficiency. The hatched bands correspond to the statistical uncertainty on the sum of the predicted yields. The ratios of the event yield in data to the sum of the predicted yields are shown at the bottom of each figure. Here, the solid gray band represents the contribution of the statistical uncertainty.

reweighting of the simulation. The impact of these variations is shown in the distribution of the number of primary vertices per event as shown in Figure 7.2. A mismatch between measured data and simulated events is visible in the nominal distribution, but as shown in the left figure, the systematic variations cover this discrepancy. This can lead to a fit result for the specific nuisance parameter tied to the systematic variation being different from zero.

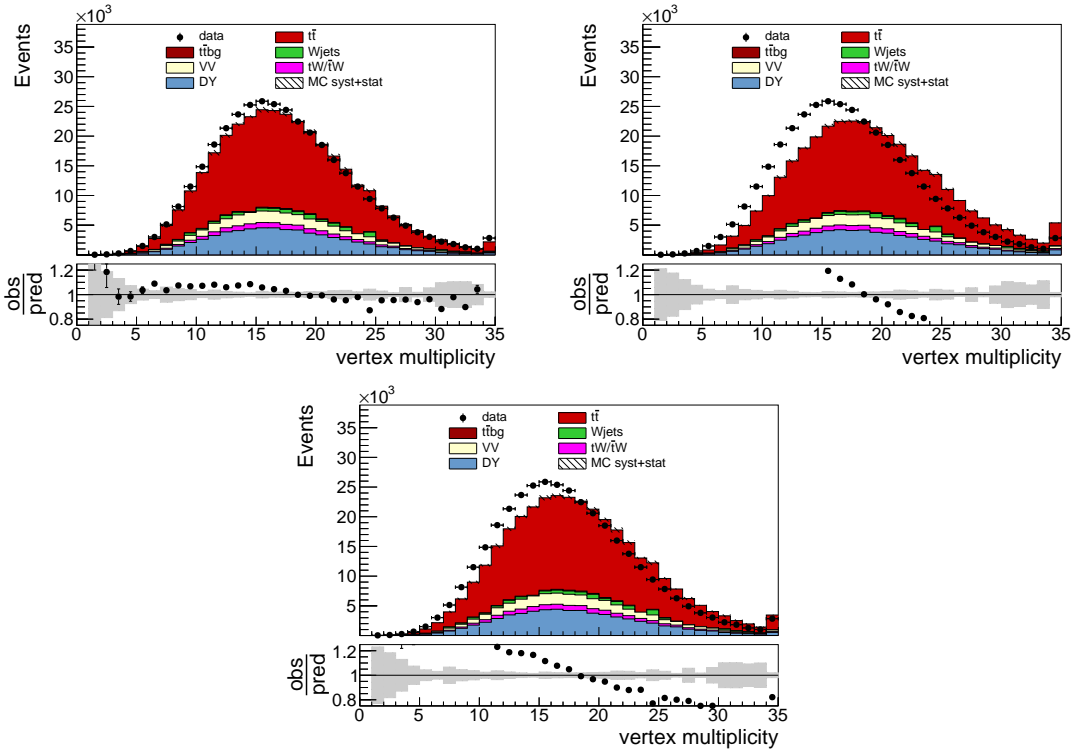


Figure 7.2: The number of primary vertices per event in the $e^+\mu^-$ channel for the two systematic variations (left, right) and the nominal (middle) pile-up corrections. The hatched bands correspond to the statistical uncertainty on the sum of the predicted yields. The ratios of the event yield in data to the sum of the predicted yields are shown at the bottom of each figure. Here, the solid gray band represents the contribution of the statistical uncertainty.

The integrated luminosity is determined by extrapolating the result of a measurement [96] of the instantaneous luminosity, using special proton beam conditions (Van der Meer scan [68]), to the full data taking period. The uncertainty on the luminosity is determined in a dedicated analysis by both taking into account the uncertainty on the initial measurement itself as well as uncertainties introduced in the extrapolation, mainly through changes in detector or beam conditions. The systematic uncertainty on the luminosity is totally independent from the measurement of the $t\bar{t}$ cross section and the other uncertainties described in this chapter. It is not included as a nuisance parameter in the fit. It is directly applied to the

final measurement of the $t\bar{t}$ cross section, by adding it in quadrature to the other uncertainties (see Equation 6.1)

7.2 Theoretical uncertainties

The distributions used in the fit are taken from simulation. In principle the physics model itself is not relevant, provided the simulation correctly predicts the event distribution for a given process. The Standard Model reliably predicts the event distribution for the processes in this measurement especially for $t\bar{t}$ production. The simulation is based on assumptions for multiple parameters, some of which are based on the SM. The uncertainties on the simulation are determined by the variation of these key parameters and they are evaluated by repeating the simulation with changed parameters. The nominal simulation is then replaced with the systematically varied simulation to propagate the uncertainty to the final measurement. The overall normalization of simulated $t\bar{t}$ events is not changed with respect to the nominal sample, so the theoretical uncertainties described have a larger effect on the shape of the templates used in the analysis than on the normalization. Changes of the overall normalization from the theoretical uncertainties are usually related to the cross section of the process that is simulated. Since separate uncertainties are assumed for the cross section of the background processes and the $t\bar{t}$ cross section is measured, the variations of the normalization from theory uncertainties do not need to be considered.

The `POWHEG` simulation generates $t\bar{t}$ events at NLO as described in Section 2.4. The impact of missing higher order corrections on the matrix element calculations is taken into account as an uncertainty. Following convention the renormalization and factorization scales (see Section 2.2.1) are varied by the factors 2 and 0.5 resulting in a two-sided variation. A uniform prior is used for the variation, with a value of unity between the $+1\sigma$ and -1σ variations and zero everywhere else. The impact of the matrix element scale variation is shown in Figure 7.3 for the distribution of the number of jets for events with one b-tagged jet for events in the $e^\pm\mu^\mp$ channel. These scale variations mostly affect the jets from matrix element calculations, which often correspond to the three jets with the highest reconstructed p_T . The p_T of the jets is influenced by the scale and this change of p_T propagates to the number of reconstructed jets due to the p_T requirement in the selection of jets. The same variation of the matrix element scale is applied to the single top background process.

A similar uncertainty is applied to the scale of the parton shower calculations as modeled by `PYTHIA8`, split between the scale parameter impacting initial state radiation (ISR) and final state radiation (FSR). For the ISR scale the parameter is again varied by a factor of 2 and 0.5 respectively. The FSR scale parameter is varied by a factor of $\sqrt{2}$ or $\sqrt{0.5}$, following the

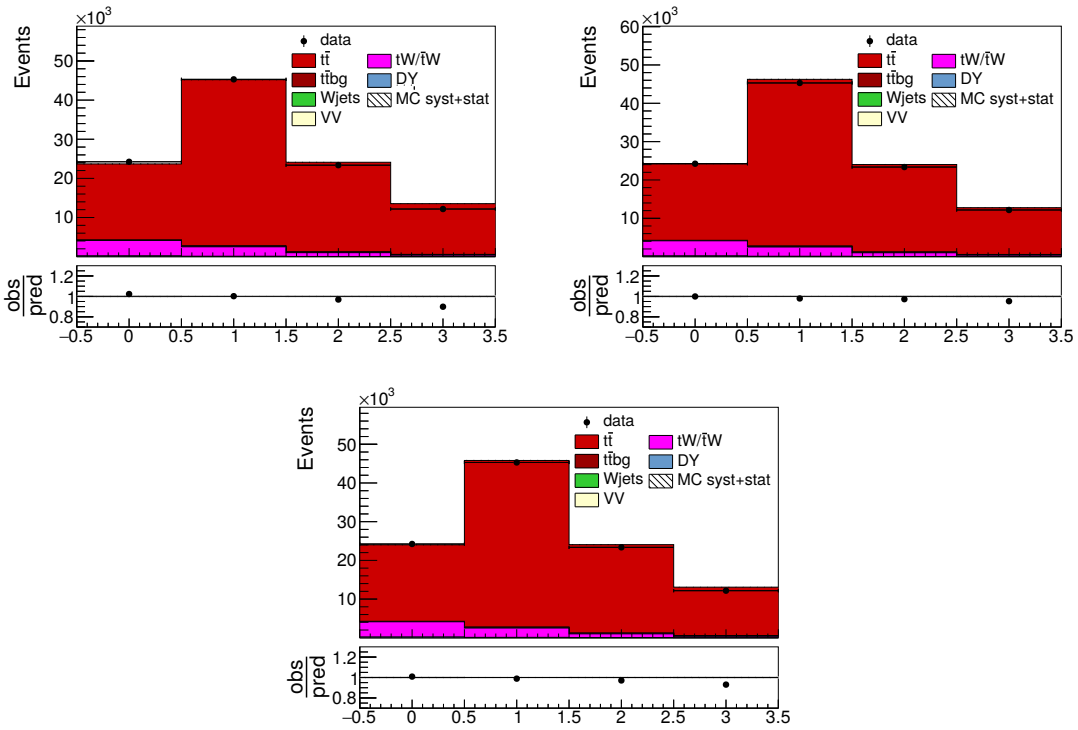


Figure 7.3: Number of additional jets for events with one b-tagged jet in the $e^\pm\mu^\mp$ channel for the two systematic variations (left, right) and the nominal $t\bar{t}$ matrix element scale. The hatched bands correspond to the statistical uncertainty on the sum of the predicted yields. The ratios of the event yield in data to the sum of the predicted yields are shown at the bottom of each figure. Here, the solid gray band represents the contribution of the statistical uncertainty.

recommendation in Ref. [65]. Possible correlations between these theoretical uncertainties and experimental uncertainties are taken into account by fitting all nuisance parameters simultaneously. Figures 7.4 and 7.5 show the variations to ISR and FSR respectively for the distribution of the number of additional jets for events with one b-tagged jet in the $e^\pm\mu^\mp$ channel. Up to three jets can originate from particles simulated in the matrix element calculations, so the impact of any changes in the parton shower scale are best seen in events with three or more additional jets. The ISR scale also affects the p_T of the $t\bar{t}$ system through the change in initial state radiation, while the FSR scale also affects the jet structure. The figures also show a change in overall normalization as events migrate between the different categories for the number of b-tagged jets. Similar variations are applied to the ISR and FSR scale for the single top background process.

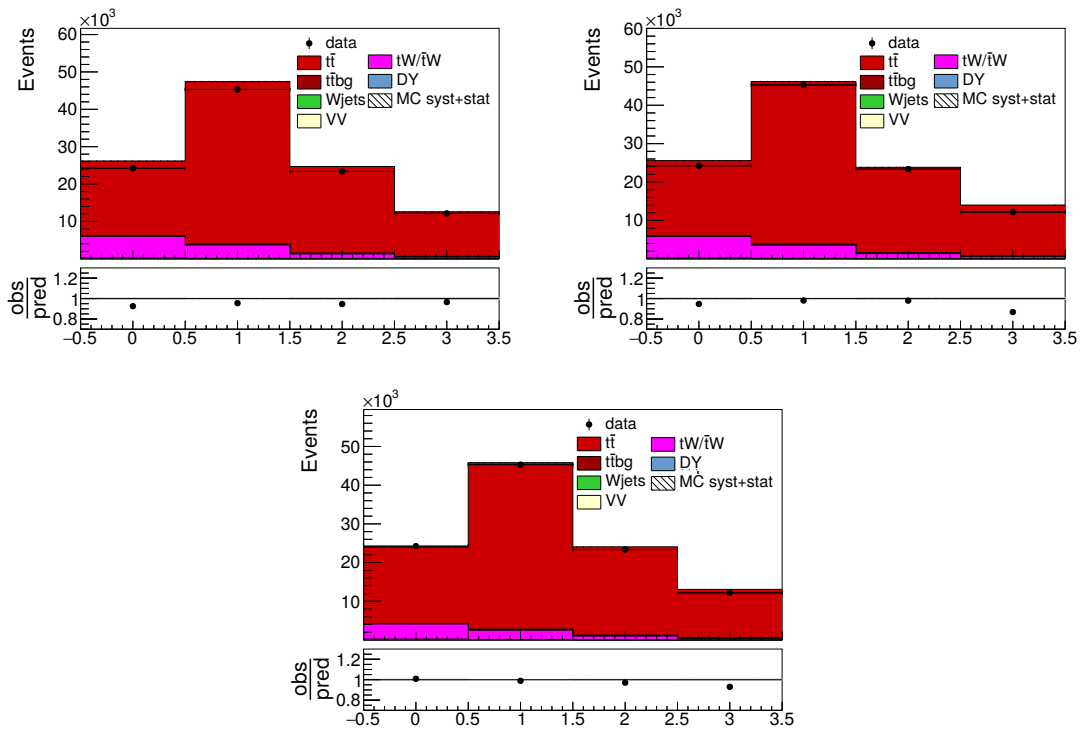


Figure 7.4: Number of additional jets for events with one b-tagged jet in the $e^\pm\mu^\mp$ channel for the two systematic variations (left, right) and the nominal ISR scale. The hatched bands correspond to the statistical uncertainty on the sum of the predicted yields. The ratios of the event yield in data to the sum of the predicted yields are shown at the bottom of each figure. Here, the solid gray band represents the contribution of the statistical uncertainty

The hardness of the first emission simulated in `POWHEG` is reduced (damped) according to the parameter h_{damp} by a factor of $h_{\text{damp}}^2/(h_{\text{damp}}^2 + p_T^2)$. In order to determine the systematic

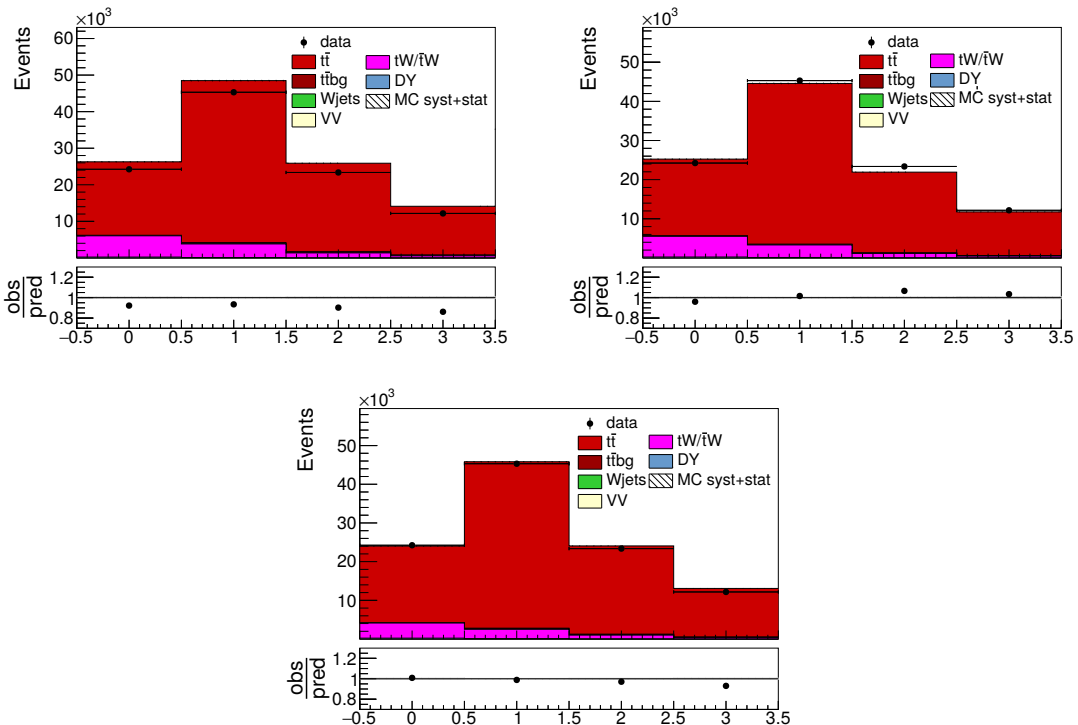


Figure 7.5: Number of additional jets for events with one b-tagged jet in the $e^\pm\mu^\mp$ channel for the two systematic variations (left, right) and the nominal FSR scale. The hatched bands correspond to the statistical uncertainty on the sum of the predicted yields. The ratios of the event yield in data to the sum of the predicted yields are shown at the bottom of each figure. Here, the solid gray band represents the contribution of the statistical uncertainty

variations, h_{damp} is varied within its uncertainty of $h_{\text{damp}} = 1.58^{+0.66}_{-0.59} m_t$, as determined by tuning measurements using data taken by CMS at a center of mass energy of 8 TeV [64]. In the context of this measurement the uncertainty is referred to as matching uncertainty.

The simulation of the underlying event is tuned to data measured by CMS [64]. The uncertainty from that tuning is propagated to the simulation resulting in a two-sided variation.

The dependence on the model of color reconnection used for the hadronization in PYTHIA is evaluated by comparing the nominal simulation with three different models [103, 104]. This results in three one-sided variations.

Differential measurements of the $t\bar{t}$ cross section [105] have shown that the simulation does not fully model the p_T distribution of the top quarks. This is likely due to higher-order effects as shown by differential NNLO calculations [106]. In order to model this disagreement a one-sided variation is introduced where simulated events are reweighted according to the p_T of the top quark with a factor of $\sqrt{SF(t)SF(\bar{t})}$ with $SF(p_T) = e^{0.0615 - 0.0005 \cdot p_T}$.

The uncertainty from the choice of PDF is evaluated using the variations provided by the CT14 PDF set [107]. Uncorrelated variations are constructed from the central CT14 result using 56 eigenvectors resulting in 28 two-sided variations. The variations are used at the 68 % confidence level. Each of the variations is treated as a separate nuisance parameter.

The branching ratio of B mesons in PYTHIA does not exactly agree with the values from the PDG [16]. Semileptonic decays of B mesons cause a different detector response compared to hadronic decays, which result in different b-jet energies. This uncertainty is modeled by reweighting the events so that the branching ratio in simulation agrees with the one in the PDG and the uncertainties on the prediction serve as systematic variations. These variations are given by a uniform nuisance parameter.

The momentum transfer from the b-quark to the B meson (fragmentation function) is controlled by PYTHIA and can influence the kinematics of the reconstructed b-jet. The default modeling uses the Bowler-Lund model [108] with the parameter of *StringZ* : *rFactB* = 0.855 [65, 64]. The respective parameter is tuned to LEP data and its uncertainty is used as a systematic variation, resulting in *StringZ* : *rFactB* = $0.855^{+0.224}_{-0.157}$. The Peterson fragmentation function [109] is used as an additional one-sided variation.

The Systematic uncertainties are summarized in Table 7.1. The next chapter describes the results of the measurement of the top quark pair production cross section. This includes the results of the fit for the systematic uncertainties.

Table 7.1: Table of the systematic uncertainties giving the name of the systematic as well as a short summary. The dominant effect of the systematic uncertainty describes whether it has more of an effect on the shape or on the normalization. The prior describes the chosen probability density function for the nuisance parameter.

Uncertainty	Dominant Effect	Prior	Short description
Experimental Uncertainties			
Electron efficiency	Normalization	Gaussian	0.5% – 2% on electron scale factor
Muon efficiency	Normalization	Gaussian	1.25% on muon scale factor
Electron energy	Shape	Gaussian	≤ 0.5% on electron energy
Muon energy	Shape	Gaussian	0.05% – 0.2% on muon energy
Trigger efficiency	Normalization	Gaussian	≤ 0.5% on trigger scale factor
Jet energy scale (JES)	Shape	Gaussian	19 sources, 1% – 2% total
Jet energy resolution (JER)	Shape	Gaussian	1% – 5% on resolution
b-tagging efficiency	Shape	Gaussian	2% – 6% on scale factor
Pile-up	Shape	Gaussian	4.6% on inelastic pp cross section
Luminosity	Normalization	Gaussian	2.6% on integrated luminosity
Theoretical Uncertainties			
Matrix element scale	Shape	Uniform	×2 \ 0.5 variation of $\mu_R \backslash \mu_F$
ISR scale	Shape	Uniform	×2 \ 0.5 variation of ISR scale
FSR scale	Shape	Uniform	$\times \sqrt{2} \backslash \sqrt{0.5}$ variation of ISR scale
Matching	Shape	Gaussian	$h_{damp} = 1.58^{+0.66}_{-0.59} m_t$ in POWHEG
Color Reconnection	Shape	Gaussian	3 models, one sided
Top p_T	Shape	Gaussian	$SF(p_T) = e^{0.0615 - 0.0005 \cdot p_T}$ one sided
PDF	Shape	Gaussian	56 Eigenvectors from CT14
B Meson BR	Shape	Uniform	semileptonic br reweighted to PDG value
B Meson fragmentation	Shape	Gaussian	$StringZ : rFactB = 0.855^{+0.224}_{-0.157}$ in PYTHIA

Chapter 8

Results

This chapter summarizes the results of the measurement of the $t\bar{t}$ production cross section at a center of mass energy of $\sqrt{s} = 13$ TeV. Before describing the main result in Section 8.2, the results for previous measurements with different data sets are shown in Section 8.1. The first cross section measurement of the $t\bar{t}$ cross section at $\sqrt{s} = 13$ TeV was measured with a small dataset using an integrated luminosity of $\mathcal{L}_{\text{int}} = 42 \text{ pb}^{-1}$ of data (see Section 8.1.1). After confirming the Standard Model expectation in this early measurement, a more precise measurement was performed with the full dataset taken in 2015 (see Section 8.1.2). These two previous measurements illustrate the increase in precision for $t\bar{t}$ cross section measurements at $\sqrt{s} = 13$ TeV.

The description of the main result starts by illustrating the result of the template fit with the fitted distributions in Section 8.2.1. A breakdown of the systematic uncertainties, including the fit results for relevant nuisance parameters, is given in Section 8.2.2.

The measured $t\bar{t}$ production cross section is compared to the theory prediction as well as to results from other experiments in Section 8.3.

The effect of adding events from the single muon channel to the fit is discussed in Section 8.4.

The top quark pole mass is extracted in Section 8.5, based on the main result for the measurement of the $t\bar{t}$ production cross section.

8.1 Results with the 2015 data sets

Both results for the $t\bar{t}$ cross section presented in this section are measured with data taken in 2015 by the CMS detector. The measurements use the same basic method as the main result with the key difference of using only the $e^\pm\mu^\mp$ decay. They were both used to cross check the main results in publications by the CMS collaboration [110, 111].

8.1.1 First measurement of the top pair production cross section at 13 TeV

The first measurement of the $t\bar{t}$ production cross section at $\sqrt{s} = 13$ TeV used $\mathcal{L}_{\text{int}} = 42 \text{ pb}^{-1}$ taken early in during the 2015 LHC run. It is aimed at discovering possible deviations from the Standard Model at a new collision energy. The analysis strategy is the same as for the main analysis, as described in Chapter 6, with a few differences:

- In order to reduce the contamination from background processes, only events in the $e^\pm\mu^\mp$ channel are selected for the measurement.
- Due to the statistics in data, the event yields are chosen as templates for the fit instead of kinematic distributions of jets (see Figures 6.6 for the templates used in the main result).
- A very simple strategy is used to select events at the trigger level, since the low amount of available data makes any more comprehensive treatment difficult.
- Systematic uncertainties are in general less detailed, especially theory based the uncertainties on the simulation. Due to large uncertainties from data statistics and luminosity, a more detailed study of further systematic uncertainties can be neglected.

Using the template fit, the $t\bar{t}$ cross section in the full phase space is measured as:

$$\sigma_{t\bar{t}} = 778 \pm 54(\text{stat}) \pm 61(\text{syst}) \pm 76(\text{lumi}) \text{ pb}. \quad (8.1)$$

The uncertainty on the luminosity is the highest single uncertainty, but the statistical uncertainty and the uncertainty from the other systematic sources are of the same order of magnitude. The breakdown of the systematic uncertainties is shown in Table 8.1.

The total uncertainty of the measurement is dominated by experimental uncertainties. The contribution from theoretical uncertainties is negligible. Besides the uncertainty on the luminosity, the largest uncertainties come from the backgrounds, the determination of trigger, lepton efficiencies and jet energy scales. The chosen templates for the fit show little discrimination between signal and background, leading to large contributions from the background uncertainties. Similarly, there is little sensitivity for the jet energy scale in the templates, which limits the constraining power of the fit.

The high contribution from the trigger efficiency uncertainty shows the importance of maximizing the trigger efficiencies and minimizing their uncertainties. This is the main motivation for the detailed trigger studies, described in Chapter 5.

Table 8.1: Results of the first measurement of the $t\bar{t}$ cross section at $\sqrt{s} = 13$ TeV. The systematic uncertainties are broken down by their sources.

Name	Contribution [%]
Trigger	± 4.0
Lepton ID/isolation	± 3.4
Lepton energy scale	± 0.2
Jet energy scale	± 2.7
Jet energy resolution	± 0.1
B-tag	± 0.8
Mistag	± 0.2
Pile-up	± 0.7
NLO generator	± 0.1
Q^2 scale	± 0.1
PDF	± 1.9
DY background	± 6.3
Single top background	± 1.5
Diboson background	± 3.5
$t\bar{t}$ background	± 0.3
W+jets background	± 0.4
Luminosity	± 11.1
Stat	∓ 6.9
Total vis	± 15.6
$\sigma_{t\bar{t}}(13 \text{ TeV})$ vis	12.5 pb
Q^2 scale (extr)	∓ 0.3 ± 0.0
PDF (extr)	± 1.6 ± 1.1
Total	± 15.6 ± 13.0
$\sigma_{t\bar{t}}(13 \text{ TeV})$	778 pb

8.1.2 Measurement of the top quark pair production cross section with the 2015 data set

This measurement of the $t\bar{t}$ production cross section at $\sqrt{s} = 13$ TeV uses the full 2015 dataset taken by CMS with a luminosity of $\mathcal{L}_{\text{int}} = 2.2 \text{ fb}^{-1}$. It should confirm the previous measurement (see Section 8.1.1) and allow a more precise comparison with theoretical predictions. The analysis strategy is again very similar to the strategy for the main result, as described in Chapter 6, with the following differences:

- Only events in the $e^\pm\mu^\mp$ channel are used.
- The trigger selection is similar to the one described in Section 5.1, but no detailed study on the systematic uncertainty on the trigger efficiency measurement is made (compare to Section 5.4).
- The determination of theoretical systematic uncertainties uses a simpler method, compared to the main result.

With the template fit the $t\bar{t}$ cross section measured to be:

$$\sigma_{t\bar{t}} = 793 \pm 7(\text{stat}) \pm 27(\text{syst}) \pm 21(\text{lumi}) \text{ pb.} \quad (8.2)$$

Compared to the analysis with early 2015 data, the uncertainty is reduced significantly. The decrease in statistical uncertainty reflects the larger dataset. The luminosity was determined with a higher precision, leading to a lower uncertainty on the $t\bar{t}$ cross section [112]. The systematic uncertainties are detailed in Table 8.2.

Here, the main systematic uncertainties are the uncertainty on the PDF, the single top background, and the trigger and lepton efficiency uncertainties. The uncertainty from the PDF is hard to constrain in the fit itself, but the main result uses an updated PDF set with lower uncertainties. Similarly, the single top process is very hard to distinguish from the $t\bar{t}$ signal. It has the same final state and very similar kinematic behavior, consequently this uncertainty is mostly irreducible.

The uncertainty on the trigger efficiency measurement again motivated the studies to reduce the associated systematic uncertainty (see Section 5.4).

Measuring the $t\bar{t}$ cross section simultaneously in all three decay channels at least allows constraining the larger of the two lepton uncertainties as explained in Section 6.4. Consequently the same flavor channels are added to the measurement of the $t\bar{t}$ cross section for the main result, as presented below.

Table 8.2: Results of the $t\bar{t}$ cross section at $\sqrt{s} = 13$ TeV with the full 2015 dataset. The systematic uncertainties are broken down by their sources. The uncertainty from the luminosity is externalized from the fit and not included in the table.

Name	Contribution [%]
Trigger	1.3
Lepton ID/isolation	1.4
Lepton energy scale	0.5
Jet energy scale	1.2
Jet energy resolution	0.1
B-tag	0.3
Mistag	0.1
Pile-up	0.3
NLO generator	0.2
Q^2 scale	0.5
PDF	1.7
Parton Shower	0.4
BG_tW/bartW	1.5
DY background	0.5
Diboson background	0.2
$t\bar{t}$ background	0.3
W+jets background	0.6
Stat	0.9
Total vis	3.2
$\sigma_{t\bar{t}}(13 \text{ TeV}) \text{ vis}$	12.73 pb
Q^2 scale (extr)	$\pm^{0.5}_{0.1}$
PDF (extr)	$\pm^{1.0}_{1.7}$
Total	$\pm^{3.5}_{3.3}$
$\sigma_{t\bar{t}}(13 \text{ TeV})$	793 pb

8.2 Measurement of the top quark pair production cross section with the 2016 data set

As described in Chapter 6, the $t\bar{t}$ production cross section is measured using a template fit. The cross section is first measured in the visible phase space requiring a dileptonic decay with the two leptons meeting the requirements of $p_T(\text{lead}) > 25 \text{ GeV}$, $p_T(\text{sublead}) > 20 \text{ GeV}$, $|\eta| < 2.4$ and $M_{\ell\ell} > 20 \text{ GeV}$. The result for the visible cross section is:

$$\sigma_{t\bar{t},\text{vis}} = 24.88 \pm 0.05(\text{stat}) \pm 0.65(\text{syst}) \pm 0.62(\text{lumi}) \text{ pb.}$$

The cross section is then extrapolated to the full phase space, resulting in:

$$\sigma_{t\bar{t}} = 827 \pm 2(\text{stat}) \pm 24(\text{syst}) \pm 21(\text{lumi}) \text{ pb.}$$

These results are more precise than the two results presented above, showing the improvement of the measurement. All three results are consistent within their uncertainties.

8.2.1 Post-fit template distribution

The results of the measurement of the $t\bar{t}$ cross section can be applied to the distributions used in the fit, including the fitted values for the nuisance parameters and their constraints. The nuisance parameters are applied to the templates following the interpolation described in Section 6.5. All nuisance parameters are considered including those related to the normalization of the background templates.

The resulting distributions are shown in Figures 8.1, 8.2 and 8.3, with the background processes being merged into one contribution.

The figures show that simulation agrees with the data after applying the fitted parameters. The agreement can be expected and shows that the fit successfully scales simulation to data and the simulation is able to model the data within its uncertainties. The post-fit uncertainties are smaller compared to the figures showing the non-constrained uncertainties in Figure 6.6, 6.7 and 6.8, which shows their constraints from the fit.

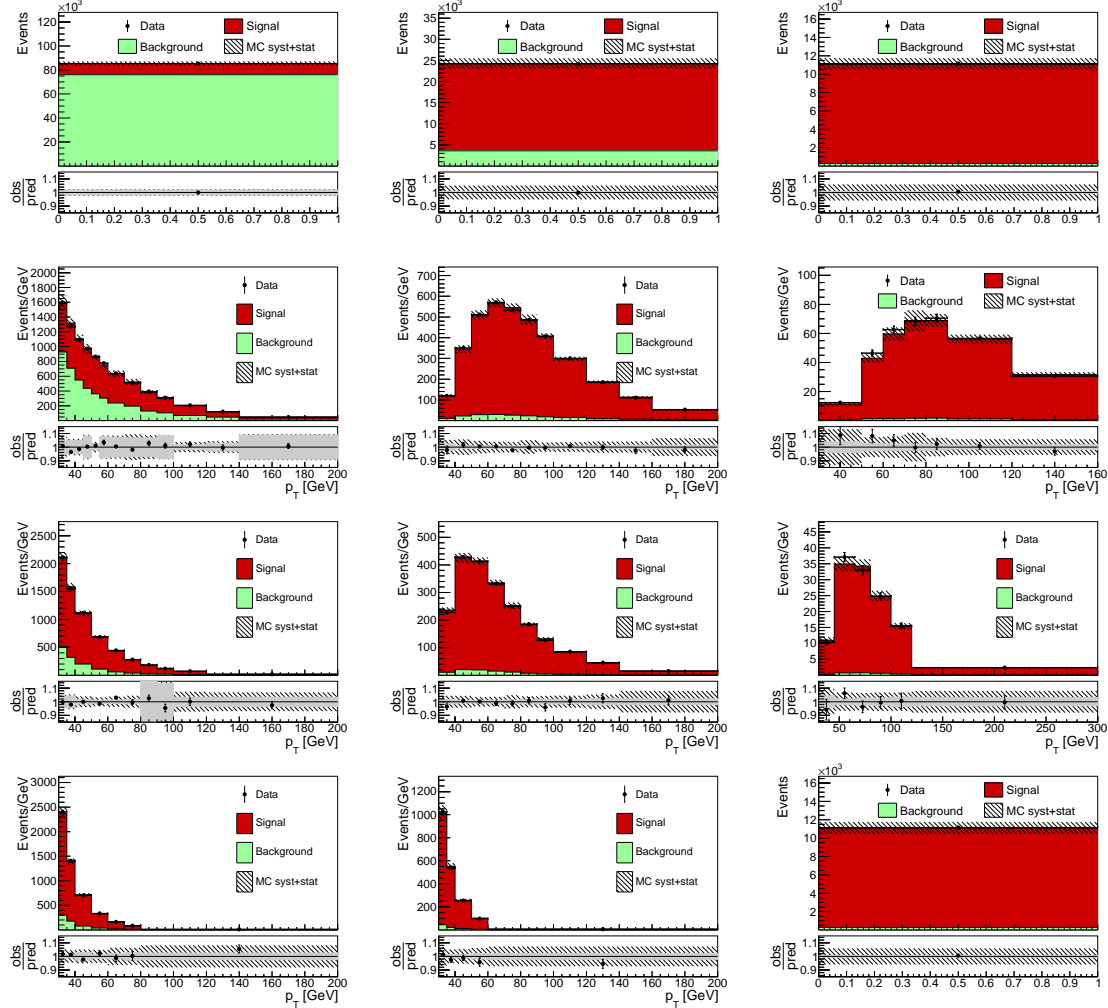


Figure 8.1: Fitted distributions ($e^\pm \mu^\mp$ channel) for events with zero as well as three or more b-tagged jets (left column): Total event yield for zero (top) and the p_T of the jet with the lowest p_T one (second from top), two (second from bottom) or three or more (bottom) additional jets. The same distributions for events with one b-tagged jet (middle column) and two b-tagged jets (right column) are shown below. The hatched bands correspond to the total uncertainty on the sum of the predicted yields. The ratios of data to the sum of the predicted yields are shown at the bottom of each figure. Here, the solid gray band represents the contribution of the statistical uncertainty.

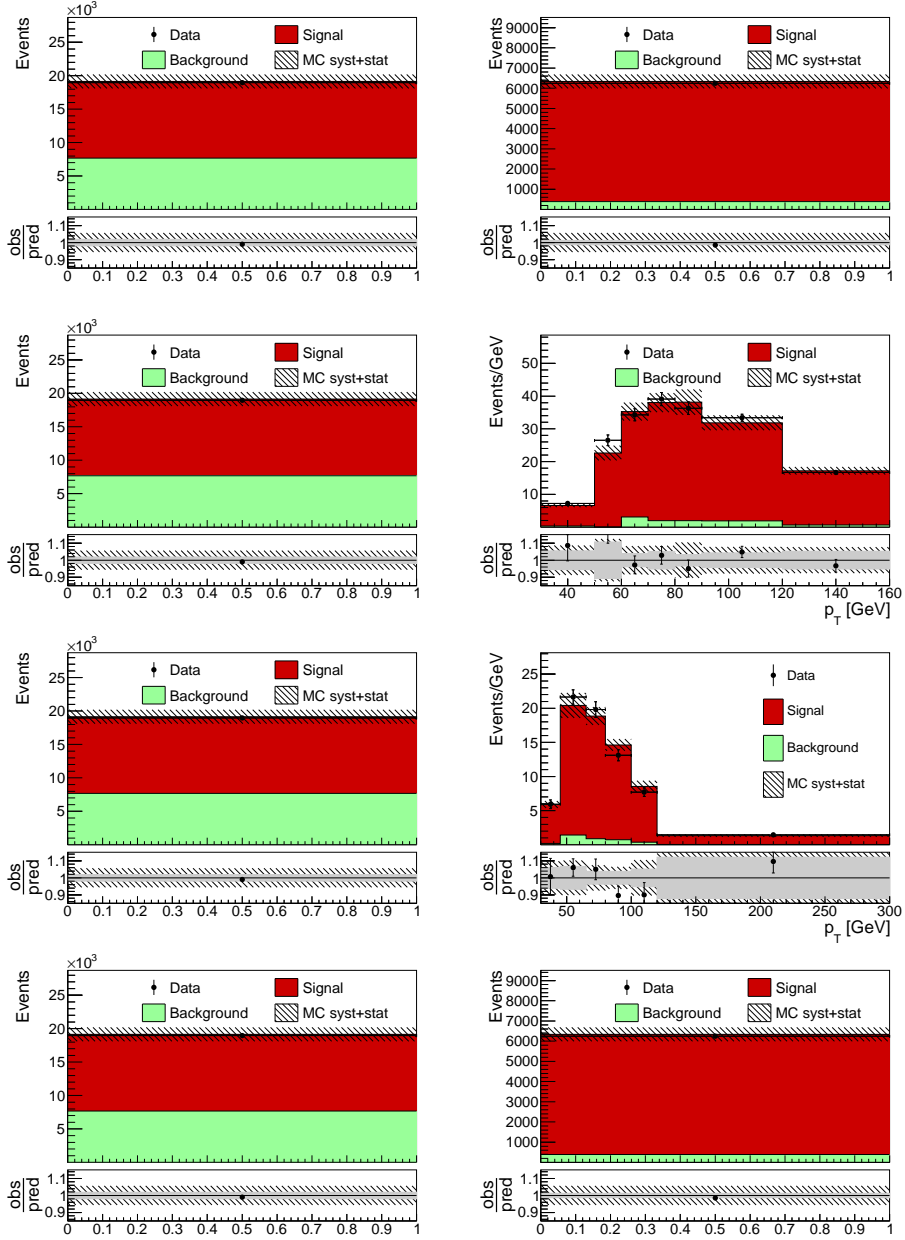


Figure 8.2: Fitted distributions ($\mu^+\mu^-$ channel): The left column shows events with one b-tagged jet and the total event yield for events with zero (top), one (second from top) two (second from bottom) or three or more additional jets (bottom). The right column shows events with two b-tagged jets and the total yield for events with zero additional jets (top), the p_T of the jet with the lowest p_T for one (second from top), two (second from bottom) or three or more (bottom) additional jets. The hatched bands correspond to the total uncertainty on the sum of the predicted yields. The ratios of data to the sum of the predicted yields are shown at the bottom of each figure. Here, the solid gray band represents the contribution of the statistical uncertainty.

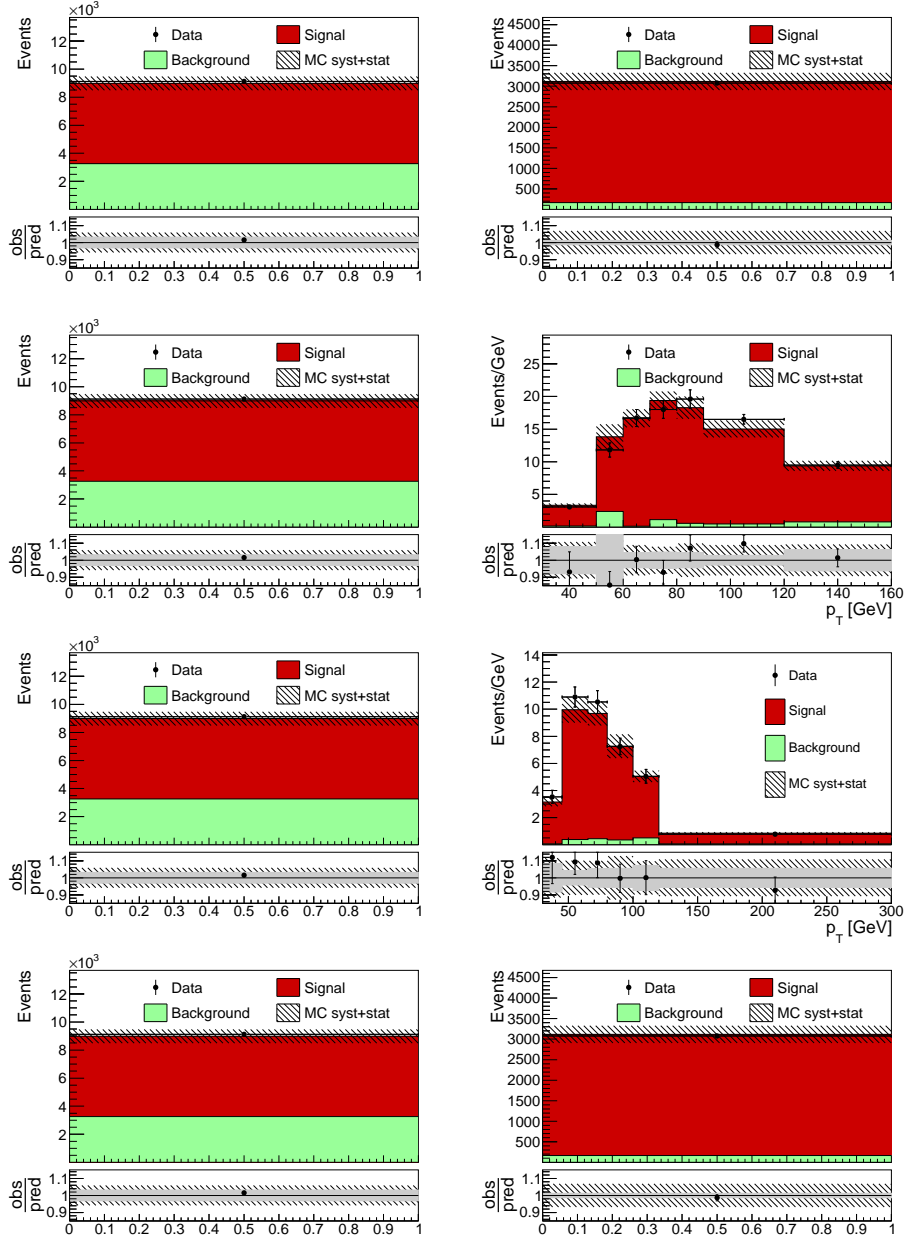


Figure 8.3: Fitted distributions (e^+e^- channel): The left column shows events with one b-tagged jet and the total event yield for events with zero (top), one (second from top) two (second from bottom) or three or more additional jets (bottom). The right column shows events with two b-tagged jets and the total yield for events with zero additional jets (top), the p_T of the jet with the lowest p_T for one (second from top), two (second from bottom) or three or more (bottom) additional jets. The hatched bands correspond to the total uncertainty on the sum of the predicted yields. The ratios of data to the sum of the predicted yields are shown at the bottom of each figure. Here, the solid gray band represents the contribution of the statistical uncertainty.

8.2.2 Results for systematic uncertainties

As described in Section 6.5, the results of the fit include the value of $t\bar{t}$ production cross section as well as the results for the fitted nuisance parameters. For the nuisance parameters a fitted value (also called pull) of 0 stands for the nominal result, while a value of ± 1 stands for the $\pm 1 \sigma$ variation. The impact of each of the nuisance parameters on the cross section is estimated by fixing one nuisance parameter to the nominal value and repeating the fit. The reduction in the resulting uncertainty on the cross section is then considered as the contribution of that single uncertainty. This calculation does not consider correlations between multiple uncertainties, so the quadratic sum of the contributions of all uncertainties does not correspond to the total uncertainty.

Table 8.3 shows the contributions from the most relevant uncertainties. Suitable uncertainty sources are combined. It also shows the result for the cross section itself and for the extrapolation of the full to the visible phase space, including the extrapolation of the relevant uncertainties. Figure 8.4 shows the pulls and constraints for the most relevant systematic uncertainties. The contributions of all single uncertainty sources, together with their pulls and constraints, are shown in Appendix A.

The results for the lepton (electron and muon) ID uncertainties can be described together as they are highly correlated. As explained in Section 6.4, the higher of the two uncertainties (the electron uncertainty) is constrained and the lower of the two (the muon uncertainty) is largely unconstrained. Compared to the constraints, the values for the pulls are small. The lepton uncertainties have the largest contribution to the total uncertainty from all single uncertainties with about $\sim 2\%$.

Since the trigger uncertainty is an overall normalization uncertainty on all templates, its size directly propagates to the final uncertainty, but it is neither pulled nor constrained.

The 28 uncertainty sources for the PDF are related to the uncertainty for the PDF represented in eigenvectors. They contribute to the uncertainty on the measured cross section up to about 0.4% per individual uncertainty. Overall, they are not strongly constrained and the pull hardly differs from the nominal value. During the extrapolation of the cross section from the visual to the full phase space the PDF uncertainties contribute again, as described in Section 6.6, in the order of 1.1% in total.

Other theoretical uncertainties do not significantly contribute to the total uncertainty, since they are either constrained or their impact is small.

Events containing a single top quark and a W boson behave very similar to events from $t\bar{t}$ production. The cross section of tW production is low compared to the cross section of $t\bar{t}$ production, but due to the similarities between both types of events there is still a considerable

Table 8.3: Results of the $t\bar{t}$ cross section at $\sqrt{s} = 13$ TeV with the full 2016 dataset. The systematic uncertainties are broken down by their sources. The uncertainty from the luminosity is externalized from the fit and not included in the table.

Name	Contribution [%]
Trigger	0.3
Lepton ID/isolation	2.1
Lepton energy scale/resolution	0.1
Jet energy scale	0.4
Jet energy resolution	< 0.1
B-tag	0.2
Mistag	0.1
Pile-up	0.2
$t\bar{t}$ ME scale	0.2
tW ME scale	< 0.1
PDF	1.1
Top p_T	0.5
ME/PS matching	0.1
UE tune	0.3
$t\bar{t}$ FSR scale	0.5
$t\bar{t}$ ISR scale	0.2
tW FSR scale	< 0.1
tW ISR scale	< 0.1
B-hadron BR	0.1
fragmentation	0.4
CR QCD-inspired	0.3
tW background	1.1
DY background	1.0
Diboson background	0.3
$t\bar{t}$ background	0.3
W+jets background	0.2
Stat	0.2
Total vis	2.6
$\sigma_{t\bar{t}}(13 \text{ TeV})$ vis	24.88 pb
$t\bar{t}$ ME scale (extr)	$\pm^{0.3}_{0.1}$
PDF (extr)	$\pm^{0.8}_{0.6}$
Top p_T (extr)	$\pm^{0.8}_{0.0}$
$t\bar{t}$ ISR scale (extr)	$\pm^{0.1}_{0.0}$
$t\bar{t}$ FSR scale (extr)	$\pm^{0.1}_{0.0}$
UE tune (extr)	$\pm^{0.0}_{0.0}$
Total	$\pm^{2.9}_{2.6}$
$\sigma_{t\bar{t}}(13 \text{ TeV})$	827 pb

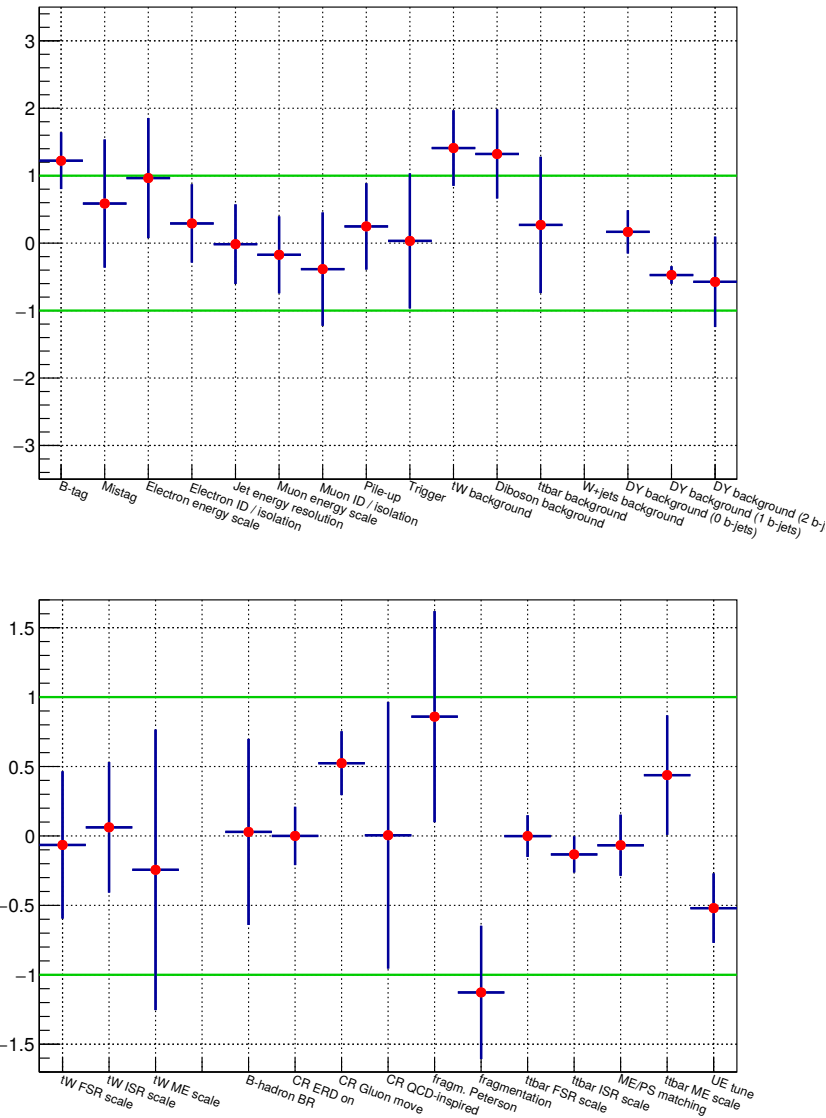


Figure 8.4: Pulls and constraints of the most relevant experimental (left) and theoretical (right) systematic uncertainties.

impact. The uncertainty on the tW production cross section has an impact of about 1.1% on the measured $t\bar{t}$ cross section.

The uncertainty on the production cross section of Drell-Yan events is explicitly decorrelated according to the number of b-tagged jets (corresponding to the event categorization in the fit). Added in quadrature the total contribution to the total uncertainty is 1%.

8.3 Comparison to theory predictions and previous results

The cross section in the full phase space is found to be:

$$\sigma_{t\bar{t}} = 827 \pm 2(\text{stat}) \pm 24(\text{syst}) \pm 21(\text{lumi}) \text{ pb.} \quad (8.3)$$

This result is in agreement with the theoretical prediction for the $t\bar{t}$ production cross section calculated with the Top++ program [113] at NNLO in perturbative QCD, including soft-gluon resummation to the next-to-next-to-leading log [114] of :

$$\sigma_{t\bar{t}} = 832 \pm^{20}_{29} (\text{scale}) \pm 35(\text{PDF} + \alpha_s) \text{ pb.} \quad (8.4)$$

This measurement is also in agreement with a previous CMS measurements of the $t\bar{t}$ production cross section in the dilepton channel [111]:

$$\sigma_{t\bar{t}} = 815 \pm 9(\text{stat}) \pm 38(\text{syst}) \pm 19(\text{lumi}) \text{ pb.} \quad (8.5)$$

In the semileptonic channel the $t\bar{t}$ production cross section was measured by CMS as well [115]:

$$\sigma_{t\bar{t}} = 888 \pm 2(\text{stat}) \pm 26(\text{syst}) \pm 20(\text{lumi}) \text{ pb.} \quad (8.6)$$

This result has a similar precision compared to the measurement presented in this work. The central values are quite far apart, but there is no tension between these results when accounting for the systematic uncertainties, which are mostly uncorrelated.

The result presented in this work is also consistent with the latest measurement from the ATLAS collaboration in the dilepton channel [116]:

$$\sigma_{t\bar{t}} = 818 \pm 8(\text{stat}) \pm 27(\text{syst}) \pm 19(\text{lumi}) \text{ pb.} \quad (8.7)$$

Overall, the $t\bar{t}$ production cross section presented in this work agrees with the theoretical prediction as well as with previous measurements.

8.4 Addition of the semileptonic channel

The uncertainty due to the lepton efficiencies is the dominant uncertainty for the measurement of the $t\bar{t}$ production cross section. The correlation between the nuisance parameters for the lepton uncertainties is introduced by fitting all three dilepton channels together, as explained in Section 6.4. Similarly, the uncertainty due to the lepton efficiencies could be further constrained by adding semileptonic channels to the fit.

In order to asses the feasibility of a combination of the dilepton channel with the semileptonic channel, events with exactly one muon in the final state are added to the fit of the $t\bar{t}$ production cross section. In order to reduce the complexity the fit is performed for a reduced number of systematic uncertainties. Theory based uncertainties with little impact on the measurement, such as the uncertainties on color reconnection or fragmentation, are not considered. In order to simulate the background processes the same simulation as in the dilepton channel is used. In general, this is should not be seen as a full measurement, but as a feasibility study.

Since no separate study on the background contributions in the single muon channel is performed, hard selection requirements are chosen: Events are required to contain exactly one muon with $p_T > 30 \text{ GeV}$ and $|\eta| < 2.4$ and two b-tagged jets with $p_T > 30 \text{ GeV}$ and $|\eta| < 2.4$. The muon and the jets are defined as described in Section 6.2. These requirements also define the visible phase space. Distributions of the jet p_T are chosen as observables for the template fit, in analogy to the dilepton channel, as described in Section 6.4. The uncertainty on the trigger efficiency is increased to 1% (before the fit), since no dedicated study on the efficiency of the single muon triggers and its uncertainty is performed.

Including these events into the fit yields the following result:

$$\sigma_{t\bar{t}} = 835 \pm 1(\text{stat}) \pm 18(\text{syst}) \pm 21(\text{lumi}) \text{ pb.} \quad (8.8)$$

This result is consistent with the main result in the dilepton channel. The uncertainty is reduced mainly, due to the reduced impact of the uncertainty on the lepton efficiency. This uncertainty is reduced from 2.1% to 1.3%. At the same time the uncertainty on the extrapolation to the full phase space is slightly increased, since a requirement on jets is included for the single-muon channel. Jets are in general more affected by the uncertainty on the parton shower, compared to leptons, which leads to an increased impact of these uncertainties in the extrapolation.

The reduction in uncertainty and the agreement with the main result show that the inclusion of the semileptonic channel is a viable method to decrease the uncertainties on the measured $t\bar{t}$ production cross section.

8.5 Extraction of the top quark pole mass

The value of the top quark pair production cross section depends on the mass of the top quark. Using this dependence, the top quark mass can be extracted from a $t\bar{t}$ cross section measurement using a mass dependent prediction [37]. In the context of this work the pole or on-shell definition of the top quark mass, m_t^{pole} , is used. The dependence of the top quark mass set for the simulation is estimated by repeating the $t\bar{t}$ cross section measurements for different settings for the top quark mass. The following cross section results are measured (with the second being the main result):

$$\begin{aligned}\sigma_{t\bar{t}} &= 814 \pm 2(\text{stat}) \pm 24(\text{syst}) \pm 20(\text{lumi}) \text{ pb for } m_t^{\text{MC}} = 175.5 \text{ GeV}, \\ \sigma_{t\bar{t}} &= 827 \pm 2(\text{stat}) \pm 24(\text{syst}) \pm 21(\text{lumi}) \text{ pb for } m_t^{\text{MC}} = 172.5 \text{ GeV} \\ \text{and } \sigma_{t\bar{t}} &= 843 \pm 2(\text{stat}) \pm 24(\text{syst}) \pm 21(\text{lumi}) \text{ pb for } m_t^{\text{MC}} = 169.5 \text{ GeV}.\end{aligned}$$

The prediction for the top quark pair production cross section is calculated at NNLO [117–119, 29] with the Hathor[120] framework. The calculation uses the NNPDF3.1nnlo PDF set [121] with full uncertainties, including the uncertainty on α_S . The renormalization and factorization scales are set to the top quark mass and varied independently to determine the respective uncertainties.

The measured and predicted $t\bar{t}$ cross sections are compared with a χ^2 minimization in the QCD analysis framework xFitter [122], with the χ^2 definition following Ref [15]. The fit is performed for eleven cross section predictions, with the top quark pole mass varied in the range of $170 \text{ GeV} < m_t^{\text{pole}} < 175 \text{ GeV}$. The optimal top quark pole mass $m_{t,\min}^{\text{pole}}$ is determined from a parabolic parametrization of the dependence of the χ^2 on the top quark pole mass:

$$\chi^2 = \chi_{\min}^2 + \left(\frac{m_t^{\text{pole}} - m_{t,\min}^{\text{pole}}}{\sigma(m_{t,\min}^{\text{pole}})} \right)^2. \quad (8.9)$$

Here, $\sigma(m_{t,\min}^{\text{pole}})$ is the uncertainty on $m_{t,\min}^{\text{pole}}$ including the experimental and the PDF uncertainties, while χ_{\min}^2 is the χ^2 value at the minimum. The uncertainty from the scales in the theory prediction and the dependence on m_t^{MC} in the measurement is determined by repeating the whole fit, varying the theoretical prediction or the experimental result, respectively. The χ^2 for the nominal choice of scale and m_t^{MC} is shown in Figure 8.5. The dependence of the χ^2 on m_t^{pole} is well modeled by the parabolic fit.

The uncertainty from the dependence of the cross section on m_t^{MC} is rescaled from the original 3 GeV variation to a 1 GeV variation, assuming a linear behavior.

The final result for the top quark pole mass is:

$$m_t^{\text{pole}} = 171.9 \pm 1.4(\text{exp} + \text{pdf} + \alpha_S) \pm 2.0(\text{scale}) \pm 0.2(m_t^{\text{MC}}) \text{GeV}. \quad (8.10)$$

This is consistent with the top quark pole mass measured by the CMS collaboration as $m_t^{\text{pole}} = 173.8 \pm 1.8 \text{ GeV}$ [37] and the ATLAS collaboration as $m_t^{\text{pole}} = 172.9 \pm 2.6$ [36].

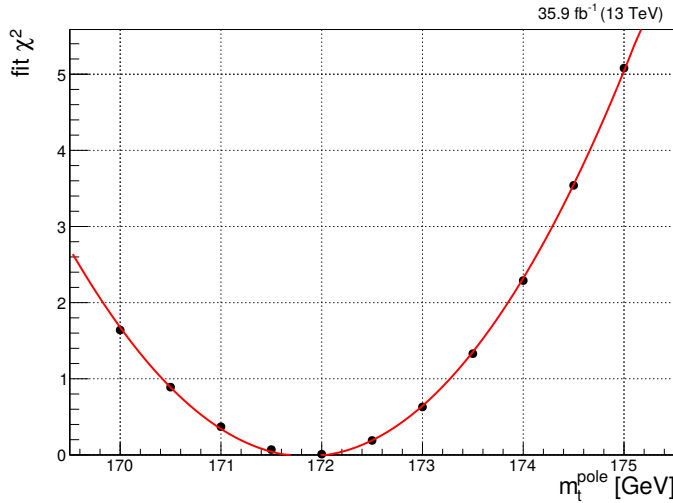


Figure 8.5: The values for $\chi^2(m_t^{\text{pole}})$ for the comparison of measured and predicted $\sigma_{t\bar{t}}$ with the nominal configuration. The red line indicates the result of the parabolic fit of the χ^2 distribution.

Chapter 9

Conclusion and outlook

In the context of this work three measurements are described, in each of which the top quark pair production cross section is measured in proton-proton collisions at a center of mass energy of $\sqrt{s} = 13 \text{ TeV}$. Two leptons are required in the final state. These separate measurements are performed using data sets with an integrated luminosity of $\mathcal{L}_{\text{int}} = 42 \text{ pb}^{-1}$, $\mathcal{L}_{\text{int}} = 2.2 \text{ fb}^{-1}$ and $\mathcal{L}_{\text{int}} = 35.9 \text{ fb}^{-1}$. The latter of these three measurements, using data with the highest luminosity, is the main result of this work. The measurements are performed with a binned maximum likelihood fit using observables of jet kinematics as templates. Systematic uncertainties are included as nuisance parameters.

In the full phase space the cross section for the three datasets mentioned previously is measured to be:

$$\begin{aligned}\sigma_{t\bar{t}} &= 778 \pm 54(\text{stat}) \pm 61(\text{syst}) \pm 76(\text{lumi}) \text{ pb} \quad \text{for } \mathcal{L}_{\text{int}} = 42 \text{ pb}^{-1}, \\ \sigma_{t\bar{t}} &= 793 \pm 7(\text{stat}) \pm 27(\text{syst}) \pm 21(\text{lumi}) \text{ pb} \quad \text{for } \mathcal{L}_{\text{int}} = 2.2 \text{ fb}^{-1}, \\ \text{and } \sigma_{t\bar{t}} &= 827 \pm 2(\text{stat}) \pm 24(\text{syst}) \pm 21(\text{lumi}) \text{ pb} \quad \text{for } \mathcal{L}_{\text{int}} = 35.9 \text{ fb}^{-1}.\end{aligned}$$

These results show a continuously improved precision for the measurement of the $t\bar{t}$ production cross section. The last (main) result is the most precise, with a total uncertainty of 32 pb (3.83%). For the main result, the $t\bar{t}$ cross section is measured in the dilepton channel including events from the $e^\pm\mu^\mp$, $\mu^+\mu^-$ and e^+e^- channel. Before the extrapolation to the full phase space, the $t\bar{t}$ production cross section is also measured in the visible phase space, as defined by the requirements for the leptons ($p_T(\text{lead}) > 25 \text{ GeV}$, $p_T(\text{sublead}) > 20 \text{ GeV}$, $M_{\ell\ell} > 20 \text{ GeV}$). For the main result, the $t\bar{t}$ production cross section in the visible phase space is measured as:

$$\sigma_{t\bar{t},\text{vis}} = 24.88 \pm 0.05(\text{stat}) \pm 0.65(\text{syst}) \pm 0.62(\text{lumi}) \text{ pb.}$$

The main result for the $t\bar{t}$ production cross section is used to extract the top quark pole mass with the xFitter framework [122]:

$$m_t^{\text{pole}} = 171.9 \pm 1.4(\text{exp} + \text{pdf} + \alpha_S) \pm 2.0(\text{scale}) \pm 0.2(m_t^{\text{MC}}) \text{ GeV.} \quad (9.1)$$

The precision of the extracted top quark pole mass is limited by the theory (scale) uncertainty, so the precision of the $t\bar{t}$ production cross section used for the extraction does not significantly influence the precision.

The main result for the measurement of the $t\bar{t}$ production cross section is compared to previous results, as well as theoretical predictions, in Figure 9.1. It agrees well with the theoretical predictions as well as with other measurements. Compared to previous measurements by both CMS and ATLAS, it is one of the most precise measurements of the $t\bar{t}$ cross section at $\sqrt{s} = 13 \text{ TeV}$.

All measurements of the $t\bar{t}$ cross section with different datasets and different experiments agree with the Standard Model prediction. The measurements from different experiments have now reached sensitivity comparable to the theoretical prediction. Nevertheless, improving the experimental sensitivity is still important.

The cross section measurement as presented here can be expanded to include a simultaneous fit of the cross section and the top quark mass. This allows for a coherent treatment of the correlation of top quark mass and the $t\bar{t}$ production cross section. The measured $t\bar{t}$ production cross section can be used to extract further Standard Model parameters like the strong coupling, α_S . These results are currently in CMS-internal review for a paper publication, together with the cross section measurement presented in this work.

The precision of the $t\bar{t}$ production cross section measurement could be improved by reducing systematic uncertainties. Since the systematic uncertainty is dominated by the uncertainty on the lepton efficiencies, a precise determination of the lepton efficiencies would improve the precision of the $t\bar{t}$ production cross section measurement. Similar to the study of the trigger efficiency in this work, a lepton efficiency measurement tailored specifically for this purpose could reduce the relevant uncertainty. With a large amount of data, it might be possible to measure the lepton efficiency in-situ within $t\bar{t}$ events by using kinematically reconstructed top quarks. Using the tag-and-probe technique, a hadronically decaying top quark could be the 'tag', while a leptonically decaying top quark could be used as a 'probe'.

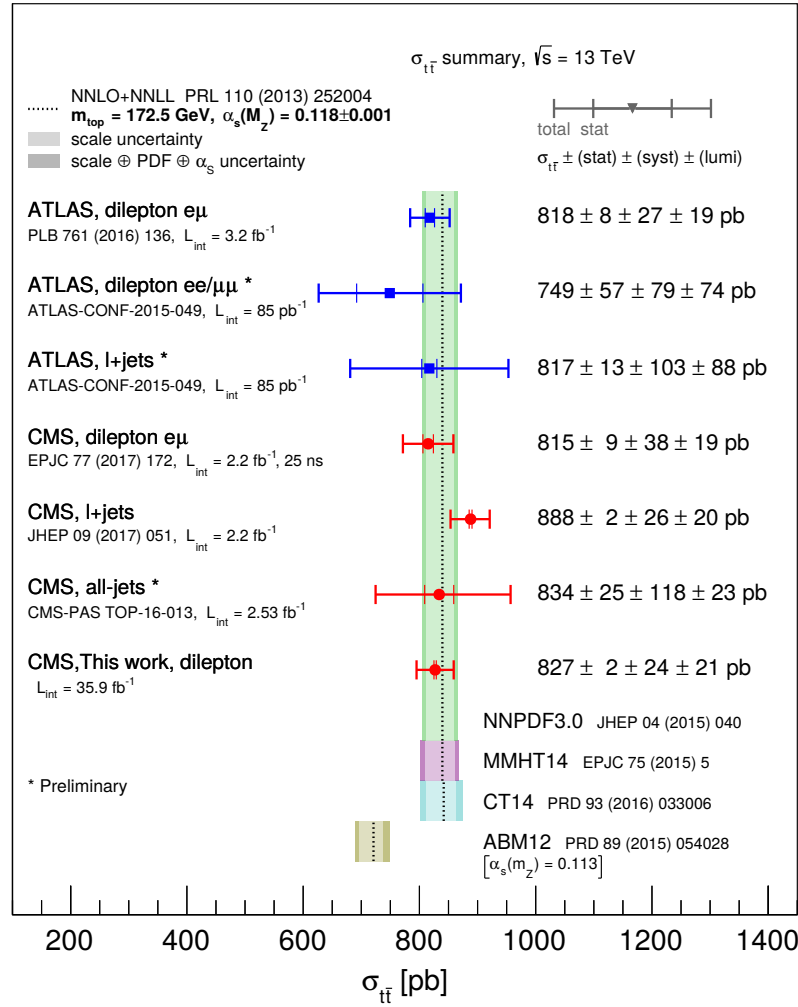


Figure 9.1: Summary of measurements of the $t\bar{t}$ production cross section at $\sqrt{s} = 13$ TeV by the CMS and ATLAS collaboration. The main result presented in this work is shown as well. All measurements are compared to theory predictions for different PDF sets. Modified from [123].

Another way to further improve the measurement would be a combination with the semi leptonic $t\bar{t}$ decay channel. As demonstrated in this work, such a combination has the potential to significantly reduce the uncertainties. If that study were to be extended to a proper measurement, special attention would have to be given to the definition of the visible phase space and the corresponding event selection. With a looser event selection, the separation between signal and background would become more challenging, as well as the determination of the contribution of background processes including fake leptons.

The measurement of the $t\bar{t}$ production cross section presented in this work could be extended by fitting the cross section in bins of relevant kinematic observables. These differential results could be more sensitive to physics phenomena beyond the SM.

Top quark physics are also a relevant topic for experiments beyond the LHC: At a linear electron-positron collider, the top quark mass could be measured with a precision below 100 MeV by using a scan of the collision energy around the threshold for top quark pair production [124]. A circular proton-proton collider at a center of mass energy of $\sqrt{s} = 100$ TeV would produce of the order of 10^{12} top quarks, which would allow for precise measurements of previously inaccessible processes.

In conclusion, a lot of possibilities to further extend or improve the measurement remain, even though a high precision for the measurement of the top quark pair production cross section has been achieved as presented in this work.

References

- [1] S. Chatrchyan et al., *Observation of a new boson at a mass of 125 gev with the cms experiment at the lhc*, Physics Letters B **716** (2012), no. 1, 30 – 61.
- [2] G. Aad et al., *Observation of a new particle in the search for the standard model higgs boson with the atlas detector at the lhc*, Physics Letters B **716** (2012), no. 1, 1 – 29.
- [3] M. Gell-Mann, *The Eightfold Way: A Theory of strong interaction symmetry*, (1961).
- [4] S. Weinberg, *A Model of Leptons*, Phys. Rev. Lett. **19** (1967), 1264–1266.
- [5] M. Breidenbach, J. I. Friedman, H. W. Kendall, E. D. Bloom, D. H. Coward, H. DeStaeler, J. Drees, L. W. Mo, and R. E. Taylor, *Observed behavior of highly inelastic electron-proton scattering*, Phys. Rev. Lett. **23** (1969), 935–939.
- [6] E. D. Bloom, D. H. Coward, H. DeStaeler, J. Drees, G. Miller, L. W. Mo, R. E. Taylor, M. Breidenbach, J. I. Friedman, G. C. Hartmann, and H. W. Kendall, *High-energy inelastic e – p scattering at 6° and 10°*, Phys. Rev. Lett. **23** (1969), 930–934.
- [7] G. Arnison et al., *Experimental observation of isolated large transverse energy electrons with associated missing energy at s=540 gev*, Physics Letters B **122** (1983), no. 1, 103 – 116.
- [8] G. Arnison et al., *Experimental observation of lepton pairs of invariant mass around 95 gev/c2 at the cern sps collider*, Physics Letters B **126** (1983), no. 5, 398 – 410.
- [9] M. Banner et al., *Observation of single isolated electrons of high transverse momentum in events with missing transverse energy at the cern pp collider*, Physics Letters B **122** (1983), no. 5, 476 – 485.
- [10] P. Bagnaia et al., *Evidence for $z0 \rightarrow e+e-$ at the cern pp collider*, Physics Letters B **129** (1983), no. 1, 130 – 140.
- [11] MissMJ, *Standard model of elementary particles*, https://commons.wikimedia.org/wiki/File:Standard_Model_of_Elementary_Particles.svg, Accessed: 2018-04-23.
- [12] P.W. Higgs, *Broken symmetries, massless particles and gauge fields*, Physics Letters **12** (1964), no. 2, 132 – 133.
- [13] F. Englert and R. Brout, *Broken symmetry and the mass of gauge vector mesons*, Phys. Rev. Lett. **13** (1964), 321–323.

- [14] G. S. Guralnik, C. R. Hagen, and T. W. B. Kibble, *Global conservation laws and massless particles*, Phys. Rev. Lett. **13** (1964), 585–587.
- [15] H. Abramowicz et al., *Combination of measurements of inclusive deep inelastic $e^\pm p$ scattering cross sections and QCD analysis of HERA data*, Eur. Phys. J. **C75** (2015), no. 12, 580.
- [16] C. Patrignani et al., *Review of Particle Physics*, Chin. Phys. **C40** (2016), no. 10, 100001.
- [17] F. Abe et al., *Observation of top quark production in $\bar{p}p$ collisions with the collider detector at fermilab*, Phys. Rev. Lett. **74** (1995), 2626–2631.
- [18] S. Abachi et al., *Observation of the top quark*, Phys. Rev. Lett. **74** (1995), 2632–2637.
- [19] K. R. Lynch, S. Mrenna, M. Narain, and E. H. Simmons, *Finding Z' bosons coupled preferentially to the third family at cern lep and the fermilab tevatron*, Phys. Rev. D **63** (2001), 035006.
- [20] J. L. Rosner, *Prominent decay modes of a leptophobic Z'* , Physics Letters B **387** (1996), no. 1, 113 – 117.
- [21] H.P. Nilles, *Supersymmetry, supergravity and particle physics*, Physics Reports **110** (1984), no. 1, 1 – 162.
- [22] G. R. Farrar and P. Fayet, *Phenomenology of the production, decay, and detection of new hadronic states associated with supersymmetry*, Physics Letters B **76** (1978), no. 5, 575 – 579.
- [23] D. B. Franzosi and C. Zhang, *Probing the top-quark chromomagnetic dipole moment at next-to-leading order in qcd*, Phys. Rev. D **91** (2015), 114010.
- [24] J. Drobniak, S. Fajfer, and J. F. Kamenik, *New physics in $t \rightarrow bw$ decay at next-to-leading order in qcd*, Phys. Rev. D **82** (2010), 114008.
- [25] J. Gao, C. S. Li, J. J. Zhang, and H. X. Zhu, *Next-to-leading order qcd corrections to the single top quark production via model-independent tqg flavor-changing neutral-current couplings at hadron colliders*, Phys. Rev. D **80** (2009), 114017.
- [26] U. Husemann, *Top-Quark Physics: Status and Prospects*, Prog. Part. Nucl. Phys. **95** (2017), 48–97.
- [27] F. Cascioli, S. Kallweit, P. Maierhöfer, and S. Pozzorini, *A unified NLO description of top-pair and associated Wt production*, Eur. Phys. J. **C74** (2014), no. 3, 2783.
- [28] C. D. White, S. Frixione, E. Laenen, and F. Maltoni, *Isolating Wt production at the LHC*, JHEP **11** (2009), 074.
- [29] M. Czakon, P. Fiedler, and A. Mitov, *Total Top-Quark Pair-Production Cross Section at Hadron Colliders Through $O(\alpha_S^4)$* , Phys.Rev.Lett. **110** (2013), 252004.
- [30] ATLAS, CDF, CMS and D0 Collaborations, *First combination of Tevatron and LHC measurements of the top-quark mass*, (2014).

- [31] V. Khachatryan et al., *Measurement of the top quark mass using proton-proton data at $\sqrt{s} = 7$ and 8 TeV*, Phys. Rev. **D93** (2016), no. 7, 072004.
- [32] I. I. Y. Bigi, M. A. Shifman, N. G. Uraltsev, and A. I. Vainshtein, *The Pole mass of the heavy quark. Perturbation theory and beyond*, Phys. Rev. **D50** (1994), 2234–2246.
- [33] M. Dowling and S.-O. Moch, *Differential distributions for top-quark hadro-production with a running mass*, Eur. Phys. J. **C74** (2014), no. 11, 3167.
- [34] M. Beneke and V. M. Braun, *Heavy quark effective theory beyond perturbation theory: Renormalons, the pole mass and the residual mass term*, Nucl. Phys. **B426** (1994), 301–343.
- [35] M. Beneke, P. Marquard, P. Nason, and M. Steinhauser, *On the ultimate uncertainty of the top quark pole mass*, Phys. Lett. **B775** (2017), 63–70.
- [36] G. Aad et al., *Measurement of the $t\bar{t}$ production cross-section using $e\mu$ events with b -tagged jets in pp collisions at $\sqrt{s} = 7$ and 8 TeV with the ATLAS detector*, Eur. Phys. J. **C74** (2014), no. 10, 3109, [Addendum: Eur. Phys. J.C76,no.11,642(2016)].
- [37] V. Khachatryan et al., *Measurement of the t - \bar{t} production cross section in the e - μ channel in proton-proton collisions at $\text{sqrt}(s) = 7$ and 8 TeV*, JHEP **08** (2016), 029.
- [38] A. Buckley et al., *General-purpose event generators for LHC physics*, Phys. Rept. **504** (2011), 145–233.
- [39] P. Marquard, A. V. Smirnov, V. A. Smirnov, and M. Steinhauser, *Quark Mass Relations to Four-Loop Order in Perturbative QCD*, Phys. Rev. Lett. **114** (2015), no. 14, 142002.
- [40] V. M. Abazov et al., *Determination of the pole and \overline{MS} masses of the top quark from the $t\bar{t}$ cross section*, Phys. Lett. **B703** (2011), 422–427.
- [41] M. Baak, J. Cúth, J. Haller, A. Hoecker, R. Kogler, K. Mönig, M. Schott, and J. Stelzer, *The global electroweak fit at NNLO and prospects for the LHC and ILC*, Eur. Phys. J. **C74** (2014), 3046.
- [42] D. Buttazzo, G. Degrassi, P. P. Giardino, G. F. Giudice, F. Sala, A. Salvio, and A. Strumia, *Investigating the near-criticality of the Higgs boson*, JHEP **12** (2013), 089.
- [43] C. M. Carloni Calame, G. Montagna, O. Nicrosini, and A. Vicini, *Precision electroweak calculation of the production of a high transverse-momentum lepton pair at hadron colliders*, JHEP **10** (2007), 109.
- [44] R. Gavin, Y. Li, F. Petriello, and S. Quackenbush, *FEWZ 2.0: A code for hadronic Z production at next-to-next-to-leading order*, Comput. Phys. Commun. **182** (2011), 2388–2403.
- [45] J. M. Campbell, F. Caola, F. Febres Cordero, L. Reina, and D. Wackerlo, *Next-to-leading order qcd predictions for w+1 jet and w+2 jet production with at least one b jet at the 7 tev lhc*, Phys. Rev. D **86** (2012), 034021.

- [46] M. S. Neubauer, *Diboson production at colliders*, Annual Review of Nuclear and Particle Science **61** (2011), no. 1, 223–250.
- [47] J. M. Campbell and R. K. Ellis, *An Update on vector boson pair production at hadron colliders*, Phys. Rev. **D60** (1999), 113006.
- [48] J. M. Campbell, R. K. Ellis, and C. Williams, *Vector boson pair production at the LHC*, JHEP **07** (2011), 018.
- [49] T. Gehrmann, M. Grazzini, S. Kallweit, P. Maierhöfer, A. von Manteuffel, S. Pozzorini, D. Rathlev, and L. Tancredi, *W^+W^- Production at Hadron Colliders in Next to Next to Leading Order QCD*, Phys. Rev. Lett. **113** (2014), no. 21, 212001.
- [50] N. Kidonakis, *Two-loop soft anomalous dimensions for single top quark associated production with W^- or H^-* , Phys. Rev. D **82** (2010), 054018.
- [51] M. Dobbs and J. B. Hansen, *The HepMC C++ Monte Carlo Event Record for High Energy Physics*, Tech. Report ATL-SOFT-2000-001, CERN, Geneva, Jun 2000, revised version number 1 submitted on 2001-02-27 09:54:32.
- [52] T. Gleisberg, S. Hoeche, F. Krauss, M. Schonherr, S. Schumann, F. Siegert, and J. Winter, *Event generation with SHERPA 1.1*, JHEP **02** (2009), 007.
- [53] S. Alioli et al., *A general framework for implementing NLO calculations in shower Monte Carlo programs: the POWHEG BOX*, JHEP **06** (2010), 043.
- [54] S. Frixione, P. Nason, and C. Oleari, *Matching NLO QCD computations with Parton Shower simulations: the POWHEG method*, JHEP **11** (2007), 070.
- [55] P. Nason, *A New method for combining NLO QCD with shower Monte Carlo algorithms*, JHEP **11** (2004), 040.
- [56] S. Frixione, P. Nason, and G. Ridolfi, *A Positive-weight next-to-leading-order Monte Carlo for heavy flavour hadroproduction*, JHEP **09** (2007), 126.
- [57] E. Re, *Single-top Wt-channel production matched with parton showers using the POWHEG method*, Eur. Phys. J. **C71** (2011), 1547.
- [58] A. Kardos, P. Nason, and C. Oleari, *Three-jet production in POWHEG*, JHEP **04** (2014), 043.
- [59] S. Alioli, P. Nason, C. Oleari, and E. Re, *Vector boson plus one jet production in POWHEG*, JHEP **01** (2011), 095.
- [60] J. Alwall, R. Frederix, S. Frixione, V. Hirschi, F. Maltoni, O. Mattelaer, H. S. Shao, T. Stelzer, P. Torrielli, and M. Zaro, *The automated computation of tree-level and next-to-leading order differential cross sections, and their matching to parton shower simulations*, JHEP **07** (2014), 079.
- [61] R. Frederix and S. Frixione, *Merging meets matching in MC@NLO*, JHEP **12** (2012), 061.

- [62] T. Sjöstrand, S. Ask, J. R. Christiansen, R. Corke, N. Desai, P. Ilten, S. Mrenna, S. Prestel, C. O. Rasmussen, and P. Z. Skands, *An Introduction to PYTHIA 8.2*, Comput. Phys. Commun. **191** (2015), 159.
- [63] R. D. Ball et al., *Parton distributions with LHC data*, Nucl. Phys. B **867** (2013), 244.
- [64] CMS Collaboration, *Investigations of the impact of the parton shower tuning in Pythia 8 in the modelling of $t\bar{t}$ at $\sqrt{s} = 8$ and 13 TeV*, Tech. Report CMS-PAS-TOP-16-021, CERN, Geneva, 2016.
- [65] P. Skands, S. Carrazza, and J. Rojo, *Tuning PYTHIA 8.1: the Monash 2013 tune*, Eur. Phys. J. C **74** (2014), 3024.
- [66] J. Allison et al., *Geant4 developments and applications*, IEEE Trans. Nucl. Sci. **53** (2006), 270.
- [67] L. Evans and Philip B., *Lhc machine*, Journal of Instrumentation **3** (2008), no. 08, S08001.
- [68] M. Zanetti, *Beams Scan based Absolute Normalization of the CMS Luminosity Measurement. CMS 2010 luminosity determination*, (2011).
- [69] G. L. Bayatian et al., *CMS Physics: Technical Design Report Volume 1: Detector Performance and Software*, Technical Design Report CMS, CERN, Geneva, 2006, There is an error on cover due to a technical problem for some items.
- [70] CMS Collaboration, *Detector Drawings*, CMS Collection., Mar 2012.
- [71] A. Dominguez et al., *CMS Technical Design Report for the Pixel Detector Upgrade*, Tech. Report CERN-LHCC-2012-016. CMS-TDR-11, Sep 2012.
- [72] S. Chatrchyan et al., *Alignment of the CMS tracker with LHC and cosmic ray data*, JINST **9** (2014), P06009.
- [73] A. M. Sirunyan et al., *Particle-flow reconstruction and global event description with the CMS detector*, JINST **12** (2017), no. 10, P10003.
- [74] The CMS Collaboration, *Description and performance of track and primary-vertex reconstruction with the cms tracker*, Journal of Instrumentation **9** (2014), no. 10, P10009.
- [75] S. Chatrchyan et al., *Performance and Operation of the CMS Electromagnetic Calorimeter*, JINST **5** (2010), T03010.
- [76] CMS Collaboration, *Identification and filtering of uncharacteristic noise in the CMS hadron calorimeter*, Journal of Instrumentation **5** (2010), T03014.
- [77] G. L. Bayatyan et al., *CMS TriDAS project: Technical Design Report, Volume 1: The Trigger Systems*, Technical Design Report CMS.
- [78] A. Tapper and D. Acosta, *CMS Technical Design Report for the Level-1 Trigger Upgrade*, (2013).

- [79] W. Adam, B. Mangano, T. Speer, and T. Todorov, *Track Reconstruction in the CMS tracker*, Tech. Report CMS-NOTE-2006-041, CERN, Geneva, Dec 2006.
- [80] CMS Collaboration, *Electron and photon performance in CMS with the full 2016 data sample.*, Tech. report, CERN, Mar 2017.
- [81] CMS Collaboration, *Electron performance using first data collected by CMS in 2016*, Tech. report, CERN, Jun 2016.
- [82] CMS Collaboration, *Jet algorithms performance in 13 TeV data*, Tech. Report CMS-PAS-JME-16-003, CERN, Geneva, 2017.
- [83] Matteo Cacciari, Gavin P. Salam, and Gregory Soyez, *The anti- k_t jet clustering algorithm*, JHEP **04** (2008), 063.
- [84] Matteo Cacciari, Gavin P. Salam, and Gregory Soyez, *FastJet user manual*, Eur. Phys. J. C **72** (2012), 1896.
- [85] CMS Collaboration, *Pileup Removal Algorithms*, Tech. Report CMS-PAS-JME-14-001, CERN, Geneva, 2014.
- [86] M. Cacciari, G. P. Salam, and G. Soyez, *The catchment area of jets*, Journal of High Energy Physics **2008** (2008), no. 04, 005.
- [87] M. Cacciari and G. P. Salam, *Pileup subtraction using jet areas*, Physics Letters B **659** (2008), no. 1, 119 – 126.
- [88] V. Khachatryan et al., *Jet energy scale and resolution in the CMS experiment in pp collisions at 8 TeV*, JINST **12** (2017), no. 02, P02014.
- [89] The CMS collaboration, *Determination of jet energy calibration and transverse momentum resolution in cms*, Journal of Instrumentation **6** (2011), no. 11, P11002.
- [90] CMS Collaboration, *Jet energy scale and resolution performances with 13TeV data*, Tech. report, CERN, Jun 2016.
- [91] CMS Collaboration, *Performance of missing energy reconstruction in 13 TeV pp collision data using the CMS detector*, Tech. Report CMS-PAS-JME-16-004, CERN, Geneva, 2016.
- [92] CMS Collaboration, *Identification of b and c jets in the cms experiment at the lhc run 2*, paper underway CMS-PAS-BTV-16-002, CERN, 2017.
- [93] CMS Collaboration, *Performance of heavy flavour identification algorithms in proton-proton collisions at 13 TeV at the CMS experiment*, Tech. report, CERN, May 2017.
- [94] C. J. Clopper and E. S. Pearson, *The use of confidence or fiducial limits illustrated in the case of the binomial*, Biometrika **26** (1934), no. 4, 404–413.
- [95] R. D. Cousins, K. E. Hymes, and J. Tucker, *Frequentist evaluation of intervals estimated for a binomial parameter and for the ratio of Poisson means*, Nuclear Instruments and Methods in Physics Research A **612** (2010), 388–398.

- [96] CMS Collaboration, *CMS Luminosity Measurements for the 2016 Data Taking Period*, Tech. Report CMS-PAS-LUM-17-001, CERN, Geneva, 2017.
- [97] V. Khachatryan et al., *Measurement of the differential cross section for top quark pair production in pp collisions at $\sqrt{s} = 8 \text{ TeV}$* , Eur. Phys. J. C **75** (2015), 542.
- [98] G. Aad et al., *Measurements of top-quark pair differential cross-sections in the lepton+jets channel in pp collisions at $\sqrt{s} = 8 \text{ TeV}$ using the ATLAS detector*, Eur. Phys. J. C **76** (2016), no. 10, 538.
- [99] F. James and M. Roos, *Minuit: a system for function minimization and analysis of the parameter errors and correlations*, Comput. Phys. Commun. **10** (1975), 343.
- [100] T. Sjostrand, S. Mrenna, and P. Z. Skands, *PYTHIA 6.4 Physics and Manual*, JHEP **05** (2006), 026.
- [101] M. Bähr, S. Gieseke, M. A. Gigg, D. Grellscheid, K. Hamilton, O. Latunde-Dada, S. Plätzer, P. Richardson, M. H. Seymour, A. Sherstnev, and B. R. Webber, *Herwig++ physics and manual*, Eur. Phys. J. C **58** (2008), 639.
- [102] M. Aaboud et al., *Measurement of the Inelastic Proton-Proton Cross Section at $\sqrt{s} = 13 \text{ TeV}$ with the ATLAS Detector at the LHC*, Phys. Rev. Lett. **117** (2016), 182002.
- [103] S. Argyropoulos and T. Sjöstrand, *Effects of color reconnection on $t\bar{t}$ final states at the LHC*, JHEP **11** (2014), 043.
- [104] J. R. Christiansen and P. Z. Skands, *String Formation Beyond Leading Colour*, JHEP **08** (2015), 003.
- [105] CMS Collaboration, *Measurement of the differential cross section for $t\bar{t}$ production in the dilepton final state at $\sqrt{s} = 13 \text{ TeV}$* , Tech. Report CMS-PAS-TOP-16-011, CERN, Geneva, 2016.
- [106] M. Czakon, D. Heymes, and A. Mitov, *High-precision differential predictions for top-quark pairs at the lhc*, Phys. Rev. Lett. **116** (2016), 082003.
- [107] S. Dulat, T.-J. Hou, J. Gao, M. Guzzi, J. Huston, P. Nadolsky, J. Pumplin, C. Schmidt, D. Stump, and C. P. Yuan, *New parton distribution functions from a global analysis of quantum chromodynamics*, Phys. Rev. D **93** (2016), no. 3, 033006.
- [108] M. G. Bowler, *e+e- production of heavy quarks in the string model*, Zeitschrift für Physik C Particles and Fields **11** (1981), no. 2, 169–174.
- [109] C. Peterson, D. Schlatter, I. Schmitt, and P. M. Zerwas, *Scaling violations in inclusive e^+e^- annihilation spectra*, Phys. Rev. D **27** (1983), 105–111.
- [110] V. Khachatryan et al., *Measurement of the top quark pair production cross section in proton-proton collisions at $\sqrt(s) = 13 \text{ TeV}$* , Phys. Rev. Lett. **116** (2016), no. 5, 052002.
- [111] V. Khachatryan et al., *Measurement of the $t\bar{t}$ production cross section using events in the $e\mu$ final state in pp collisions at $\sqrt{s} = 13 \text{ TeV}$* , Eur. Phys. J. C **77** (2017), 172.

- [112] CMS Collaboration, *CMS luminosity measurement for the 2015 data-taking period*, Tech. Report CMS-PAS-LUM-15-001, CERN, Geneva, 2017.
- [113] M. Czakon and A. Mitov, *Top++: A Program for the Calculation of the Top-Pair Cross-Section at Hadron Colliders*, Comput.Phys.Commun. **185** (2014), 2930.
- [114] V. Andreev et al., *Determination of the strong coupling constant $\alpha_s(M_Z)$ in next-to-next-to-leading order QCD using H1 jet cross section measurements*, (2017).
- [115] A. M. Sirunyan et al., *Measurement of the $t\bar{t}$ production cross section using events with one lepton and at least one jet in pp collisions at $\sqrt{s} = 13$ TeV*, JHEP **09** (2017), 051.
- [116] M. Aaboud et al., *Measurement of the $t\bar{t}$ production cross-section using $e\mu$ events with b -tagged jets in pp collisions at $\sqrt{s}=13$ TeV with the ATLAS detector*, Phys. Lett. **B761** (2016), 136–157, [Erratum: Phys. Lett.B772,879(2017)].
- [117] P. Bärnreuther, M. Czakon, and A. Mitov, *Percent-level-precision physics at the tevatron: Next-to-next-to-leading order qcd corrections to $q\bar{q} \rightarrow t\bar{t}+x$* , Phys. Rev. Lett. **109** (2012), 132001.
- [118] M. Czakon and A. Mitov, *NNLO corrections to top-pair production at hadron colliders: the all-fermionic scattering channels*, JHEP **12** (2012), 054.
- [119] M. Czakon and A. Mitov, *NNLO corrections to top pair production at hadron colliders: the quark-gluon reaction*, JHEP **01** (2013), 080.
- [120] M. Aliev, H. Lacker, U. Langenfeld, S. Moch, P. Uwer, et al., *HATHOR: HAdronic Top and Heavy quarks crOss section calculatoR*, Comput.Phys.Commun. **182** (2011), 1034–1046.
- [121] R. D. Ball et al., *Parton distributions from high-precision collider data*, (2017).
- [122] S. Alekhin et al., *HERAFitter*, Eur. Phys. J. **C75** (2015), no. 7, 304.
- [123] LHCTOPWG, *Summary of measurements of the top-pair production cross-section at 13 tev*, <https://twiki.cern.ch/twiki/bin/view/LHCPhysics/LHCTopWGSummaryPlots>, Accessed: 2018-05-11.
- [124] K. Seidel, F. Simon, M. Tesař, and S. Poss, *Top quark mass measurements at and above threshold at clic*, The European Physical Journal C **73** (2013), no. 8, 2530.

Appendix A

Detailed breakdown of systematic uncertainties

Table A.1: Extracted cross sections with detailed list of uncertainties. Besides the contribution to the total uncertainty in %, the fitted value of the nuisance parameter (pull), as well as the ratio of the estimated uncertainty over the uncertainty from a 1σ variation, called constr/ σ , are shown.

Name	Pull	Constr / σ	Contribution [%]
B-tag	1.222	0.42	0.249
Mistag	0.587	0.95	-0.120
Electron energy resolution - phi	-0.424	0.98	-0.007
Electron energy resolution - rho	-0.022	0.94	0.010
Electron energy scale	0.965	0.89	-0.144
Electron ID / isolation	0.292	0.58	-1.931
Jet energy resolution	-0.015	0.59	0.063
JES: MPF	0.006	0.43	0.004
JES: Absolute Scale	0.347	0.62	-0.025
JES: Absolute Stat	0.423	0.83	-0.048
JES: Fragmentation	-0.019	0.46	-0.052
JES: Pileup Data/MC	-0.07	0.46	-0.117
JES: Pileup p_T BB	0.19	0.51	-0.112
JES: PileUp p_T EC1	-0.092	0.78	-0.177
JES: PileUp p_T Ref	-0.008	0.42	-0.102
JES: Relative Balance	0.365	0.4	-0.041
JES: Intercalibration	0.257	0.53	0.003

Name	Pull	Constr / σ	Contribution [%]
JES: Relative JER EC1	-0.237	1.31	0.003
JES: Relative p_T BB	0.116	0.53	-0.043
JES: Relative p_T EC1	-1.234	0.52	-0.001
JES: Relative Stat EC	0.36	0.76	0.047
JES: Relative Stat FSR	-0.378	1.06	0.005
JES: Single pion ECAL	0.029	0.45	-0.062
JES: Single pion HCAL	-0.007	0.47	-0.026
JES: Time $p_T \eta$	0.125	0.63	0.033
Muon energy scale	-0.173	0.57	-0.030
Muon ID / isolation	-0.385	0.84	-2.080
Pile-up	0.248	0.64	0.220
tW FSR scale	-0.065	0.53	0.004
tW ISR scale	0.062	0.47	-0.021
tW ME scale	-0.244	1.01	0.083
Top p_T	1.735	0.43	0.503
Trigger	0.033	1	-0.338
B-hadron BR	0.029	0.67	-0.020
CR ERD on	0	0.21	-0.001
CR Gluon move	0.524	0.23	0.113
CR QCD-inspired	0.005	0.96	0.328
fragm. Peterson	0.859	0.76	-0.193
fragmentation	-1.127	0.48	-0.344
$t\bar{t}$ FSR scale	-0.001	0.15	0.541
$t\bar{t}$ ISR scale	-0.133	0.13	-0.209
ME/PS matching	-0.067	0.22	0.143
$t\bar{t}$ ME scale	0.438	0.43	-0.086
UE tune	-0.52	0.25	0.270
PDF10	0.02	0.86	0.445
PDF11	0.031	0.87	0.165
PDF12	-0.007	0.86	-0.251
PDF13	0.115	0.86	0.134
PDF14	0.012	0.86	-0.113
PDF15	0.014	0.85	-0.079
PDF16	-0.005	0.86	0.074
PDF17	-0.035	0.85	-0.173

Name	Pull	Constr / σ	Contribution [%]
PDF18	-0.127	0.85	0.087
PDF19	-0.038	0.85	0.349
PDF1	-0.009	0.86	-0.037
PDF20	-0.066	0.86	0.143
PDF21	-0.119	0.85	-0.156
PDF22	-0.197	0.86	-0.179
PDF23	0.096	0.8	-0.057
PDF24	0.065	0.9	0.138
PDF25	-0.06	0.87	-0.002
PDF26	0.019	0.85	0.018
PDF27	0.034	0.85	0.080
PDF28	0.011	0.83	-0.018
PDF2	-0.164	0.96	0.046
PDF3	0.026	0.84	0.155
PDF4	-0.062	0.9	0.114
PDF5	-0.023	0.82	-0.390
PDF6	-0.041	0.87	0.147
PDF7	0.045	0.83	-0.525
PDF8	0.076	0.87	-0.057
PDF9	0.05	0.86	-0.021
JES: Flavor response	0.088	0.43	-0.048
tW background	1.41	0.56	-1.072
Diboson background	1.322	0.66	0.269
$t\bar{t}$ background	0.27	1.01	-0.296
W+jets background	-3.567	0.47	0.168
DY background (0 b-jets)	0.167	0.32	0.366
DY background (1 b-jets)	-0.473	0.13	0.838
DY background (2 b-jets)	-0.574	0.67	-0.090
$\sigma_{t\bar{t}}$ (13 TeV)	-4.346	21.88	2.644
Stat			0.192
Total vis			$\pm^{2.644}_{2.526}$
$\sigma_{t\bar{t}}(13 \text{ TeV})$ vis			24.8794 pb
$t\bar{t}$ ISR scale (extr)			$\pm^{0.104}_{0.011}$
$t\bar{t}$ FSR scale (extr)			$\pm^{0.051}_{0.017}$
$t\bar{t}$ ME scale (extr)			$\pm^{0.324}_{0.069}$

Name	Pull	Constr / σ	Contribution [%]
UE tune (extr)			$\pm^{0.015}_{0.036}$
PDF (extr)			$\pm^{0.763}_{0.635}$
Top p_T (extr)			$\mp^{0.777}_{0.000}$
Total			$\pm^{2.880}_{2.606}$
$\sigma_{t\bar{t}}(13 \text{ TeV})$			827.41 pb

Appendix B

List of publications

- Measurement of the top quark pair production cross section at 13 TeV with the CMS detector,
T. Arndt, PoS TOP2015 (2016) 026
- Measurement of the top quark pair production cross section using $e\mu$ events in proton-proton collisions at $\sqrt{s} = 13$ TeV with the CMS detector,
CMS Collaboration, Eur.Phys.J. C77 (2017) 172, DOI: 10.1140/epjc/s10052-017-4718-8
- Measurement of the top quark pair production cross section in proton-proton collisions at $\sqrt{s} = 13$ TeV with the CMS detector,
CMS Collaboration, Phys. Rev. Lett. 116 (2016) 052002, DOI: 10.1103/PhysRevLett.116.052002
- Measurement of normalized differential $t\bar{t}$ cross sections in the dilepton channel from pp collisions at $\sqrt{s} = 13$ TeV,
CMS Collaboration, JHEP 1704 (2017) 060, DOI: 10.1007/JHEP04(2018)060
- Search for $t\bar{t}H$ production in the $H \rightarrow b\bar{b}$ decay channel with leptonic $t\bar{t}$ decays in proton-proton collisions at $\sqrt{s} = 13$ TeV,
CMS Collaboration, Preliminary publication, April 2018, CMS-PAS-HIG-17-026
- Search for $t\bar{t}H$ production in the $H \rightarrow b\bar{b}$ decay channel with $\sqrt{s} = 13$ TeV pp collisions at the CMS experiment,
CMS Collaboration, Preliminary publication, March 2016, CMS-PAS-HIG-16-004

- First measurement of the differential cross section for $t\bar{t}$ production in the dilepton final state at $\sqrt{s} = 13$ TeV,
CMS Collaboration, Preliminary publication, August 2015, CMS-PAS-TOP-15-010